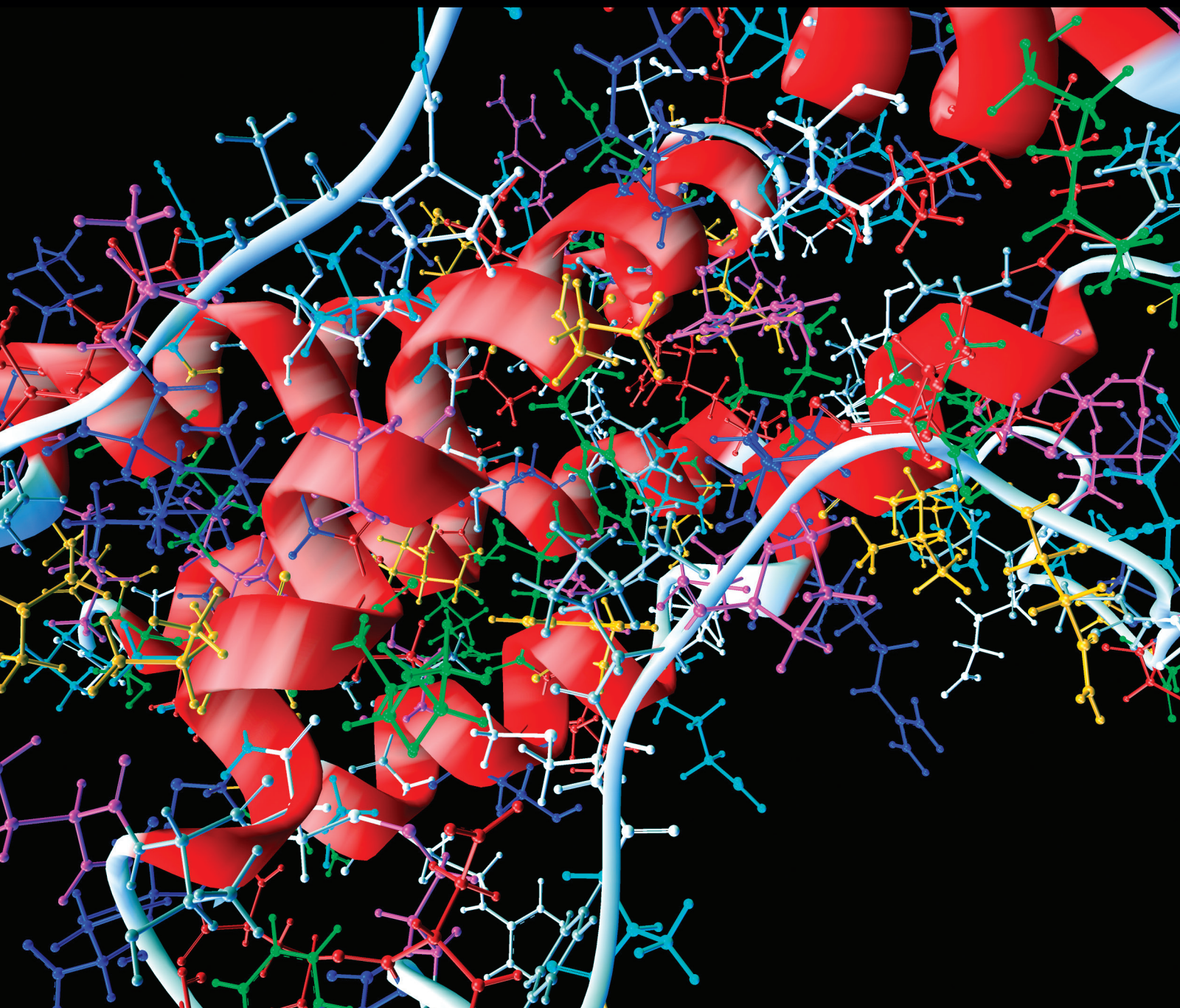


Computational and Mathematical Methods in Medicine

Computational Bioelectromagnetics in Medicine

Lead Guest Editor: Marta Parazzini

Guest Editors: György Thuróczy and Wout Joseph





Computational Bioelectromagnetics in Medicine

Computational and Mathematical Methods in Medicine

Computational Bioelectromagnetics in Medicine

Lead Guest Editor: Marta Parazzini

Guest Editors: György Thuróczy and Wout Joseph



Copyright © 2018 Hindawi. All rights reserved.

This is a special issue published in “Computational and Mathematical Methods in Medicine.” All articles are open access articles distributed under the Creative Commons Attribution License, which permits unrestricted use, distribution, and reproduction in any medium, provided the original work is properly cited.

Editorial Board

Raul Alcaraz, Spain
Emil Alexov, USA
Konstantin G. Arbeev, USA
Georgios Archontis, Cyprus
Enrique Berjano, Spain
Junguo Bian, USA
Elia Biganzoli, Italy
Konstantin Blyuss, UK
Hans A. Braun, Germany
Zoran Bursac, USA
Thierry Busso, France
Guy Carrault, France
Filippo Castiglione, Italy
Carlos Castillo-Chavez, USA
Prem Chapagain, USA
Hsiu-Hsi Chen, Taiwan
Wai-Ki Ching, Hong Kong
Nadia A. Chuzhanova, UK
Maria N. D.S. Cordeiro, Portugal
Cristiana Corsi, Italy
Irena Cosic, Australia
Qi Dai, China
Chuangyin Dang, Hong Kong
Didier Delignières, France
Jun Deng, USA
Thomas Desaive, Belgium
David Diller, USA
Michel Dojat, France
Irina Doytchinova, Bulgaria
Esmaeil Ebrahimie, Australia
Georges El Fakhri, USA
Issam El Naqa, USA
Angelo Facchiano, Italy

Luca Faes, Italy
Maria E. Fantacci, Italy
Giancarlo Ferrigno, Italy
Marc Thilo Figge, Germany
Alfonso T. García-Sosa, Estonia
Humberto González-Díaz, Spain
Igor I. Goryanin, Japan
Marko Gosak, Slovenia
Damien Hall, Australia
Roberto Hornero, Spain
Tingjun Hou, China
Seiya Imoto, Japan
Hsueh-Fen Juan, Taiwan
Martti Juhola, Finland
Rafik Karaman, Palestine
Andrzej Kloczkowski, USA
Chung-Min Liao, Taiwan
Ezequiel López-Rubio, Spain
Reinoud Maex, Belgium
Valeri Makarov, Spain
Kostas Marias, Greece
Juan Pablo Martínez, Spain
Richard J. Maude, Thailand
Michele Migliore, Italy
John Mitchell, UK
Luminita Moraru, Romania
Chee M. Ng, USA
Michele Nichelatti, Italy
Kazuhisa Nishizawa, Japan
Francesco Pappalardo, Italy
Manuel F. G. Penedo, Spain
Jesús Picó, Spain
Alberto Policriti, Italy

Giuseppe Pontrelli, Italy
Jesús Poza, Spain
Christopher Pretty, New Zealand
Mihai V. Putz, Romania
Jose Joaquin Rieta, Spain
Jan Rychtar, USA
Vinod Scaria, India
Xu Shen, China
Simon A. Sherman, USA
Dong Song, USA
Xinyuan Song, Hong Kong
João M. R. S. Tavares, Portugal
Jlenia Toppi, Italy
Nelson J. Trujillo-Barreto, UK
Anna Tsantili-Kakoulidou, Greece
Markos G. Tsipouras, Greece
Po-Hsiang Tsui, Taiwan
Gabriel Turinici, France
Raoul van Loon, UK
Liangjiang Wang, USA
Ruisheng Wang, USA
David A. Winkler, Australia
Gabriel Wittum, Germany
Yu Xue, China
Yongqing Yang, China
Chen Yanover, Israel
Xiaojun Yao, China
Kaan Yetilmezsoy, Turkey
Hiro Yoshida, USA
Henggui Zhang, UK
Yuhai Zhao, China
Xiaoqi Zheng, China

Contents

Stimulation Strategies for Tinnitus Suppression in a Neuron Model

Alessandra Paffi , Francesca Camera , Chiara Carocci, Francesca Apollonio , and Micaela Liberti 
Research Article (9 pages), Article ID 5215723, Volume 2018 (2018)

A Neuromuscular Interface for Robotic Devices Control

Innokentiy Kastalskiy , Vasily Mironov, Sergey Lobov, Nadia Krilova , Alexey Pimashkin,
and Victor Kazantsev
Research Article (8 pages), Article ID 8948145, Volume 2018 (2018)

Modelling of the Current Density Distributions during Cortical Electric Stimulation for Neuropathic Pain Treatment

S. Fiocchi , E. Chiaramello , P. Ravazzani , and M. Parazzini
Research Article (12 pages), Article ID 1056132, Volume 2018 (2018)

Transfer Kernel Common Spatial Patterns for Motor Imagery Brain-Computer Interface Classification

Mengxi Dai, Dezhi Zheng , Shucong Liu, and Pengju Zhang
Research Article (9 pages), Article ID 9871603, Volume 2018 (2018)

Direct-Current Electric Field Distribution in the Brain for Tumor Treating Field Applications: A Simulation Study

Yung-Shin Sun 
Research Article (13 pages), Article ID 3829768, Volume 2018 (2018)

Simulation of Atrial Fibrosis Using Coupled Myocyte-Fibroblast Cellular and Human Atrial Models

Yuan Gao, Yinglan Gong, and Ling Xia
Research Article (10 pages), Article ID 9463010, Volume 2017 (2018)

Computational FEM Model, *Phantom* and *Ex Vivo* Swine Breast Validation of an Optimized Double-Slot Microcoaxial Antenna Designed for Minimally Invasive Breast Tumor Ablation: Theoretical and Experimental Comparison of Temperature, Size of Lesion, and SWR, Preliminary Data

Geshel David Guerrero López, Mario Francisco Jesús Cepeda Rubio, José Irving Hernández Jáquez, Arturo Vera Hernandez, Lorenzo Leija Salas, Francisco Valdés Perezgasga, and Francisco Flores García
Research Article (11 pages), Article ID 1562869, Volume 2017 (2018)

Research Article

Stimulation Strategies for Tinnitus Suppression in a Neuron Model

Alessandra Paffi , **Francesca Camera** , **Chiara Carocci**,
Francesca Apollonio , and **Micaela Liberti** 

Sapienza University of Rome, Via Eudossiana 18, 00184 Rome, Italy

Correspondence should be addressed to Micaela Liberti; liberti@diet.uniroma1.it

Received 29 December 2017; Revised 16 April 2018; Accepted 6 June 2018; Published 30 July 2018

Academic Editor: György Thuróczy

Copyright © 2018 Alessandra Paffi et al. This is an open access article distributed under the Creative Commons Attribution License, which permits unrestricted use, distribution, and reproduction in any medium, provided the original work is properly cited.

Tinnitus is a debilitating perception of sound in the absence of external auditory stimuli. It may have either a central or a peripheral origin in the cochlea. Experimental studies evidenced that an electrical stimulation of peripheral auditory fibers may alleviate symptoms but the underlying mechanisms are still unknown. In this work, a stochastic neuron model is used, that mimics an auditory fiber affected by tinnitus, to check the effects, in terms of firing reduction, of different kinds of electric stimulations, i.e., continuous wave signals and white Gaussian noise. Results show that both white Gaussian noise and continuous waves at tens of kHz induce a neuronal firing reduction; however, for the same amplitude of fluctuations, Gaussian noise is more efficient than continuous waves. When contemporary applied, signal and noise exhibit a cooperative effect in retrieving neuronal firing to physiological values. These results are a proof of concept that a combination of signal and noise could be delivered through cochlear prosthesis for tinnitus suppression.

1. Introduction

Tinnitus is a debilitating perception of sound in the absence of external auditory stimuli that affects more than 10% of the world population [1–3] and tends to increase with the age [2, 3].

The origin of this debilitating disorder may be central or peripheral; i.e., it can originate in the cochlea, in the primary hearing cortex or in any other point of the auditory pathway [4].

Based on frequency and permanence of sound perception, tinnitus is classified in continuous low frequency tinnitus (CLFT) for frequencies below 100 Hz, continuous high frequency tinnitus (CHFT) for frequencies above 3 kHz, and transient spontaneous tinnitus (TST) [5]. Several studies [6, 7] confirm that the CHFT is the most widespread tinnitus typology, generally associated with a reduction of cochlear functionality at high frequency, due to a damage of the basal section of the cochlea. In the tonotopic organization of sound perception [8], the cochlea basal section encodes for high frequency stimuli, above 3 kHz.

This close association between tinnitus and hearing loss suggests that, in many cases, it is due to an impairment of the outer hair cells (OHC) of the cochlear basal section that, in turn, induces a pathologic state of depolarization of the inner hair cells (IHC) [9].

In 1995 Le Page [9] proposed a cochlear model to explain tinnitus origin. The OHCs determine the hair deflection of the IHCs that, in turn, depolarize the acoustic fibers. In physiologic conditions, in the absence of an external stimulus, the OHCs fix the operating point on the IHC transfer function (acoustic neuron depolarization versus IHC hair deflection) to a position that brain recognizes as absence of sound. When the OHCs are damaged, the control input to the IHCs gets lost with a consequent shift of the operating IHC point and a permanent firing rate of the acoustic fiber interpreted by the brain as a real acoustic pattern [9].

This modification of the nerve fiber firing pattern due to OHC impairment was experimentally observed in different animal models [10–13].

Several experimental studies [14–16] revealed that an electric stimulation of the cochlea, delivered through cochlear

prosthesis or transtympanic electrode, could alleviate tinnitus perception in a significant percentage of treated patients. McKerrow and colleagues [14] used continuous wave (CW) high frequency signals (2-6 MHz) superposed to a Gaussian white noise (GWN), whereas other authors used pulse trains with repetition frequency up to 5 kHz [15, 17]. Recently, Tyler and colleagues [18] efficiently used pulsed modulated signals delivered to the Vagus nerve on human volunteers.

However, the electric signals delivered in stimulation, in terms of type (CW, pulse train, white noise), frequency content, amplitude, and modulation, were empirically chosen and their mechanisms of action on the auditory fibers were not defined.

Moving from a recent study by the authors [19] showing an inhibitory effect of an electric exogenous stimulation on a hyperexcited neuronal network model, it was hypothesized that an electric stimulation may interfere with the neuron firing pattern of a pathologically polarized acoustic neuron by reducing its firing rate to the physiologic one.

Aim of this work is to verify such a hypothesis and to study the efficacy of a combination of signal and noise in tinnitus inhibition, using a simple model of a hyperexcited auditory fiber.

In a biomedical perspective, the final aim is to deliver this stimulation to the auditory nerve using cochlear prosthesis to suppress tinnitus in patients with acoustic impairment.

2. Models and Methods

2.1. Neuron Model. To describe the single Ranvier node of an auditory fiber, a stochastic Hodgkin-Huxley (HH) model was used [20–22]. In this model, the neuronal membrane patch is represented by an electrical equivalent, in which the balance of the currents per unit area is given by

$$C_m \frac{dV}{dt} = -g_l(V - E_l) - g_K(V - E_K) - g_{Na}(V - E_{Na}) + I_0 \quad (1)$$

where C_m is the unit area capacitance that takes into account the dielectric properties of the membrane phospholipidic bilayer, V is the transmembrane potential, g_{Na} , g_K , g_l are sodium, potassium and leakage conductances per unit area, respectively, and E_{Na} , E_K , E_l are the reversal potentials of the corresponding current densities. Finally, I_0 is the bias current density that controls the transition between the resting state and the firing activity of the neuron [23]. For the deterministic HH model at 6.3°C, the threshold value above which the neuron starts its firing activity is equal to 6.3 $\mu\text{A}/\text{cm}^2$ [23].

Despite the model limitation concerning the operating temperature equal to 6.3°C, it is simple, very well characterized in terms of neuronal response as a function of model parameters, and the most used in different applications, with more than 10000 citations in the Scopus database [24], so that it can be considered as a golden standard when a new hypothesis has to be tested. Moreover, the possibility of including channel gating stochasticity allowed us to realistically model

channel noise which is particularly relevant in the auditory fibers, due to their small size [25, 26].

To account for the random gating of sodium and potassium channels, the ionic current densities $I_{Na} = g_{Na}(V - E_{Na})$ and $I_K = g_K(V - E_K)$ were calculated using a channel-state-tracking algorithm [27, 28] where Markov chains [27, 29] modeled independent gating particles belonging to each ionic channel.

The magnitude of fluctuations in current densities (channel noise) depends on the number of ionic channels and, thus, for fixed channel densities ($\rho_{Na}=60$ channels/ μm^2 , $\rho_K=18$ channels/ μm^2), on the area of the considered membrane patch. Specifically, channel noise is inversely proportional to the square root of the number of ionic channels in the membrane patch [21, 30]. Acoustic fibers are characterized by small Ranvier nodes, whose size may vary from 2.2 [25] to 15.7 μm^2 [26] and thus by high levels of intrinsic channel noise. In this work, three patch areas were considered: 2.2, 11.0, and 15.7 μm^2 , corresponding to the maximum, the minimum, and an intermediate fiber size.

Besides Na, K, and leakage current densities, I_0 represents here the background level of stimulation coming from the OHCs. This current density determines the firing rate of the neuron, i.e., the operating point on the IHC transfer function.

To simulate different states of pathologic neuron depolarization, I_0 was set to a value close to the threshold: 6 $\mu\text{A}/\text{cm}^2$ and to suprathreshold values: 7 and 10 $\mu\text{A}/\text{cm}^2$ [23]. Conversely, physiological spontaneous firing of the auditory fiber was modeled by using a subthreshold bias current density I_0 equal to 2 $\mu\text{A}/\text{cm}^2$. With respect to this physiological condition, the other conditions increased the background firing activity from 30 to 80%, as suggested by experimental recordings in animals with induced tinnitus [12, 13].

In this paper, for each patch area, four bias currents densities were used: 2, 6, 7, and 10 $\mu\text{A}/\text{cm}^2$. The first value was used to model a healthy acoustic fiber; the other ones modeled paroxysmal excitation underlying tinnitus.

The model was run in the C++ environment using the forward Euler integration method with time step 10 μs .

In principle, the HH model extends its validity up to frequencies that short-circuit the membrane capacitance. According to [31], this occurs above the beta relaxation frequency of the cell membrane, at about 100 MHz. Moreover, the ionic channel modeling using Markov chains [32] is valid if the sampling time is much longer than the channel protein transition time (order of ps) [33]. The used time step of 10 μs imposes a practical limitation of 50 kHz to the maximum frequencies that can be studied with the model. This is well below the theoretical frequency limitations of the model previously discussed.

For each studied condition, 300 independent runs of the model, 1 s in duration, were considered. The number of runs was approximately the number of afferent fibers contemporary stimulated by a single electrode of the cochlear prosthesis; this number was calculated by considering the size of the electrode (0.3 mm), the diameter of a IHC ($\approx 10 \mu\text{m}$), and the number of auditory fibers (≈ 10) contacting a single IHC.

TABLE 1: Mean firing rate (spikes/s) exhibited by the neuron model for different bias current densities I_0 and patch areas in the absence of external electric stimulation.

Patch area (μm^2)	Sub-threshold (physiologic)	Close to threshold (pathologic)	Supra-threshold (pathologic)	
	$I_0=2 \mu\text{A}/\text{cm}^2$	$I_0=6 \mu\text{A}/\text{cm}^2$	$I_0=7 \mu\text{A}/\text{cm}^2$	$I_0=10 \mu\text{A}/\text{cm}^2$
2.2	53.7	64.9	66.8	72.2
11.0	44.5	57.8	60.7	67.2
15.7	42.1	56.5	59.3	66.2

2.2. *Stimulation.* The exogenous stimulation was introduced in the model as an additional voltage over the membrane potential [34–36]. In terms of equivalent HH electric circuit, the electric stimulus was represented as a voltage generator in series with the membrane capacitor and the ionic conductances per unit area [37–40].

The applied electric stimulation was either a CW or a zero-mean GWN or a combination of both.

It should be noticed that the CW is a deterministic signal completely characterized by amplitude (A) and frequency (f), whereas the GWN, being a stochastic process, is described by its statistic moments, namely, average value, variance (σ_N^2), and autocorrelation function.

The GWN had zero-mean value, flat spectrum, and variance values: $\sigma_N^2=3, 25, 100 \text{ mV}^2$. The variance can be associated with the average power that the process dissipates on a 1Ω resistance. The CW signal was chosen to have amplitude values: $A=1.73, 5, 10 \text{ mV}$, equal to the standard deviations (σ_N) of the considered GWN processes, where σ_N was taken as a measure of the amplitude of noise fluctuations. The CW frequencies were chosen to be equal to 25, 35, 50 kHz

because they are above the upper perception threshold of human hearing (20 kHz). Due to the time step of $10 \mu\text{s}$ chosen for the model solution, 50 kHz is the maximum frequency allowed for an input signal. For the same reason, even the GWN spectrum is practically limited to that upper frequency.

After separately studying the two kinds of stimulation, all combinations of the CW signals and the GWN were applied to the model to check possible cooperative effects.

2.3. *Quantification of Firing Reduction.* As already mentioned in Introduction, a pathologic acoustic fiber exhibits a spontaneous firing rate higher than that of a healthy neuron [12, 13]. The mean firing rate, i.e., the number of spikes per second, is due to the operating point fixed by the OHC and to the endogenous noise related to the number of ionic channels. To quantify the level of firing inhibition, and thus of tinnitus suppression, induced by the electric stimulation, it is necessary to introduce a sensitive technique.

In this work, the inactivation function (IA) was defined as follows:

$$IA = \frac{\#spike(\sigma_N = 0; A = 0; f = 0; I_0 = 6, 7, 10) - \#spike(\sigma_N \neq 0; A \neq 0; f \neq 0; I_0 = 6, 7, 10)}{\#spike(\sigma_N = 0; A = 0; f = 0; I_0 = 6, 7, 10) - \#spike(\sigma_N = 0; A = 0; f = 0; I_0 = 2)} \times 100 \quad (2)$$

where $\#spike(\sigma_N=0; A=0; f=0; I_0=6, 7, 10)$ is the number of spikes per second of a pathologic neuron ($I_0=6, 7, 10 \mu\text{A}/\text{cm}^2$) in the absence of exogenous electric stimulation ($\sigma_N=0 \text{ mV}$; $A=0 \text{ mV}$; $f=0 \text{ Hz}$); $\#spike(\sigma_N \neq 0; A \neq 0; f \neq 0; I_0=6, 7, 10)$ is the number of spikes per second of a pathologic neuron during the exogenous electric stimulation ($\sigma_N \neq 0 \text{ mV}$; $A \neq 0 \text{ mV}$; $f \neq 0 \text{ Hz}$); $\#spike(\sigma_N=0; A=0; f=0; I_0=2)$ is the number of spikes per second of a healthy neuron ($I_0=2 \mu\text{A}/\text{cm}^2$) in the absence of exogenous electric stimulation ($\sigma_N=0 \text{ mV}$; $A=0 \text{ mV}$; $f=0 \text{ Hz}$).

This quantity furnishes the percentage of firing reduction obtained using the stimulation in the pathologic neuron with respect to the difference, in terms of firing activity, between a pathologic and a physiologic neuron. The inactivation function will be 0% if the stimulation does not change the number of spikes of pathologic neuron and 100% if the neuron activity is turned back to the physiologic one. In this latter case, tinnitus is considered completely suppressed. Inactivation could be also higher than 100% if the firing activity is reduced

below the physiologic condition or negative if the effect of electric stimulation is excitatory instead of inhibitory.

3. Results

3.1. *Spontaneous Firing.* The used stochastic neuron model exhibits a firing activity, quantified by the mean firing rate (spikes per second), that increases with the bias current density I_0 injected in the model, as shown in Table 1. Even in subthreshold conditions (see second column of Table 1) a not null firing rate is observed, due to the energy injected into the system by channel noise, that increases as the Ranvier node area becomes smaller (Table 1).

The neuron firing rate is due to the contemporary presence of channel noise and bias current density; the first one is determined by the typical sizes of the acoustic Ranvier nodes, the second one accounts for the operating point set by the OHC on the IHC transfer function, according to [9].

As shown in Table 1, for the same patch area, the three bias current densities, used to mimic the neuron with tinnitus (pathologic condition), increase the firing activity with respect to the physiologic condition, here modeled using the subthreshold bias current density $I_0=2 \mu\text{A}/\text{cm}^2$. These increases range from 21% ($I_0=6 \mu\text{A}/\text{cm}^2$) to 35% ($I_0=10 \mu\text{A}/\text{cm}^2$), for the $2.2 \mu\text{m}^2$ patch area, from 25% ($I_0=6 \mu\text{A}/\text{cm}^2$) to 40% ($I_0=10 \mu\text{A}/\text{cm}^2$), for the $11.0 \mu\text{m}^2$ patch area, and from 35% ($I_0=6 \mu\text{A}/\text{cm}^2$) to 57% ($I_0=10 \mu\text{A}/\text{cm}^2$), for the $15.7 \mu\text{m}^2$ patch area (Table 1). This shows that when channel noise decreases, in correspondence of larger patch areas, bias current densities assume a stronger influence on neuron firing.

The increased firing activity obtained by using the close to threshold and the suprathreshold current densities reported in Table 1 agrees with the experimental recordings on animals with induced tinnitus, reporting an increase from 35 to 83% [12, 13].

In the next sections, it will be examined the efficacy of different exogenous electric stimulations (see Section 2.2) in reducing the firing activity of pathologic neurons down to physiologic conditions.

3.2. Effect of Different Electric Stimulations. The effects of a GWN on the mean firing rate of the neuron model, in each operating condition, have been quantified by the inactivation function IA, defined in Section 2.3, and summarized in Figure 1. For each pathologic condition, Figure 1 shows inactivation versus patch area for three standard deviations σ_N of noise fluctuations: 1.73 mV (panel (a)), 5 mV (panel (b)), and 10 mV (panel (c)).

For the lowest σ_N (Figure 1(a)), the inactivation does not exceed 2% and, in some cases, assumes negative values, indicating an increase of the mean firing frequency instead of a reduction. For σ_N of 5 mV (Figure 1(b)) it is possible to observe higher inactivation values that increase with the patch area and decrease with the bias current density, reaching a value of about 10% for patch size $15.7 \mu\text{m}^2$ and bias current density $6 \mu\text{A}/\text{cm}^2$. However, such values are too low to induce considerable tinnitus alleviation. Further increasing σ_N up to 10 mV (Figure 1(c)), the inactivation could become considerable, reaching 53% for the highest patch area and the smallest bias current density. However, the inactivation is just some percent points for the smallest patch area, where the endogenous channel noise dominates on the exogenous stimulation in determining the neuron firing rate.

Therefore, a standard deviation of 10 mV is necessary for the GWN to induce an inactivation from 26 to 53% in acoustic fibers whose Ranvier nodes are larger than $11 \mu\text{m}^2$.

However, a broadband stimulation with a quite high power, related to the variance of noise fluctuations, may in principle induce unwanted acoustic perceptions coming from neighboring healthy hear cells.

Thus, it is worth evaluating the effect of using a stimulation with comparable amplitude of noise at a single frequency (CW) above 20 kHz, the upper perception limit of the human hearing. In fact, this stimulation cannot be directly interpreted as a sound by the human auditory system.

Figure 2(a) shows the inactivation versus the bias current density for the larger patch area (best case) and an applied CW at 25 kHz and amplitude equal to 1.73, 5, or 10 mV. As discussed in Section 2.2, these amplitudes have been chosen to have the same standard deviation of the used GWNs.

Even in this case, the signal with 1.73 mV of amplitude is not efficient in inhibiting firing and that of 5 mV inactivates the neuron up to 10%. The effect becomes considerable for the 10 mV signal, when the inactivation is equal to 18% for $I_0=10 \mu\text{A}/\text{cm}^2$ and reaches a maximum of 35% for $I_0=6 \mu\text{A}/\text{cm}^2$. As already noticed for the GWN stimulation, the inactivation decreases with the bias current density, i.e., with the background firing activity of the pathologic neuron.

To evaluate the sensitivity to different stimulation frequencies, also 35 and 50 kHz CW signals have been considered. Figure 2(b) shows the inactivation induced by 25 kHz, 35 kHz and 50 kHz CW signals with the amplitude set to 10 mV.

It is worth noticing that the CW is almost ineffective at 50 kHz, being the inactivation always less than 20%, whereas 25 kHz and 35 kHz signals behave in a similar way, with a slightly better performance of the 25 kHz CW. This evidences a frequency sensitivity of the neuron already observed also in a lower frequency range (50-500 Hz) [41, 42].

Results of simulations show that the GWN, having the standard deviation equal to the sinusoidal amplitude, is always more efficient than the 25 kHz CW in inducing firing reduction. Figure 3 compares the inactivations induced by these two exogenous stimulations in the best case ($I_0=6 \mu\text{A}/\text{cm}^2$; patch area= $15.7 \mu\text{m}^2$). Although the inactivation values are very similar when both the noise standard deviation (σ_N) and the signal amplitude (A) are equal to 1.73 and 5 mV, for $\sigma_N=10$ mV the inactivation induced by GWN is 52% versus 35% obtained by using the 25 kHz CW signal with the same amplitude. In fact, while the CW inactivation trend versus the amplitude (purple line in Figure 3) is accurately approximated ($R=0.99976$) by a quadratic curve with the second-order coefficient equal to 0.35, in the case of GWN (orange line in Figure 3), the quadratic function which best fits the inactivation trend ($R=0.99964$) has a second-order coefficient equal to 0.64.

To obtain 100 % inactivation, too high amplitude values for the CW signal would be necessary; conversely GWN has the disadvantage of having a spectrum segment in the auditory frequency band.

For these reasons, it would be useful to combine in a suitable way these two kinds of stimulation.

3.3. Effects of Combined Stimulation. The question arises on what happens if monochromatic and white stimulations are combined.

Results of the combined stimulation have been compared to the superposition of the effects induced by the two stimulations applied individually. Figure 4 shows a comparison of inactivation obtained by combining the two kinds of stimulation IA(CW+GWN) with the sum of the inactivations obtained by using the two single stimulations

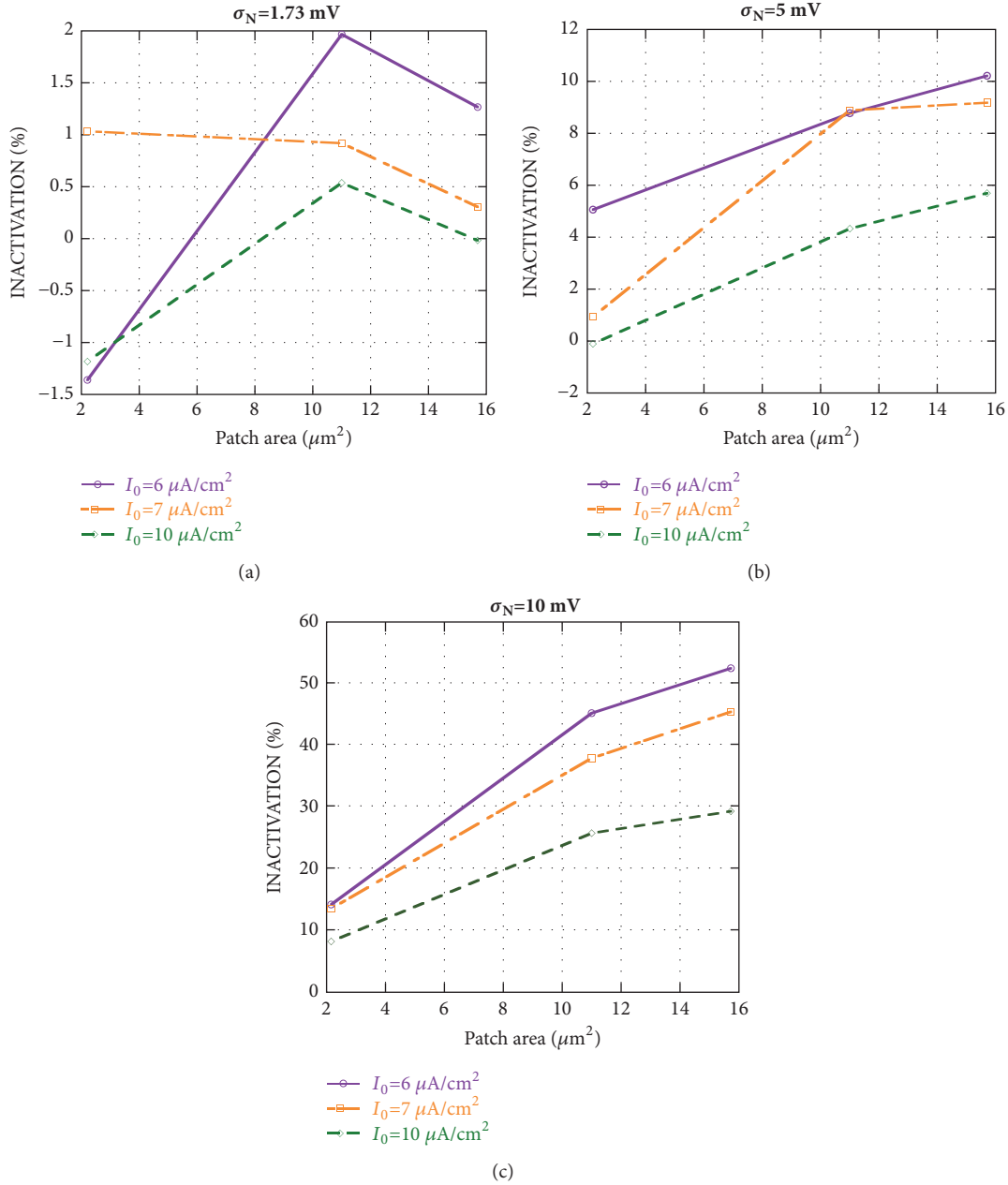


FIGURE 1: Inactivation versus patch area for different bias current densities I_0 . The exogenous stimulation is given by a Gaussian white noise GWN with different standard deviations: $\sigma_N = 1.73$ mV (panel (a)), $\sigma_N = 5$ mV (panel (b)), and $\sigma_N = 10$ mV (panel (c)).

IA(CW)+IA(GWN), in the best case: CW at 25 kHz with amplitude 10 mV, and GWN with $\sigma_N = 10$ mV.

As evident from Figure 4, except for the lowest patch area and $I_0 = 6 \mu\text{A}/\text{cm}^2$, IA(CW+GWN) is always higher than IA(CW)+IA(GWN) and, for $I_0 = 6 \mu\text{A}/\text{cm}^2$ and patch area $15.7 \mu\text{m}^2$, it reaches 100%. This means that the firing rate of the stimulated neuron is reduced to physiologic conditions.

These results, due to the nonlinear neuronal behavior, show a cooperative effect of the applied signal and noise that can be usefully exploited in applications. So, a good stimulation solution could be a combination of CW and

GWN to maximize tinnitus suppression while reducing possible side effects.

4. Discussion

Results of this work furnish a proof of concept that a suitable exogenous electrical stimulation, consisting of a high frequency (25-35 kHz) CW and/or Gaussian noise, can alleviate tinnitus through a mechanism of firing inhibition. This finding is coherent with studies on human volunteers, where the electrical stimulation was delivered to the cochlea [14-16], and suggests a possible interaction mechanism based on

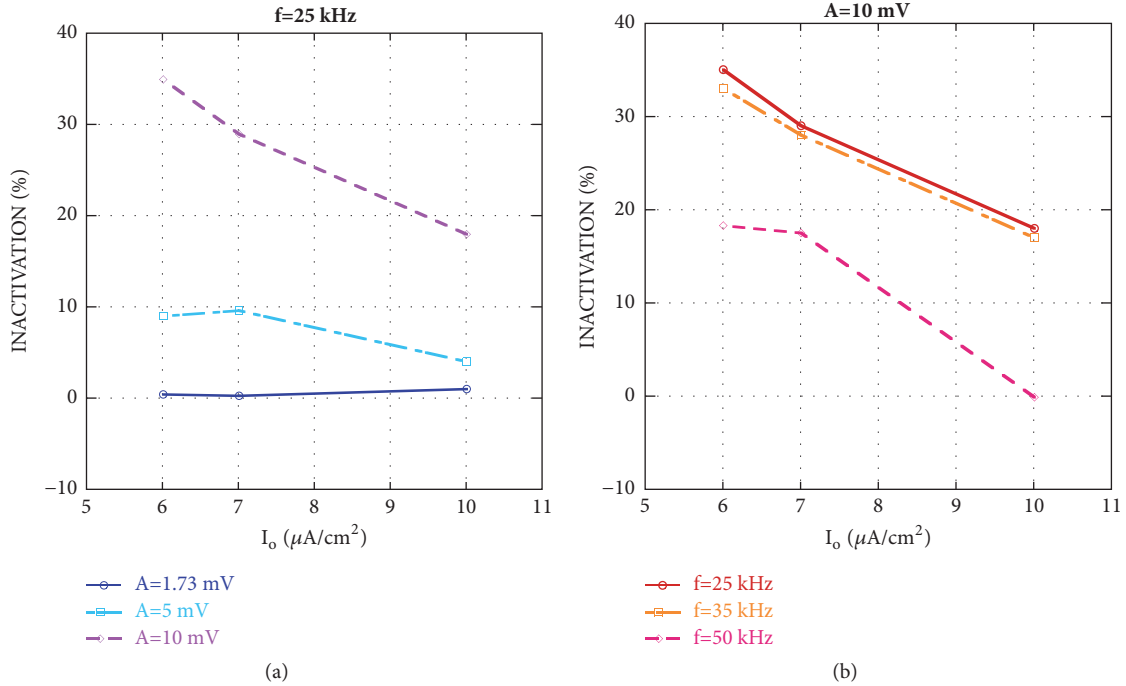


FIGURE 2: Inactivation versus bias current density I_0 for a patch area equal to $15.7\ \mu\text{m}^2$. The exogenous stimulation is given by a CW at 25 kHz and amplitudes 1.73 mV, 5 mV, and 10 mV (panel (a)) or a CW of amplitude 10 mV and frequencies 25 kHz, 35 kHz, and 50 kHz (panel (b)).

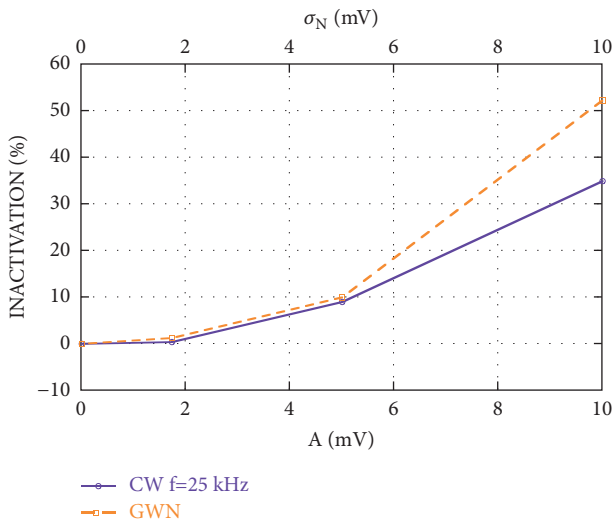


FIGURE 3: Inactivation induced by the CW stimulation versus the amplitude A of the CW at 25 kHz (purple solid line) and inactivation induced by the GWN stimulation versus its standard deviation σ_N (orange dashed line); A and σ_N assume the same values; $I_0=6\ \mu\text{A}/\text{cm}^2$; patch area= $15.7\ \mu\text{m}^2$.

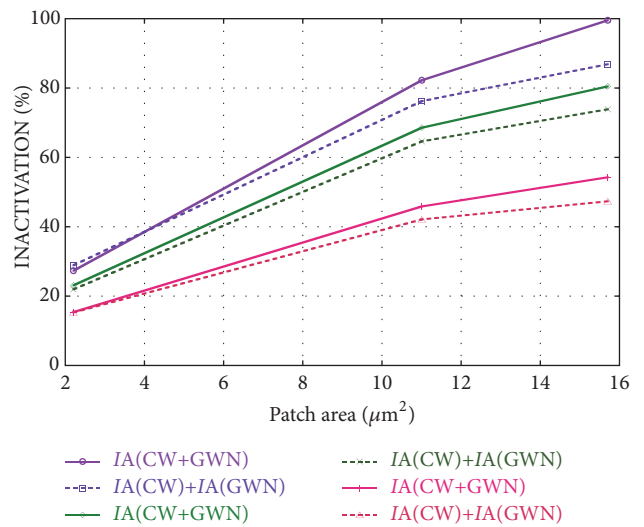


FIGURE 4: Inactivation IA versus patch area for $I_0=6\ \mu\text{A}/\text{cm}^2$ (purple lines), $I_0=7\ \mu\text{A}/\text{cm}^2$ (green lines), and $I_0=10\ \mu\text{A}/\text{cm}^2$ (magenta lines), obtained by combining the CW at 25 kHz 10 mV and the GWN, $\sigma_N=10\text{ mV}$ (solid lines), compared with the superposition of the inactivations induced by the two stimulations applied individually (dashed lines).

the reduction of the pathologic firing rate to the spontaneous activity of a healthy auditory fiber.

To simulate the single Ranvier node of an auditory fiber, a stochastic HH neuron model was used, since it is well characterized and considered as a reference model in the literature for a lot of different applications with more than

10000 citations in the Scopus database [24]. The authors themselves already used it to study neuronal encoding [37, 38, 42, 43] and to explain the analgesic effect of the Complex Neuroelectromagnetic Pulse [44] by means of a silencing mechanism [19].

A limitation of the used model is that, even if a temperature correction factor is used [45], it cannot work at the mammalian temperature of 37°C. In the HH model, a temperature increase causes the threshold current density to shift towards higher values, and the firing rate to change depending on the patch size [45]. So, different operating conditions, in terms of bias current densities, would mimic healthy and pathologic neuronal activities. Similar mechanisms of relative firing reduction are expected to occur for a suitable combination of signal and noise since the model anyway presents two attraction basins for firing and resting states and the exogenous stimulation can push the system from one state to the other. However, since the temperature adjustment in neuronal models is still an open question, here it was preferred to use the well-assessed reference temperature for the HH model.

Due to the generality of the used model and the high number of degrees of freedom, a complete evaluation of the uncertainty budget is not practicable but, besides the temperature, the other main variables that may influence results are examined in the following.

An aspect that could contribute to the uncertainty of results is that, for frequencies above 10 kHz, the membrane capacitance per unit area (C_m) is not constant, differently from what was assumed in our model. In fact, the permittivity of the cell membrane decreases with frequency due to the relaxation of the alpha polarization phenomenon [46]. Nevertheless, our simplification is largely acceptable since the frequency dependence of C_m was shown to have a negligible effect on the stimulation threshold of a HH model (median = 1.4%) [47].

Other model parameters that induce a great variability of results are the bias current density I_0 and the patch area. When applying a combination of the CW ($f=25$ kHz, $A=10$ mV) and the GWN ($\sigma_N=10$ mV) to the neuronal patch of $15.7 \mu\text{m}^2$, the inactivation ranges from 54% ($I_0=10 \mu\text{A}/\text{cm}^2$) to 100% ($I_0=6 \mu\text{A}/\text{cm}^2$). Conversely, for $I_0=6 \mu\text{A}/\text{cm}^2$, the inactivation passes from 28% to 100% if the patch size increases from 2.2 to $15.7 \mu\text{m}^2$. Such variations could explain the great variability of results on human volunteers [16] that could be attributed to the individual variability of auditory fiber size (patch area in the model) and tinnitus severity (bias current density in the model).

This study suggests a plausible mechanism of tinnitus suppression using exogenous electrical excitation and is a first step towards the characterization of kind and parameters of stimulation that maximize the efficacy while reducing possible short-term or long-term side effects, such as unwanted sound perception or adaptation.

To control side effects, charge-balanced signals should be used and the induced currents should not exceed typical currents used in cochlear prostheses. A recent dosimetric study [48] revealed that a typical cochlear implant delivered, at the location of the afferent fibers of the auditory nerve, a peak voltage of several tens of mVs, higher than the signal amplitudes used in this work (≤ 10 mV). This suggests that the stimulation signals used in this work are plausible to be released from cochlear implants without severe side effects,

even though it will be necessary to conduct a careful risk analysis to assess the safety of the proposed technique.

5. Conclusions

A stochastic HH neuron model was used to evaluate the efficacy of different electric stimulation strategies in tinnitus suppression. The used stimulations were CW signals at different frequencies in the range of tens of kHz and GWN.

Results of simulations show that both a CW and a white noise, applied individually to the neuron model, may induce a firing inhibition. The inactivation level is shown to depend on many parameters, such as patch area, bias current density, CW frequency and amplitude, and noise standard deviation. The more the background activity is low (larger patch size and lower bias currents), the more the inactivation is high. Considerable inactivation values are obtained by using either CW at 25 or 35 kHz or GWN with 10 mV of standard deviation, but GWN is shown to be more efficient than CW (IA=53% versus IA=35% in the best condition) for a comparable amplitude of fluctuations.

Moreover, the inactivation induced by a combination of signal and noise is almost always higher than the sum of the inactivations induced by the two stimulations applied individually and it reaches 100% for the lowest I_0 and the highest patch area.

These results are a proof of concept that signal and noise act on the neuron in a cooperative way and could be suitably delivered in combination through cochlear prosthesis to alleviate tinnitus while reducing possible side effects due to a broadband stimulation.

Future works will concern the validation of the presented results on a mammalian neuronal model at 37°C, such as the Spatially Extended Nonlinear Node (SENN) [49] and the McIntyre-Richardson-Grill (MRG) [50] models and the identification of a colored stimulating noise suitably filtered considering the typical frequency selectivity of the used model.

Disclosure

This work was partially performed within the context of the European COST EMF-MED Action BM1309. Preliminary results were presented at the Joint Annual Meeting of the Bioelectromagnetics Society and the European BioElectromagnetics Association, Ghent, Belgium, 2016.

Conflicts of Interest

The authors report no conflicts of interest. The authors alone are responsible for the content and writing of the paper.

References

- [1] K. Brunger, "Managing tinnitus," *The Journal of Family Health Care*, vol. 18, no. 2, pp. 47-48, 2008.
- [2] J. Shargorodsky, G. C. Curhan, and W. R. Farwell, "Prevalence and characteristics of tinnitus among US adults," *American Journal of Medicine*, vol. 123, no. 8, pp. 711-718, 2010.

- [3] B. Scott and P. Lindberg, "Psychological profile and somatic complaints between help-seeking and non-help-seeking tinnitus subjects," *Psychosomatics*, vol. 41, no. 4, pp. 347–352, 2000.
- [4] H. P. Zenner, M. Pfister, and N. Birbaumer, "Tinnitus sensitization: Sensory and psychophysiological aspects of a new pathway of acquired centralization of chronic tinnitus," *Otology & Neurotology*, vol. 27, no. 8, pp. 1054–1063, 2006.
- [5] G. Baracca, L. Del Bo, and U. Ambrosetti, "Tinnitus and hearing loss," in *Textbook of Tinnitus*, A. R. Møller, B. Langguth, D. De Ridder, and T. Kleinjung, Eds., pp. 285–291, Springer, New York, NY, USA, 2011.
- [6] C. Nicolas-Puel, T. Akbaraly, R. Lloyd et al., "Characteristics of tinnitus in a population of 555 patients: Specificities of tinnitus induced by noise trauma," *International Tinnitus Journal*, vol. 12, no. 1, pp. 64–70, 2006.
- [7] F. Martines, D. Bentivegna, E. Martines, V. Sciacca, and G. Martinciglio, "Characteristics of tinnitus with or without hearing loss: Clinical observations in Sicilian tinnitus patients," *Auris Nasus Larynx*, vol. 37, no. 6, pp. 685–693, 2010.
- [8] G. Ehret, "Tonotopic organization (maps)," in *Encyclopedia of Neuroscience*, pp. 4083–4088, 2009.
- [9] E. L. Le Page, "A model for cochlear origin of subjective tinnitus: excitatory drift in the operating point of inner hair cells," in *Mechanisms of Tinnitus*, J. A. Vernon and A. R. Møller, Eds., pp. 115–148, Allyn and Bacon, London, 1995.
- [10] A. J. Noreña, M. Tomita, and J. J. Eggermont, "Neural changes in cat auditory cortex after a transient pure-tone trauma," *Journal of Neurophysiology*, vol. 90, no. 4, pp. 2387–2401, 2003.
- [11] A. J. Noreña and J. J. Eggermont, "Changes in spontaneous neural activity immediately after an acoustic trauma: implications for neural correlates of tinnitus," *Hearing Research*, vol. 183, no. 1–2, pp. 137–153, 2003.
- [12] J. A. Kaltenbach, "Tinnitus: models and mechanisms," *Hearing Research*, vol. 276, no. 1–2, pp. 52–60, 2011.
- [13] P. G. Finlayson and J. A. Kaltenbach, "Alterations in the spontaneous discharge patterns of single units in the dorsal cochlear nucleus following intense sound exposure," *Hearing Research*, vol. 256, no. 1–2, pp. 104–117, 2009.
- [14] W. S. Mckerrow, C. E. Schreiner, M. M. Merzenich, R. L. Snyder, and J. G. Toner, "Tinnitus suppression by cochlear implants," *Annals of Otolaryngology, Rhinology & Laryngology*, vol. 100, no. 7, pp. 552–558, 1991.
- [15] J. T. Rubinstein, R. S. Tyler, A. Johnson, and C. J. Brown, "Electrical suppression of tinnitus with high-rate pulse trains," *Otology & Neurotology*, vol. 24, no. 3, pp. 478–485, 2003.
- [16] J. E. Chang and F. Zeng, "Tinnitus suppression by electric stimulation of the auditory nerve," *Frontiers in Systems Neuroscience*, vol. 6, article 19, 2012.
- [17] F.-G. Zeng, Q. Tang, A. Dimitrijevic, A. Starr, J. Larky, and N. H. Blevins, "Tinnitus suppression by low-rate electric stimulation and its electrophysiological mechanisms," *Hearing Research*, vol. 277, no. 1–2, pp. 61–66, 2011.
- [18] R. Tyler, A. Cacace, C. Stocking et al., "Vagus Nerve Stimulation Paired with Tones for the Treatment of Tinnitus: A Prospective Randomized Double-blind Controlled Pilot Study in Humans," *Scientific Reports*, vol. 7, no. 1, 2017.
- [19] F. Camera, A. Paffi, A. W. Thomas et al., "The CNP signal is able to silence a supra threshold neuronal model," *Frontiers in Computational Neuroscience*, vol. 9, Article 44, pp. 1–11, 2015.
- [20] A. L. Hodgkin and A. F. Huxley, "A quantitative description of membrane current and its application to conduction and excitation in nerve," *The Journal of Physiology*, vol. 117, no. 4, pp. 500–544, 1952.
- [21] E. Schneidman, B. Freedman, and I. Segev, "Ion Channel Stochasticity May Be Critical in Determining the Reliability and Precision of Spike Timing," *Neural Computation*, vol. 10, no. 7, pp. 1679–1703, 1998.
- [22] J. R. Clay and L. J. DeFelice, "Relationship between membrane excitability and single channel open-close kinetics," *Biophysical Journal*, vol. 42, no. 2, pp. 151–157, 1983.
- [23] E. M. Izhikevich, *Dynamical Systems in Neuroscience: The Geometry of Excitability and Bursting*, MIT Press, Cambridge, UK, 2006.
- [24] Scopus database, (<https://www.scopus.com>).
- [25] F. Rattay, "Basics of hearing theory and noise in cochlear implants," *Chaos, Solitons & Fractals*, vol. 11, no. 12, pp. 1875–1884, 2000.
- [26] H. Mino and W. M. Grill Jr., "Effects of stochastic sodium channels on extracellular excitation of myelinated nerve fibers," *IEEE Transactions on Biomedical Engineering*, vol. 49, no. 6, pp. 527–532, 2002.
- [27] H. Mino, J. T. Rubinstein, and J. A. White, "Comparison of algorithms for the simulation of action potentials with stochastic sodium channels," *Annals of Biomedical Engineering*, vol. 30, no. 4, pp. 578–587, 2002.
- [28] J. H. Goldwyn, N. S. Imennov, M. Famulare, and E. Shea-Brown, "Stochastic differential equation models for ion channel noise in Hodgkin-Huxley neurons," *Physical Review E: Statistical, Nonlinear, and Soft Matter Physics*, vol. 83, no. 4, 2011.
- [29] J. T. Rubinstein, "Threshold fluctuations in an N sodium channel model of the node of Ranvier," *Biophysical Journal*, vol. 68, no. 3, pp. 779–785, 1995.
- [30] J. A. White, J. T. Rubinstein, and A. R. Kay, "Channel noise in neurons," *Trends in Neurosciences*, vol. 23, no. 3, pp. 131–137, 2000.
- [31] C. Merla, M. Liberti, F. Apollonio, and G. D'inzeo, "Quantitative assessment of dielectric parameters for membrane lipid bilayers from rf permittivity measurements," *Bioelectromagnetics*, vol. 30, no. 4, pp. 286–298, 2009.
- [32] E. Neher and B. Sakmann, "Single-channel currents recorded from membrane of denervated frog muscle fibers," in *A Century of Nature: Twenty-One Discoveries that Changed Science and the World*, L. Garwin and T. Lincoln, Eds., 2003.
- [33] P. Marracino, M. Liberti, E. Trapani et al., "Human aquaporin 4 gating dynamics under perpendicularly-oriented electric-field impulses: A molecular dynamics study," *International Journal of Molecular Sciences*, vol. 17, no. 7, article no. 1133, 2016.
- [34] C. Merla, A. Denzi, A. Paffi et al., "Novel passive element circuits for microdosimetry of nanosecond pulsed electric fields," *IEEE Transactions on Biomedical Engineering*, vol. 59, no. 8, pp. 2302–2311, 2012.
- [35] F. Apollonio, M. Liberti, A. Paffi et al., "Feasibility for microwaves energy to affect biological systems via nonthermal mechanisms: a systematic approach," *IEEE Transactions on Microwave Theory and Techniques*, vol. 61, no. 5, pp. 2031–2045, 2013.
- [36] A. Denzi, C. Merla, P. Camilleri et al., "Microdosimetric study for nanosecond pulsed electric fields on a cell circuit model with nucleus," *Journal of Membrane Biology*, vol. 246, no. 10, pp. 761–767, 2013.
- [37] A. Paffi, F. Apollonio, G. d'inzeo, and M. Liberti, "Stochastic resonance induced by exogenous noise in a model of a neuronal

- network,” *Network: Computation in Neural Systems*, vol. 24, no. 3, pp. 99–113, 2013.
- [38] A. Paffi, F. Camera, F. Apollonio, G. D’Inzeo, and M. Liberti, “Restoring the encoding properties of a stochastic neuron model by an exogenous noise,” *Frontiers in Computational Neuroscience*, vol. 9, Article 42, pp. 1–11, 2015.
- [39] T. Y. Tsong and R. D. Astumian, “Electroconformational coupling and membrane protein function,” *Progress in Biophysics and Molecular Biology*, vol. 50, no. 1, pp. 1–45, 1987.
- [40] H. Mino, J. T. Rubinstein, C. A. Miller, and P. J. Abbas, “Effects of electrode-to-fiber distance on temporal neural response with electrical stimulation,” *IEEE Transactions on Biomedical Engineering*, vol. 51, no. 1, pp. 13–20, 2004.
- [41] F. Liu, J. Wang, and W. Wang, “Frequency sensitivity in weak signal detection,” *Physical Review E: Statistical, Nonlinear, and Soft Matter Physics*, vol. 59, no. 3, pp. 3453–3460, 1999.
- [42] S. Orcioni, A. Paffi, F. Camera, F. Apollonio, and M. Liberti, “Automatic decoding of input sinusoidal signal in a neuron model: Improved SNR spectrum by low-pass homomorphic filtering,” *Neurocomputing*, vol. 267, pp. 605–614, 2017.
- [43] S. Orcioni, A. Paffi, F. Camera, F. Apollonio, and M. Liberti, “Automatic decoding of input sinusoidal signal in a neuron model: high pass homomorphic filtering,” *Neurocomputing*, vol. 292, pp. 165–173, 2018.
- [44] A. W. Thomas, M. Kavaliers, F. S. Prato, and K.-P. Ossenkopp, “Antinociceptive effects of a pulsed magnetic field in the land snail, *Cepaea nemoralis*,” *Neuroscience Letters*, vol. 222, no. 2, pp. 107–110, 1997.
- [45] L. Yang and Y. Jia, “Effects of patch temperature on spontaneous action potential train due to channel fluctuations: Coherence resonance,” *BioSystems*, vol. 81, no. 3, pp. 267–280, 2005.
- [46] K. R. Foster and H. P. Schwan, “Dielectric properties of tissues and biological materials: a critical review,” *Critical Reviews in Biomedical Engineering*, vol. 17, pp. 25–104, 1989.
- [47] B. Howell, L. E. Medina, and W. M. Grill, “Effects of frequency-dependent membrane capacitance on neural excitability,” *Journal of Neural Engineering*, vol. 12, no. 5, Article ID 056015, 2015.
- [48] G. Tognola, A. Pesatori, M. Norgia et al., “Numerical modeling and experimental measurements of the electric potential generated by cochlear implants in physiological tissues,” *IEEE Transactions on Instrumentation and Measurement*, vol. 56, no. 1, pp. 187–193, 2007.
- [49] J. P. Reilly and A. M. Diamant, *Electrostimulation Theory, Applications, and Computational Models*, 2011, <http://www.artechhouse.com>.
- [50] C. C. McIntyre, A. G. Richardson, and W. M. Grill, “Modeling the excitability of mammalian nerve fibers: Influence of afterpotentials on the recovery cycle,” *Journal of Neurophysiology*, vol. 87, no. 2, pp. 995–1006, 2002.

Research Article

A Neuromuscular Interface for Robotic Devices Control

Innokentiy Kastalskiy , **Vasily Mironov**, **Sergey Lobov**, **Nadia Krilova** ,
Alexey Pimashkin, and **Victor Kazantsev**

Center for Translational Technologies, Nizhny Novgorod Neuroscience Center, National Research Lobachevsky State University of Nizhny Novgorod, Gagarin Ave. 23, Nizhny Novgorod 603950, Russia

Correspondence should be addressed to Innokentiy Kastalskiy; kastalskiy@neuro.nnov.ru

Received 28 September 2017; Revised 4 May 2018; Accepted 12 June 2018; Published 22 July 2018

Academic Editor: György Thuróczy

Copyright © 2018 Innokentiy Kastalskiy et al. This is an open access article distributed under the Creative Commons Attribution License, which permits unrestricted use, distribution, and reproduction in any medium, provided the original work is properly cited.

A neuromuscular interface (NI) that can be employed to operate external robotic devices (RD), including commercial ones, was proposed. Multichannel electromyographic (EMG) signal is used in the control loop. Control signal can also be supplemented with electroencephalography (EEG), limb kinematics, or other modalities. The multiple electrode approach takes advantage of the massive resources of the human brain for solving nontrivial tasks, such as movement coordination. Multilayer artificial neural network was used for feature classification and further to provide command and/or proportional control of three robotic devices. The possibility of using biofeedback can compensate for control errors and implement a fundamentally important feature that has previously limited the development of intelligent exoskeletons, prostheses, and other medical devices. The control system can be integrated with wearable electronics. Examples of technical devices under control of the neuromuscular interface (NI) are presented.

1. Introduction

Development of neurointerface technology is a topical scientific focus, with the demand for such systems driven by the need for humans to communicate with numerous electronic computing and robotic devices (RD), for example, in medical applications such as prosthetic limbs and exoskeletons. At present, multichannel recording of neuromuscular activity and the development of neurointerface applications that implement unique mechanisms for high-dimensional data processing are areas of major interest.

One of the most suitable signals aiming at controlling external RDs is electromyographic (EMG) activity. Multichannel signals from the human peripheral nervous system have been previously successfully used to control external devices and novel methods of EMG acquisition and control strategies have recently been implemented [1–8]. When controlling anthropomorphic RD, the human pilot independently coordinates and plans the trajectory of motion using the massive computing power of the human brain [9, 10]. The use of afferent neural pathways allows the activation of biological feedback; using this principle is fundamentally

important to the development of rehabilitation exoskeletons, prostheses, and various other medical applications.

The disadvantages of using EMG interfaces in rehabilitation are the presence of muscle fatigue and insufficient residual muscle activity. On the other hand electroencephalographic (EEG) interfaces proved to be the best due to a direct link to the nervous system by measurement of brain activity during therapy [11, 12]. The brain mechanisms that enable humans to facilitate the control of external devices remain largely unknown. However, despite this knowledge gap, appropriate collection, detection, and classification can enable brain-controlled signals from the human body to be utilized for highly efficient and even intelligent control of multiparameter RDs. But brain-machine interfaces (BMI) have some limitations such as low reliability and accuracy when it comes to complex functional task training.

A possible solution to these problems is the combined use of the advantages of both types of interfaces. Such interfaces are called hybrid, for example, hybrid BMI (hBMI); the use of EMG input here can lead to a more accurate classification of EEG patterns [13–15]. However, the task of developing an EMG interface is still relevant.

Considering the problem of motion recognition and decoding of EMG signals, note that there are several generally applicable methods of software signal processing: linear discriminant analysis (LDA) [20], support vector machines (SVM) [21], artificial neural networks (ANN) [22], fuzzy algorithms [22, 23], etc.

Despite significant progress in the field of machine learning and its application in medical tasks [24], algorithms are still based on applying ANN technologies and solving optimization problems. Creation of a universal algorithm that can adapt to different conditions in a technical control system was proven theoretically impossible, at least in the context of existing theories [25, 26]. Compared to traditionally controlled electronic devices, neurocontrolled devices may offer the advantage of adapting due to human brain plasticity.

The present study focuses on the development of methods and technologies for remote control of RDs in specific applications. The objective was to integrate human bioelectrical signals into a control loop. Online collection and interpretation of multisite EMG signals were performed to control a variety of robotic systems. Technical solutions were developed to associate patterns of muscular activity (and human brain, if possible) with the commands to the controlled object by employing a user-defined translation algorithm. EMG interface solution is driven by multilayer ANN feature classifier. User-defined programmable function translates sensory signals into motor commands to successfully control a variety of existing commercial RDs.

2. Methods

2.1. EMG Array. Multielectrode array (EMG array) was designed as a data acquisition system that detects the EMG signals associated with wrist gestures. Monitoring of the signals from several muscles was performed simultaneously (for example, the muscles of the forearm, involved in making gestures: *m. brachioradialis*, *m. flexor carpi radialis*, *m. palmaris longus*, *m. flexor carpi ulnaris*, etc.). First layout contained six pairs of standard medical Ag/AgCl electrodes, which are often used for surface EMG recording. The electrodes were placed on the flexible fabric, which was put on the forearm at a distance of about 1/3 from the elbow to the wrist. The EMG array was suitable for several hours of recording.

An array was developed using commercial technology of printing circuit board (PCB) flexible electronics: flexible substrate made of polyimide with six pairs of silver-coated (99.9% silver) planar electrodes (Figure 1(a)). Registration was performed in bipolar mode; i.e., the muscle signal was obtained by pairs of electrodes. The reference electrode was mounted close to the elbow. An example of EMG signal on one electrode is shown in Figure 1(b).

2.2. Multichannel Signal Registration and Classification Using an Artificial Neural Network. Ten healthy volunteers aged 20 to 42 years were recruited for experimental purpose. All persons had different physique (asthenic: 1, hypersthenic: 2, and normosthenic: 7) and had no previous experience in dealing with EMG interfaces. Two series of nine gestures each were performed in a random order.

Next, registered signals for nine static hand gestures, such as motor patterns, were classified. The first series was the learning set; the second series was the testing set. The data flow (EMG amplitudes) $\mathbf{x}(t) \in \mathbb{R}^6$ was divided into 200 ms overlapping time windows at a 100 ms step ($t = 0, 1, 2, \dots$ is the discrete time with the sampling rate of 1 kHz). Then the moving root mean square (RMS) values of the EMG signal along each channel independently over time were calculated in order to extract the features of the multichannel signal.

$$RMS(t) = \sqrt{\frac{1}{N} \sum_{n=0}^{N-1} \mathbf{x}(t-n)^2}, \quad (1)$$

where $N = 200$ is the number of samples in a time window and $t = Mk$ ($k = 2, 3, 4, \dots$) with $M = 100$ being the time shift between consecutive windows. Each 50 ms RMS was fed to a multilayer artificial neural network (ANN) for feature classification.

The network neurons apply weighted sum over inputs, z_i , and use sigmoidal activation function (2) to generate output, y :

$$y = \frac{1}{1 + e^{-\sum_i w_{ij} z_i}}, \quad (2)$$

where w_{ij} are the synaptic weights of neuron j . The learning, i.e., adjustment of the neuron weights \mathbf{w} , is achieved by the backpropagation algorithm [27]. During the learning, the weight w_{ij} is corrected proportionally to the error δ_j introduced by the neuron j when the current sample is fed to the network input:

$$\Delta w_{ij} = \eta \delta_j x_i, \quad (3)$$

where η is learning rate and x_i is the signal from neuron i to neuron j . Running through the network of all samples makes up an epoch. As a rule, a large number of epochs are required for training. Each basic gesture corresponds to a single target class. Thus, each neuron of the last layer should produce “1” for one class and “0” for the others.

The classification error was calculated for the training and testing sets as the rate of incorrectly recognized samples. It served as a criterion to stop the learning procedure as soon as the error started increasing on test samples. On average the learning process required about 5000 training epochs and took less than 1 min on a standard Intel Core i5 PC.

Once the learning is deemed finished, online controlling of a robotic device can be enabled. To introduce a proportional control an approach similar to that described in [8] was employed. The muscle effort is evaluated by the mean absolute value (MAV) averaged over all EMG sensors:

$$MAV(t) = \frac{1}{NK} \sum_{k=1}^K \sum_{n=0}^{N-1} |x_k(t-n)|, \quad (4)$$

where K is the number of EMG channels (in our case $K = 6$). Then the actuator’s rotation speed is set proportional to the MAV.

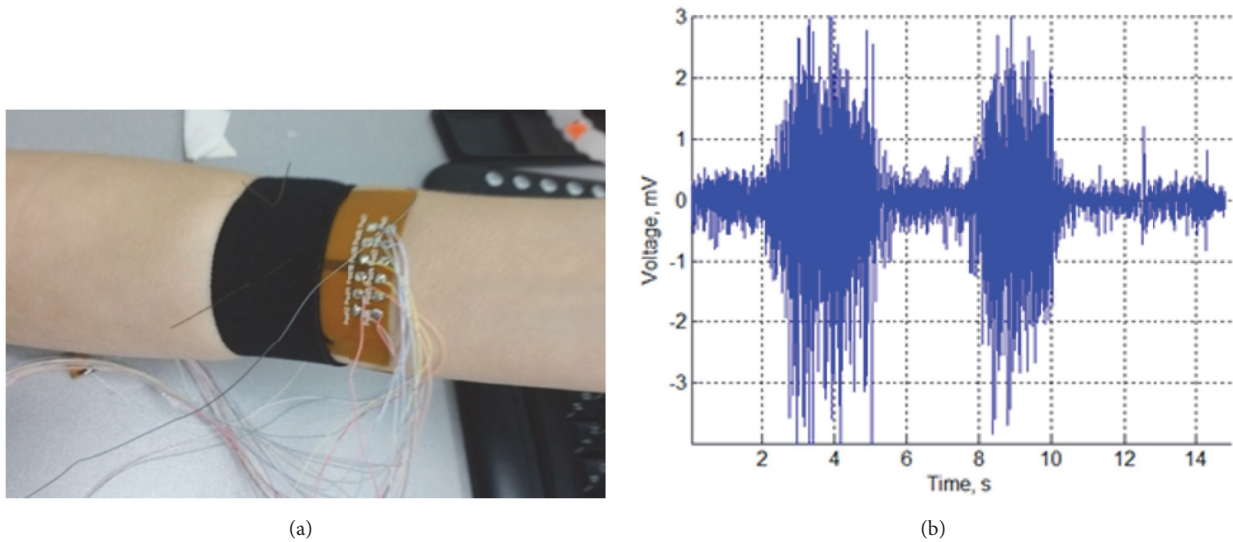


FIGURE 1: Multielectrode array for EMG signal recording. (a) Medical Ag/AgCl electrodes of the flexible EMG array used to record the muscles activity. (b) EMG signal from one electrode of the array. Signal contains two periods of muscle contraction.

2.3. Software and Tested Robotic Devices. The RDs tested in this study were the LEGO NXT Mindstorms mobile robot (LEGO, Denmark) [7, 8], the NAO humanoid robot (Aldebaran, France), and an exoskeleton “Ilya Muromets” (UNN, Russia) [28]. The standard software development kits (SDKs) of each device were used. The connections between the control device and tested RDs were wireless: Bluetooth for LEGO or Wi-Fi for NAO and the exoskeleton. If the SDK had a support of movement instructions, a direct macrocommand was sent (e.g., “go forward” for the NAO and exoskeleton). Otherwise, the required macrocommands were implemented by the software and sent to the elementary command of the device (e.g., “rotate motor A with speed x%” for LEGO).

To configure the parameters of the signal translator, a special software module was developed (Figure 2). The software contains GUI interface that allows creating a test bed configuration. Various modules can be added and a different modules relationship configuration can be set up. Also, the operator has the ability to change the specific settings for each module.

Three types of modules are used: input modules, processing modules, and executor modules. Each output of any input module can be connected to one or more free input slots of any processing module, and likewise each output of any processing module can be connected to one or more free input slots of any executor module.

The input modules provide an interface with data acquisition devices, such as EMG and EEG adapters. One of the tasks of input modules is preprocessing (filtering, resampling) of incoming data and their normalization. The normalized data is then transferred to the processing unit with which this input module was connected in the “Configurator” (Figure 2(b)).

The processing modules perform the classification tasks based on the selected algorithm. The result of the classifier operation is the number of the recognized pattern, which is

transmitted to the corresponding module of the executive device.

The executive device module is a driver that communicates with the executive device and converts the pattern number received from the processing module into a command sequence of a particular device to perform the desired action.

3. Results

3.1. EMG Data Acquisition. The parameters of the EMG signal recorded using NI were comparable to similar systems described in the literature [4, 16, 19, 29–31]. The design of the electrode array enabled stable signal recording and could potentially be used to further develop neurointerfaces for prosthetic limb control in medical and rehabilitation applications or commercial interfaces for everyday use.

One of the most important characteristics of the hardware amplifier of NI is the low noise of the raw signal. In the case of the input signal with approximate amplitude of 100 mV a mean signal-to-noise-ratio (SNR) was 11.9 ± 0.5 dB, for 200 mV – 19.3 ± 0.7 dB, and for 500 mV – 29.2 ± 0.9 dB. Series of SNR values measured experimentally showed stability of this characteristic but in the majority of cases such a level cannot be considered very high. However, normal values in these signal amplifiers (usually 50 dB and more) are indicated for measurements performed in ideal conditions.

3.2. ANN Parameters Optimization. To optimize ANN performance, gesture recognition on the same datasets of EMG signals (patterns of the RMS signals) was performed. The number of layers in the ANN, the number of neurons in hidden layers, and the learning rate were varied. The ANN error dropped significantly between one and two layers and then slightly increased as the number of layers increased up to eight, while learning time increased significantly. A similar increase in ANN error was obtained as the number

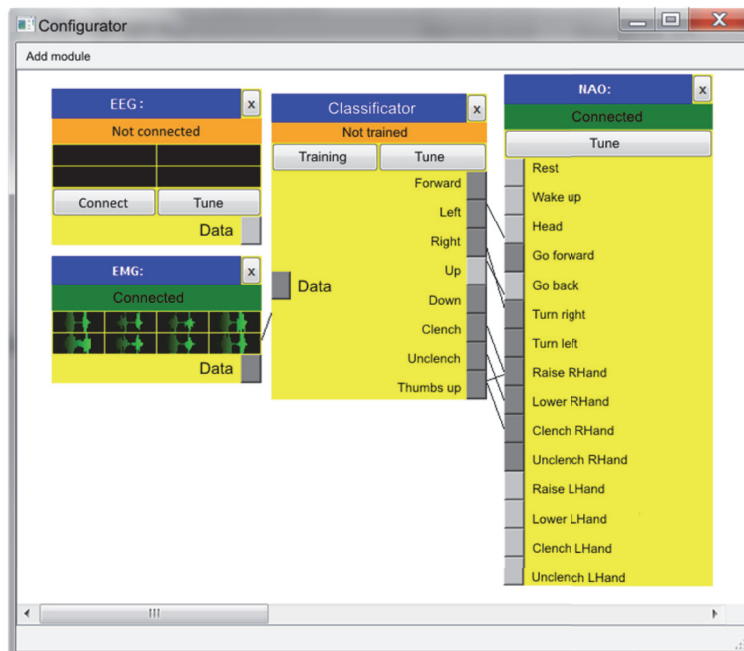
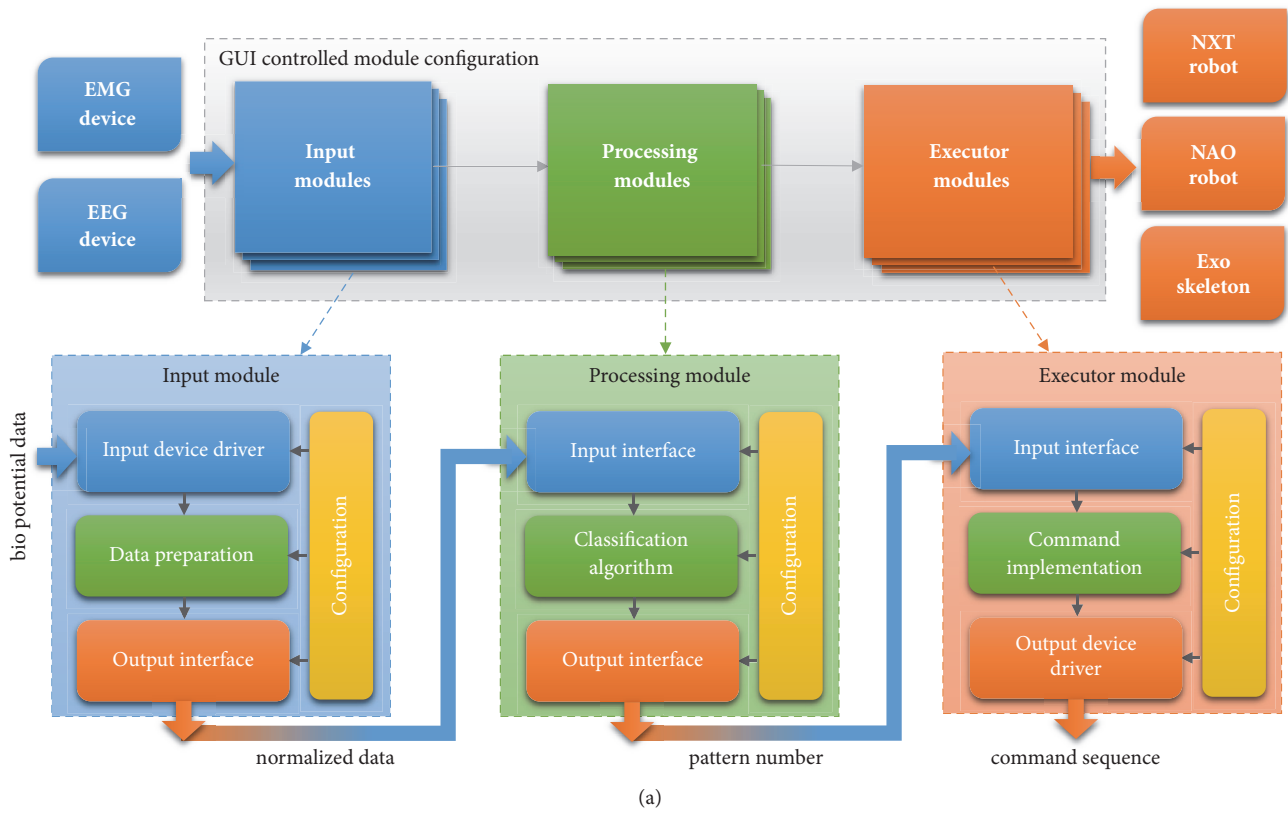


FIGURE 2: The “Configurator” for the programmable translator of NI. (a) Flow chart. (b) Main window of the software module. It allows for setting the modalities for processing and the type of translation of the input signal of the human pilot to the output one on device actuators.

TABLE I: Comparison of various myoelectric control devices.

Indicator measured	NI	Fougner et al., 2012, [16]	Wurth et al., 2014, [17]	Jiang et al., 2012, [18]	Hahne et al., 2014, [19]	Hahne et al., 2016, [4]	Earley et al., 2016, [6]
Average recognition accuracy	92.5%	-	96%	>90%	-	~90%	-
Control	Command and proportional	Consistent proportional	Motion pattern recognition. Proportional	Proportional	Proportional	Command and proportional	Motion pattern recognition. Proportional
Classifier	ANN (perceptron)	LDA	LDA	ANN (perceptron)	ANN (perceptron)	Linear regression	LDA
Number of gestures / degrees of freedom (DoF)	9 gestures	5 gestures	2 DoF, 5 gestures	3 DoF	2 DoF, 4 gestures	2 DoF, 4 gestures	8 gestures
Number of EMG channels /sensors	8 for recording + 1 reference	5	6	7 pairs for each forearm	192-channel electrode array in the monopolar configuration	4 for each type of electrode	12 pairs of bipolar electrodes

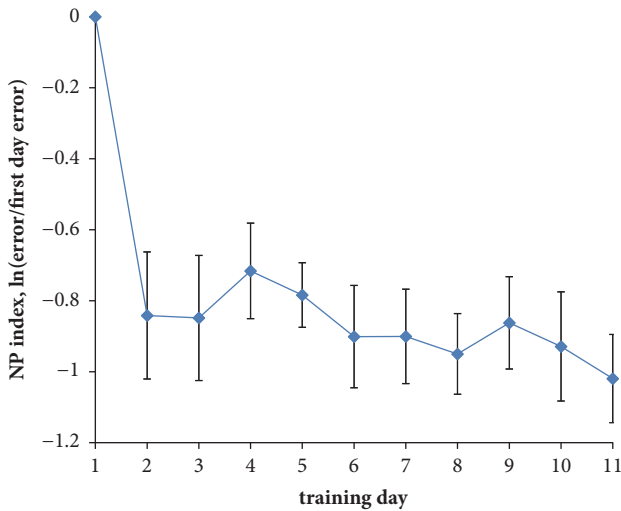


FIGURE 3: Evolution of neurointerface performance (NP index) during training. Averaged data for 10 users are shown. Error bars correspond to standard deviations.

of neurons in the hidden layers increased from 8 to 16. Thus, a network with two layers and eight neurons in the hidden layer was selected for further experiments. It was also found that a learning rate of 0.01 led to optimal learning error and learning time. This is learning rate dimensionless parameter of standard backpropagation algorithm. Thus, this learning rate was used in all experimental tests of the interface.

3.3. Neuromuscular Interface Performance. The software and hardware system implement both command control based on pattern classification and proportional control based on muscle effort estimation. Several schemes for combining these strategies were previously suggested [7, 32]. In particular, the

patterns for controlling direction of movement and muscle effort to control speed were recognized.

Note that personal classification accuracy varied significantly [33]. For example, the accuracy of recognition for nine patterns for ten users ranged from 86.5 to 98.5%. In this regard, the possibility of improving personal performance by training the user was explored.

To measure the personal progress an index of neurointerface performance (NP) was introduced:

$$NP = \ln \left(\frac{E_i}{E_1} \right), \quad (5)$$

where E_i is the error of EMG pattern classification on the current training day and E_1 is the error on the first day. Note that on the first day NP is equal to 0 always. A positive NP value means degradation of the interface performance, and a negative value means an improvement.

Eight of the ten subjects showed a positive improvement in performance after several days of training including playing a training game with the EMG interface. Figure 3 illustrates the improvement in terms of NP index. The majority of progress was achieved on the second day of training. This is acceptable, given that a short training course would be necessary before any user could effectively operate an EMG interface. Our previous study reported the accuracy of the pattern classification algorithm used in this NI was $92\% \pm 4\%$ for the nine gestures and $97\% \pm 2\%$ for six gestures in the command control mode [32]. This high accuracy rate is very close to the attainable limit (“error-free”) in the development of human-machine interfaces.

A detailed comparison of the characteristics of NI developed in this study and other devices is shown in Table 1.

Neuromuscular interface consisted of an EMG module that permitted control of external RDs, including existing commercial ones, using muscle effort patterns. In the future, our device could also be improved by adding an EEG module

that permits control of RDs using both brain intention and EMG patterns.

Overall, the hardware and software system described in this study could successfully interpret the bioelectric activity signals from the pilot into robotic commands to achieve correct control of the tested RDs.

4. Discussion

Trying to develop an ideal human-machine interface, one must keep in mind and improve not only its technical component. It requires understanding how much a person can limit system performance. Despite a relatively high mean fidelity, neurointerfaces still exhibit strong variance in the accuracy of gesture recognition among different users. Our recent study showed that the factors determining the performance of neurointerfaces were the degree of muscle cooperation and the amount of the body fatty tissue. A person can improve his/her performance in the long run by doing sports or fitness (nonspecific training) or even in a short period of time training with NI (specific training) [33]. It is crucial to identify “problematic” gestures.

In this study, users were informed of their errors in execution of gestures, and as a result, on the second day of testing, their performance improved. Outside the study remains an important question about the motivation. In our experiments, a significant drop in motivation was observed already on the second week. Most likely, people who really need a NI (for example, amputees) will be able to show a more impressive dynamics of training.

One of the drawbacks of the proposed NI hardware implementation is the wire communication channel of the EMG array. It is not suitable for long-term unconstrained use. However, it can be overcome by developing a portable amplifier with a wireless transmitter driven by Bluetooth 4.0 protocol. The latter has high noise immunity and low requirements to the electromagnetic environment. In this embodiment, the sensors will be quite more cumbersome, but there will be no hand obstructions or electrode wires imposing constraints on allowable movements.

Nevertheless, the use of high-density surface electromyography (HDEMG) [3] can bring the approach greater solidity. It can add redundancy and is more immune from movement artifacts (electrode slippage, etc.), with the potential to significantly improve decoding reliability.

On the other hand the disadvantage of a HDEMG is its high power consumption. But advanced algorithms of active channel selection can lead to low power consumption per channel, which enables operation for long periods of time on miniature batteries.

In the future the NI can be conveniently embedded into wearable garments and worn unobtrusively by the operator. No extra setup time is required for placement of individual electrodes, fine alignment, etc.

The functioning of a device combining EMG and EEG modalities imposes certain difficulties in implementing the control strategy. Such an implementation is seen as promising in the case of rehabilitation of severe motor impairment. EEG should be used as a trigger to confirm of a movement

execution. The output of the gesture recognition can be mapped into various command libraries for different control modes.

Being designed for either medical rehabilitation or general consumer, the NI must have characteristics that take into account the fundamental computational aspects of the brain. Employment of brain information processing power in control applications still has many questions debated. On the one hand, possibilities of modern electronics together with advanced ANN classification algorithms permit achieving quite fast rather precise multiparameter human-machine interfaces as has been demonstrated in the present study. On the other hand, the NI power is still limited by ultimate need of human concentration to implement the proportional control. The development of advance training algorithms and tools to monitor pilot’s concentration during control gives challenges for further work in this direction. Another, more fundamental question is how many parameters and external devices one pilot can navigate simultaneously? Theoretically, the number of muscles of the body simultaneously controlled by the brain is huge. For example, a simple grasping finger movement involves up to 50 muscles [34]. They represent muscle synergies that consisted of groups of muscles worked in a coherence to implement a given motor task.

In this context in nearest future, feasibly, properly configured multisite EMG human-machine interface will be able to provide adaptive control in real time of many parameters/limbs/actuators including ones with remote control. In other words, nervous system (e.g., the peripheral one) will be integrated with machine controllers and interpreted by brain as “natural” extension of the body. To work like that different feedback channels in addition to purely biological feedback (e.g., visual, olfactory) might be needed to develop.

Further research in this direction not only has obvious applied perspective in rehabilitation medicine and industrial robotics but also will shed light on fundamental principles of motor control implemented by our brain.

5. Conclusions

A technical solution for collecting, decoding, and translating multichannel biometric data to control a variety of external RDs was described. Novel algorithms for the classification of human bioelectric activity patterns were developed. In particular, the approach to implement muscle activity patterns classification using artificial neural network was proposed. It permitted classifying up to nine patterns with very high average accuracy (98.5% for some persons) relative to other systems.

Experimental tests of developed recording and decoding system were performed. During operational testing, NI functioned correctly when controlling existing commercial RDs such as the Aldebaran Robotics NAO and an exoskeleton for the lower limbs.

Conflicts of Interest

The authors declare that there are no conflicts of interest regarding the publication of this article.

Acknowledgments

This work was funded by the Russian Foundation for Basic Research (RFBR) according to the Research Project no. 16-29-08437.

References

- [1] F. Negro, S. Muceli, A. M. Castronovo, A. Holobar, and D. Farina, "Multi-channel intramuscular and surface EMG decomposition by convolutive blind source separation," *Journal of Neural Engineering*, vol. 13, no. 2, Article ID 026027, 2016.
- [2] M. Ison, I. Vujaklija, B. Whitsell, D. Farina, and P. Artemiadis, "High-density electromyography and motor skill learning for robust long-term control of a 7-DoF robot arm," *IEEE Transactions on Neural Systems and Rehabilitation Engineering*, vol. 24, no. 4, pp. 424–433, 2016.
- [3] E. Martinez-Valdes, C. M. Laine, D. Falla, F. Mayer, and D. Farina, "High-density surface electromyography provides reliable estimates of motor unit behavior," *Clinical Neurophysiology*, vol. 127, no. 6, pp. 2534–2541, 2016.
- [4] J. M. Hahne, D. Farina, N. Jiang, and D. Liebetanz, "A novel percutaneous electrode implant for improving robustness in advanced myoelectric control," *Frontiers in Neuroscience*, vol. 10, article 114, 2016.
- [5] Z. Tang, K. Zhang, S. Sun, Z. Gao, L. Zhang, and Z. Yang, "An upper-limb power-assist exoskeleton using proportional myoelectric control," *Sensors*, vol. 14, no. 4, pp. 6677–6694, 2014.
- [6] E. J. Earley, L. J. Hargrove, and T. A. Kuiken, "Dual window pattern recognition classifier for improved partial-hand prosthesis control," *Frontiers in Neuroscience*, vol. 10, article 58, 2016.
- [7] S. Lobov, N. Krilova, I. Kastalskiy, V. Kazantsev, and V. A. Makarov, "A human-computer interface based on electromyography command-proportional control," in *Proceedings of the 4th International Congress on Neurotechnology, Electronics and Informatics, NEUROTECHNIX 2016*, SCITEPRESS 1, pp. 57–64, November 2016.
- [8] S. A. Lobov, V. I. Mironov, I. A. Kastalskiy, and V. B. Kazantsev, "Combined use of command-proportional control of external robotic devices based on electromyography signals," *Sovremennye Tehnologii v Medicine [Modern Technologies in Medicine]*, vol. 7, no. 4, pp. 30–38, 2015.
- [9] J. M. Carmenta, M. A. Lebedev, R. E. Crist et al., "Learning to control a brain-machine interface for reaching and grasping by primates," *PLoS Biology*, vol. 1, no. 2, pp. 193–208, 2003.
- [10] D. Farina, R. Merletti, and R. M. Enoka, "The extraction of neural strategies from the surface EMG," *Journal of Applied Physiology*, vol. 96, no. 4, pp. 1486–1495, 2004.
- [11] A. Ramos-Murguialday, D. Broetz, M. Rea et al., "Brain-machine interface in chronic stroke rehabilitation: a controlled study," *Annals of Neurology*, vol. 74, no. 1, pp. 100–108, 2013.
- [12] E. López-Larraz, F. Trincado-Alonso, V. Rajasekaran et al., "Control of an ambulatory exoskeleton with a brain-machine interface for spinal cord injury gait rehabilitation," *Frontiers in Neuroscience*, vol. 10, article 359, 2016.
- [13] A. Sarasola-Sanz, N. Irastorza-Landa, E. López-Larraz et al., "A hybrid brain-machine interface based on EEG and EMG activity for the motor rehabilitation of stroke patients," in *Proceedings of the 2017 International Conference on Rehabilitation Robotics, ICORR 2017*, pp. 895–900, July 2017.
- [14] K. Kiguchi and Y. Hayashi, "A study of EMG and EEG during perception-assist with an upper-limb power-assist robot," in *Proceedings of the International Conference on Robotics and Automation 2012*, pp. 2711–2716, 2012.
- [15] X. Li, O. W. Samuel, X. Zhang, H. Wang, F. Peng, and G. Li, "A motion-classification strategy based on sEMG-EEG signal combination for upper-limb amputees," *Journal of NeuroEngineering and Rehabilitation*, vol. 14, no. 1, article 2, 2017.
- [16] A. Fougner, O. Stavadahl, P. J. Kyberd, Y. G. Losier, and P. A. Parker, "Control of upper limb prostheses: terminology and proportional myoelectric control – a review," *IEEE Transactions on Neural Systems and Rehabilitation Engineering*, vol. 20, no. 5, pp. 663–667, 2012.
- [17] S. M. Wurth and L. J. Hargrove, "A real-time comparison between direct control, sequential pattern recognition control and simultaneous pattern recognition control using a Fitts' law style assessment procedure," *Journal of NeuroEngineering and Rehabilitation*, vol. 11, no. 1, article no. 91, 2014.
- [18] N. Jiang, J. L. Vest-Nielsen, S. Muceli, and D. Farina, "EMG-based simultaneous and proportional estimation of wrist/hand kinematics in uni-lateral trans-radial amputees," *Journal of NeuroEngineering and Rehabilitation*, vol. 9, article 92, 2012.
- [19] J. M. Hahne, F. Biebmann, N. Jiang et al., "Linear and nonlinear regression techniques for simultaneous and proportional myoelectric control," *IEEE Transactions on Neural Systems and Rehabilitation Engineering*, vol. 22, no. 2, pp. 269–279, 2014.
- [20] K. Englehart and B. Hudgins, "A robust, real-time control scheme for multifunction myoelectric control," *IEEE Transactions on Biomedical Engineering*, vol. 50, no. 7, pp. 848–854, 2003.
- [21] M. A. Oskoei and H. Hu, "Support vector machine-based classification scheme for myoelectric control applied to upper limb," *IEEE Transactions on Biomedical Engineering*, vol. 55, no. 8, pp. 1956–1965, 2008.
- [22] K. Veer and T. Sharma, "A novel feature extraction for robust EMG pattern recognition," *Journal of Medical Engineering & Technology*, vol. 40, no. 4, pp. 149–154, 2016.
- [23] H. Jahani Fariman, S. A. Ahmad, M. Hamiruce Marhaban, M. Ali Jan Ghasab, and P. H. Chappell, "Simple and computationally efficient movement classification approach for EMG-controlled prosthetic hand: ANFIS vs. artificial neural network," *Intelligent Automation and Soft Computing*, vol. 21, no. 4, pp. 559–573, 2015.
- [24] A. L. Edwards, M. R. Dawson, J. S. Hebert et al., "Application of real-time machine learning to myoelectric prosthesis control: A case series in adaptive switching," *Prosthetics and Orthotics International*, vol. 40, no. 5, pp. 573–581, 2016.
- [25] D. H. Wolpert and W. G. Macready, "No free lunch theorems for optimization," *IEEE Transactions on Evolutionary Computation*, vol. 1, no. 1, pp. 67–82, 1997.
- [26] Y. C. Ho and D. L. Pepyne, "Simple explanation of the no-free-lunch theorem and its implications," *Journal of Optimization Theory and Applications*, vol. 115, no. 3, pp. 549–570, 2002.
- [27] D. E. Rumelhart, G. E. Hinton, and R. J. Williams, "Learning internal representations by error propagation," in *Parallel Distributed Processing*, pp. 318–362, 1985.
- [28] V. Mironov, S. Lobov, I. Kastalskiy, and V. Kazantsev, "Myoelectric control system of lower limb exoskeleton for re-training motion deficiencies," *Lecture Notes in Computer Science*, vol. 9492, pp. 428–435, 2015.
- [29] L. J. Hargrove, K. Englehart, and B. Hudgins, "A comparison of surface and intramuscular myoelectric signal classification," *IEEE Transactions on Biomedical Engineering*, vol. 54, no. 5, pp. 847–853, 2007.

- [30] S. Lee, J. Oh, Y. Kim, M. Kwon, and J. Kim, "Estimation of the upper limb lifting movement under varying weight and movement speed," in *International Journal of Engineering and Industries (ICEI)*, pp. 1–6, 2011.
- [31] M. A. Khoruzhko, G. N. Sesekin, N. V. Boldyreva et al., "A mobile exoskeleton control system using electromyographic signals from human muscles," *Sovremennye Tehnologii v Medicine [Modern Technologies in Medicine]*, vol. 9, no. 4, pp. 162–169, 2017.
- [32] S. Lobov, V. Mironov, I. Kastalskiy, and V. Kazantsev, "A spiking neural network in SEMG feature extraction," *Sensors*, vol. 15, no. 11, pp. 27894–27904, 2015.
- [33] S. Lobov, N. Krilova, I. Kastalskiy, V. Kazantsev, and V. Makarov, "Latent factors limiting the performance of sEMG-interfaces," *Sensors*, vol. 18, article 1122, 2018.
- [34] R. R. Llinas, *I of the vortex: From neurons to self*, 264 p, MIT Press, Cambridge, MA, USA, 2001.

Research Article

Modelling of the Current Density Distributions during Cortical Electric Stimulation for Neuropathic Pain Treatment

S. Fiocchi , E. Chiaramello , P. Ravazzani , and M. Parazzini

CNR Consiglio Nazionale delle Ricerche, Istituto di Elettronica e di Ingegneria dell'Informazione e delle Telecomunicazioni IEIIT, Milan, Italy

Correspondence should be addressed to S. Fiocchi; serena.fiocchi@ieiit.cnr.it

Received 19 September 2017; Accepted 20 February 2018; Published 23 April 2018

Academic Editor: Reinoud Maex

Copyright © 2018 S. Fiocchi et al. This is an open access article distributed under the Creative Commons Attribution License, which permits unrestricted use, distribution, and reproduction in any medium, provided the original work is properly cited.

In the last two decades, motor cortex stimulation has been recognized as a valuable alternative to pharmacological therapy for the treatment of neuropathic pain. Although this technique started to be used in clinical studies, the debate about the optimal settings that enhance its effectiveness without inducing tissue damage is still open. To this purpose, computational approaches applied to realistic human models aimed to assess the current density distribution within the cortex can be a powerful tool to provide a basic understanding of that technique and could help the design of clinical experimental protocols. This study aims to evaluate, by computational techniques, the current density distributions induced in the brain by a realistic electrode array for cortical stimulation. The simulation outcomes, summarized by specific metrics quantifying the efficacy of the stimulation (i.e., the effective volume and the effective depth of penetration) over two cortical targets, were evaluated by varying the interelectrode distance, the stimulus characteristics (amplitude and frequency), and the anatomical human model. The results suggest that all these parameters somehow affect the current density distributions and have to be therefore taken into account during the planning of effective electrical cortical stimulation strategies. In particular, our calculations show that (1) the most effective interelectrode distance equals 2 cm; (2) increasing voltage amplitudes increases the effective volume; (3) increasing frequencies allow enlarging the effective volume; and (4) the effective depth of penetration is strictly linked to both the anatomy of the subject and the electrode placement.

1. Introduction

Neuropathic pain (NP) is defined as pain caused by a lesion or a disease of the central (central neuropathic pain (CNP)) or peripheral (peripheral neuropathic pain (PNP)) somatosensory nervous system [1]. Despite the availability of different drugs, no more than 30–40% patients with chronic NP receive adequate pain reduction ($\geq 50\%$) by currently available drug-based therapies [2, 3].

Among the nonpharmacological treatments, favourable effects of motor cortex stimulation (MCS) upon CNP have been reported [4–10]. This technique is based on the cortical stimulation with biphasic waves of electric current administered through two (the most used bipolar stimulation) or more electrodes. The stimulating electrode is placed over the motor cortex region where the contralateral painful body area is represented [11–13].

Since its first introduction in 1991 [14] for the treatment of thalamic pain, MCS has been applied worldwide on both animals and humans in the attempt to alleviate medically refractory CNP of different origins, such as the facial NP (including trigeminal neuralgia, trigeminal NP, trigeminal deafferentation pain, symptomatic trigeminal neuralgia, and postherpetic neuralgia), the phantom limb pain, the brachial plexus avulsion, the poststroke pain, the Wallenberg syndrome, the pain secondary to multiple sclerosis, and the posttraumatic brain injury pain (to this purpose see the review studies of both animal and human experiments [15–18]). All these studies have been elaborated based on empirical experience given the incomplete understanding of the pathophysiology of CNP and the difficulties to conduct double-blinded studies; therefore, the mechanism underlying the analgesic effect produced by MCS is still largely debated [11, 19, 20].

TABLE 1: Conductivities (S/m) of the head tissues at different stimulation frequencies [36, 37].

Tissue	Conductivity (S/m)			
	40 Hz	50 Hz	85 Hz	130 Hz
Air internal	0	0	0	0
Artery, blood vessels, vein	0.7	0.7	0.7	0.7
Mandible, marrow red, skull, teeth, vertebrae	0.0201	0.0201	0.0201	0.0201
Brain grey matter, hippocampus, hypothalamus, thalamus	0.0681	0.0753	0.0869	0.0915
Brain white matter, commissure	0.0506	0.0533	0.0573	0.0590
Cartilage, ear cartilage, intervertebral disks, cerebellum	0.171	0.171	0.172	0.172
Cerebrospinal Fluid (CSF)	0.0881	0.0953	0.107	0.111
Connective tissue, tendon, ligament	2	2	2	2
Cornea,	0.263	0.270	0.295	0.322
Muscle	0.421	0.421	0.422	0.422
Ear skin, skin	0.224	0.233	0.259	0.278
Eye lens,	0.0002	0.0002	0.0002	0.0002
Eye sclera	0.321	0.321	0.322	0.323
Eye vitreous humor	0.503	0.503	0.503	0.503
Fat, subcutaneous adipose tissue (SAT)	1.5	1.5	1.5	1.5
Hypophysis, pineal body	0.0188	0.0196	0.0206	0.0210
Medulla oblongata, midbrain, pons	0.521	0.521	0.522	0.523
Mucosa	0.0594	0.0643	0.0721	0.0753
Nerve, spinal cord	0.00042	0.00043	0.00045	0.00048
Tongue	0.0269	0.0274	0.0280	0.0281
	0.271	0.271	0.272	0.272

However, the most accredited theories addressing pain relief by MCS (for a review see [21]) attribute its efficacy to the neural modulation, given by the flow of current density in the motor cortex [22]. It is indeed believed that the electrical stimulation of the motor cortex inhibits, disrupts, or interferes with the allogenic signals coming from the thalamus and from other hyperactive areas in the brain networks that govern the nociception [14, 23].

In this context, the MCS delivered “dose,” here intended as the current density quantification in the cortex and in the neural tissues, should be considered one of the key points for both the treatment optimization and a deeper understanding of the mechanisms lying behind its efficacy [24].

So far, studies addressing the characterization of the current density distributions due to MCS are scarce and limited to the analysis of different electrode types [25, 26] and/or placed on very simplified cortical models [12, 27–30].

In this study a precise quantification, using computational techniques and appropriately defined metrics, of the current density distributions in the brain of different-aged detailed anatomical human models was conducted. This was performed by reproducing the model of a realistic electrode array for MCS [31] used in clinic and placed on the motor cortex target area that corresponds to the somatic area of pain. Typically, for most of the clinical applications for the neuropathic pain treatment [18], these coincide with facial and upper limb cortical areas, placed in the lower part and in the middle part of the central gyrus, respectively. The

electrode array was fed according to the typical frequency and voltage amplitude delivered in the medical practice [7, 9, 10, 32, 33] and the extent to which they affect specific current density-related parameters was quantified. The rigorous analysis of these parameters in realistic and detailed human head models could ultimately help to gain further insights into the evaluation of the clinical outcomes and the optimization of the treatment delivered through the MCS.

2. Materials and Methods

2.1. Human Models. Three realistic anatomical male models of the Virtual Population Family [34, 35] (Duke, 34 years old; Louis, 14 years old; and Glenn, 84 years old) were used in the study. They were obtained by the segmentation of high-resolution magnetic resonance (MR) images of healthy volunteers and then reconstructed based on a computer-aided design representation of the organ surfaces.

The use of these different anatomical models allowed assessing the characteristics of the current density distributions in three different brain morphologies. In each of them, more than 40 tissues can be distinguished at the head level (head tissues list in Table 1).

For all the human models, in the regions where the electrodes were positioned, it was possible to distinguish the grey and white brain matter and the CSF (Figure 1). The dielectric properties of each tissue were assigned based on the literature data at low frequency [36, 37]. Table 1 reports the

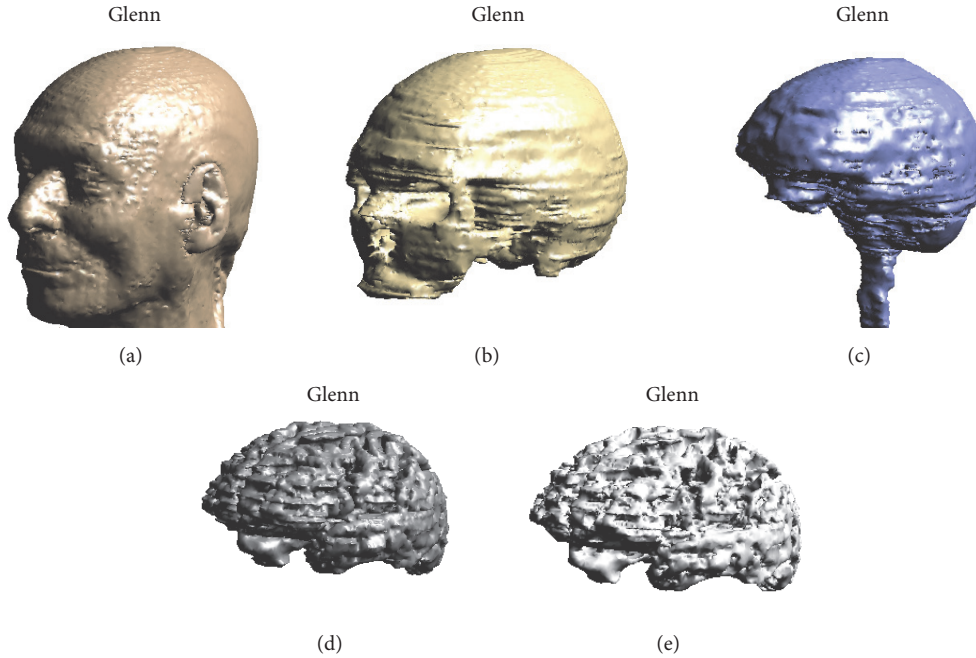


FIGURE 1: 3d rendering of Glenn head model. Tissues shown are (a) skin; (b) skull; (c) CSF; (d) brain grey matter; and (e) brain white matter.

conductivity values of each tissue segmented in the models for each frequency of the stimulation settings used in the study (see Section 2.4 below).

2.2. Electrode Modelling. Since the meninges are not segmented in our anatomical models, our computational model is simulating subdural cortical stimulation.

The geometrical and physical characteristics of the electrodes and their position over the cortex have been modelled based on the clinical literature which uses the MCS for the treatment of neuropathic pain (see, e.g., [7, 9, 10, 32, 33]). Briefly, it consists of a four-electrode array of Medtronic, named, Resume II [31]; each electrode has the following properties, as taken from the technical manual: 4 mm diameter and 1.9 mm height disk made of a platinum-iridium alloy (electrical conductivity: 5.278×10^6 S/m). The lower base of each electrode was positioned in contact with the cortex, whereas the side surface and the upper base are covered by a silicone layer (conductivity: $0.1 * 10^{-9}$ S/m) mimicking the silicone backing that is not modelled, following the approach already used in literature [25]. A 1 cm distance was kept between two neighbouring electrode centres, according to the manufacturer specifications.

The array was centred on the central sulcus alternatively in two different positions corresponding to the cortical somatotopic representation of the upper limb and of the face. More specifically, the electrodes were placed so that the first and the second (numbered 0 and 1 in Figure 2) lie on the motor cortex over the precentral gyrus, and the third and the fourth (numbered 2 and 3) lie on the somatosensory cortex over the postcentral gyrus and in the proximity of postcentral sulcus, respectively (Figure 2).

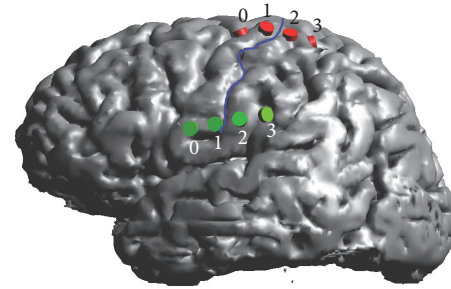


FIGURE 2: Electrode placement on Duke's cortex over the face target region (green) and over the upper limb target region (red). Blue line shows the central sulcus.

2.3. Current Density Numerical Simulations. In this study, a simulation-based approach to calculate the current density distributions within brain tissues was performed through the simulation platform SEMCAD X [38], which implements the Finite Element Method (FEM) in the low frequency range. In detail, it solves the Laplace equation to obtain the electric potential (φ) distribution:

$$\nabla \cdot (\sigma \nabla \varphi) = 0, \quad (1)$$

where σ (S/m) is the electrical conductivity of the human tissues. In the low frequency approximation adopted, ohmic currents dominate displacement currents and capacitive effects are disregarded. The electric field (\mathbf{E}) and then the current density (\mathbf{J}) distributions were obtained by means of the following relations:

$$\begin{aligned} \mathbf{E} &= -\nabla \varphi \\ \mathbf{J} &= \sigma \mathbf{E}. \end{aligned} \quad (2)$$

Implicitly, we assumed the neuronal excitability in the cortex is proportional to the \mathbf{J} (and \mathbf{E}) amplitude and that therefore the regions with a greater current density are more likely stimulated, while the regions with very low current will not directly feel the effects of stimulation [39].

For each simulation, the human head model was inserted in a surrounding bounding box filled with air. The tangential E field component, E_t , was set to be continuous ($E_{t1} = E_{t2}$, which is equivalent to $J_{t1}/\sigma_1 = J_{t2}/\sigma_2$) at the interface between two tissues. Current density was set to be parallel to the face at the interface between skin and air. The upper surface of each of the two active electrodes activated was set to a uniform electrical potential and the potential difference between the two electrodes was adjusted according to the settings listed in the following figure (Figure 3). The computation domain was discretized using a uniform rectilinear mesh with a grid discretization equal to 0.5 mm, which assures resolving the thinnest structures of the model. Relative tolerance for FEM convergence was set to 10^{-12} . To further optimize the quality of the grid and reduce the calculation time, the computational domain was truncated at the brainstem level. Both these choices (mesh step and dimension of the computational domain) were based on a sensitivity analysis showing that neither reducing the mesh step nor increasing the computational domain had a substantial effect on the field values. At the truncation section, we assigned the boundary condition of continuity of the current, whereas the other faces of the bounding box have been treated as insulated, that is, vanishing flux normal to the computational boundary.

2.4. Stimulation Scenarios and Settings. The analysis of the current density distributions was articulated in three distinct phases, corresponding to different scenarios and stimulation settings as summarized in Figure 3.

Phase 1. In Phase 1, we evaluated to which extent the inter-electrode distance affects the current density distributions on both the target regions. A bipolar electrode configuration was set: the cathode was kept fixed on the electrode positioned on the motor cortical representation of the pain region (i.e., electrode 0 in Figure 2), whereas the anode was changed in each simulation from electrodes 1 to 3 of the four-electrodes array (see Figure 2) so that the distance between the two active electrodes varied from 1 cm to 2 cm and 3 cm. This was done for both motor cortex targets, placing the electrode array alternatively on these two regions (i.e., once on the face and once on the upper limb cortical somatotopic representation). The potential difference between the active electrodes was kept fixed at 2 V and the stimulation frequency equal to 40 Hz (in the following these setting parameters will be referred to as “Reference”), as commonly used in chronic MCS therapy for neuropathic pain [5, 32] and the simulation was performed on the 34-year-old model (“Duke”).

Phase 2. In Phase 2, we analysed the effect of both the amplitude and the frequency stimulus for a fixed interelectrode distance of 2 cm. In particular, the potential difference

between cathode (Electrode 0 placed over the precentral gyrus in the motor cortex, Figure 2) and anode (Electrode 2 on postcentral gyrus in the somatosensory cortex, Figure 2) and the frequency of the stimulation signal have been varied in the range described by following literature studies:

- (i) Setting A: taken from [32], who found a significant improvement in the clinical assessment for the evaluation of NP of various origins when the stimulation settings were as follows: amplitude, 2 V; frequency: 40 Hz; and pulsewidth, 60 μ s.
- (ii) Setting B: based on [10], who established the efficacy of electric stimulation on a central poststroke facial pain subject, with the following stimulation parameters: amplitude, 3.65 V; frequency, 50 Hz; and pulsewidth, 120 μ s.
- (iii) Setting C: [7] reported the successful application of bipolar MCS (amplitude: 4.5 V, frequency: 85 Hz, and pulsewidth: 210 μ s) to patients suffering from thalamic neuropathic pain (TNP) and poststroke pain (PSP).
- (iv) Setting D: [9] obtained a positive pain relief in 27 patients affected by chronic neuropathic pain, by increasing both amplitude and frequency and pulsewidth of the delivered pulse up to 5.3 V and 130 Hz and 210 μ s, respectively.

Simulations were run by varying, for each stimulus amplitude (i.e., 2 V, 3.5 V, 4.5 V, and 5.3 V), all the four stimulus frequencies used in the above-mentioned clinical studies (40, 50, 85, and 130 Hz), thus allowing us to consider all the possible combinations of the two parameters. The stimulation signal was considered as a pure sinusoid, following an approach already used in the literature [25, 26]. The pulsewidth was then considered only to verify the stimulation stayed within the safety margins to avoid neuronal damage (see in Section 4 below). Also in this phase, the electrode array was placed over the face motor cortex area of the 34-year-old model (Duke).

Phase 3. The third phase was designed to investigate the age-dependent anatomical differences of the current density distributions generated in the cortex. Bipolar stimulation at the intensity equals 2 V and frequency to 40 Hz was delivered at the electrodes 0 and 2 (interelectrode distance of 2 cm) placed on Duke (34 years old), Louis (14 years old), Glenn (84 years old) on both cortical targets of the face and of the upper limb.

2.5. Data Analysis. The current density distributions were assessed in the cortex and in the white matter. The following parameters were then calculated, according to the study performed by Kim’s group ([25–27, 40, 41]):

- (i) Effective volume (EV_{50}): evaluated for both grey and white matter, it is the volume which has a current density greater than 50% of motor cortex threshold

	Electrode distance (cm)			Delivered current form (setting)*				Model			Cortical target	
	1	2	3	A	B	C	D	Louis	Duke	Glenn	Face	Upper limb
Phase 1	Blue	Blue	Blue	Red	White	White	White	White	Green	White	Grey	Grey
Phase 2	White	Blue	White	Red	Red	Red	Red	White	Green	White	Grey	White
Phase 3	White	Blue	White	Red	White	White	White	Green	Green	Green	Grey	Grey

* Setting A [32]: amplitude 2 V, frequency 40 Hz, pulsewidth 60 μ s

* Setting B [10]: amplitude 3.65 V, frequency 50 Hz, pulsewidth 120 μ s

* Setting C [7]: amplitude 4.5 V, frequency 85 Hz, pulsewidth 210 μ s

* Setting D [9]: amplitude 5.3 V, frequency 130 Hz, pulsewidth 210 μ s

FIGURE 3: Schematic representation of the simulation scenarios and input signal settings used in the three phases.

(MCT) ($J_{MCT} = 2.5 \text{ A/m}^2$ as calculated by [42]). That threshold was chosen as the current density amplitude that can provoke analgesia without motor effects and lies in the range of the practical usage case [27]. This index therefore quantifies the tissue volume that undergoes neural modulation.

- (ii) Effective depth of penetration ($D_{J_{MCT}}$): it is the maximum depth [mm] from the cerebral cortex surface, reached by a current density higher than the 50% of J_{MCT} .

These indexes were analysed as surrogate of the stimulation effectiveness.

3. Results

Figure 4 shows some examples of the current density distributions over the axial slice at 4 cm below the projection of Cz over the cortex (where Cz is referred to according to the 10–20 EEG system) for some phases of the different stimulation settings. The colour maps represent the amplitude distribution of \mathbf{J} and are all clipped above 50% of the J_{MCT} to favour the comparison between the amplitude distributions resulting from the settings used in the three different phases. The green arrows represent the direction of \mathbf{J} , which is preferentially directed tangentially in the crowns of the gyri, whereas it is directed predominantly normally at the bottom of the sulci. In the following, the results will be presented by investigating the two indexes described above, and within each index analysis, by comparing the results of the three phases.

3.1. Effective Volume (EV_{50}). Figure 5 shows the effective volume (in cm^3) calculated varying the stimulation settings according to the three phases (see Section 2.4 above). The bars in the graphs are the sum of the cortex effective volume

(dark colours) and the white matter effective volume (light colours). The total effective volume (EV_{50}) (i.e., the sum of cortex and white matter effective volume) for each simulation setting can be therefore read on the vertical axis. From that figure, one can notice that for a 2 cm interelectrode distance (Phase 1), the total effective volume is significantly higher (up to 30%) than the same quantity calculated for the other two distances and for both the cortical areas. Moreover, one could identify a comparable trend of the EV_{50} along the three distances for both the cortical regions. Similar considerations apply when we consider separately the effective volume trends on the cortex and white matter. Interestingly, the total effective volumes calculated on the facial cortical area are almost double the ones calculated on the upper limb area. This is mainly due to the contribution of the cortex effective volume, whereas the white matter effective volume is higher in the upper limb area. However, for both the electrode placements and for all the distances, the total effective volume stays below 4 cm^3 . This result changes when increasing amplitude and frequency stimulus (Phase 2). In particular, increasing amplitude, the ratio between EV_{50} calculated with an applied potential difference of 3.65 V, 4.5 V, and 5.3 V with respect to EV_{50} calculated at 2 V equals 1.73, 2.10, and 2.46, respectively, independently of the stimulus frequency. Similarly, increasing frequency, the trend of the EV_{50} is the same for each applied potential difference. The ratio between EV_{50} calculated at 50, 85, and 130 Hz with respect to EV_{50} calculated at 40 Hz equals 1.1, 1.25, and 1.3, independently of the applied potential difference and that happens even for both cortex and white matter proportions.

On the contrary, the effective volume variation does not present a clear age-related trend across the three models (Phase 3). The levels, however, for both the targets, decrease in the younger (i.e., Louis) and older (i.e., Glenn) male model with respect to the adult male (i.e., Duke), and hence in this phase the total EV_{50} stays everywhere below 4 cm^3 .

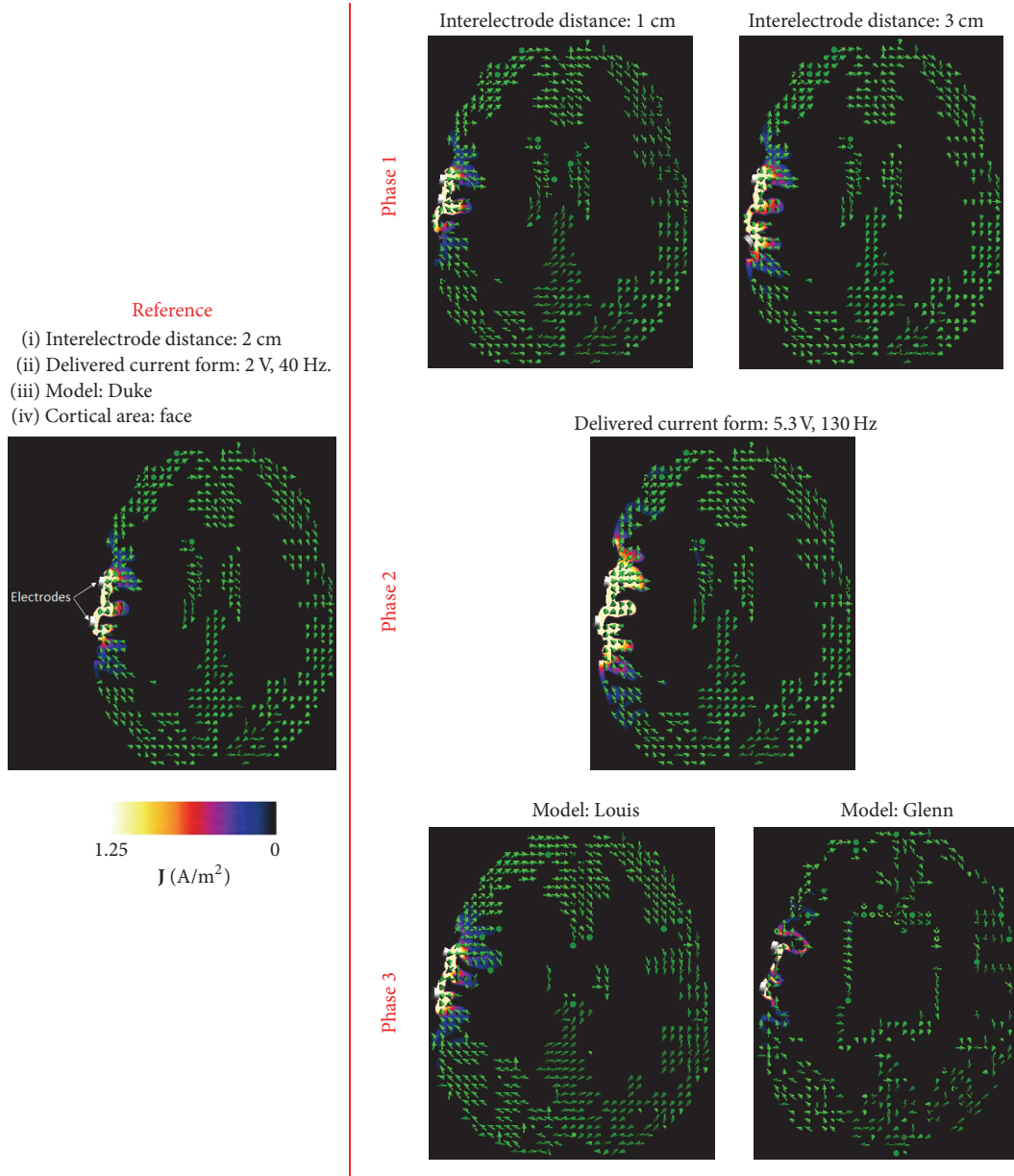


FIGURE 4: Examples of current density (J) distributions over the axial slices at 4 cm below the projection of Cz over the cortex. Colormaps are set between 0 and the 50% of MCT (i.e., 1.25 A/m²); therefore, white areas correspond to the areas in which J is equal or higher to the scale upper limit. Green arrows represent the direction of the current density on the cortex. Panel on the left shows the J distribution produced in the cortex by “Reference” simulation.

3.2. Effective Depth of Penetration (D_{JMCT}). Figure 6 shows the penetration depth (D_{JMCT} in mm) calculated varying stimulation scenarios and settings of the three phases. This analysis was conducted considering the whole brain matter, that is, the cortex and the white matter taken together. By increasing the interelectrode distance (Phase 1), the penetration depth increases with some differences between the two cortical areas: in the face cortical area, the capability to penetrate the cortex ranges from 9.7 to 10.3 mm, whereas in the upper limb from 6.5 to 10.5 mm.

The increase in both amplitude and frequency (Phase 2) results in penetration depth increase, but no clear trend of

those increases can be identified. Moreover, D_{JMCT} calculated on the old male model (Glenn) is reduced in both the cortical regions of about 15–20% with respect to the 34-years-old male model (Phase 3).

4. Discussion and Conclusions

4.1. Motor Threshold Definition. Although MCS for the neuropathic pain treatment is under investigation for more than two decades, the mechanism of action behind its effectiveness is still not clear. Moreover, no guidelines for the best set of stimulation parameters and electrode montages exist so

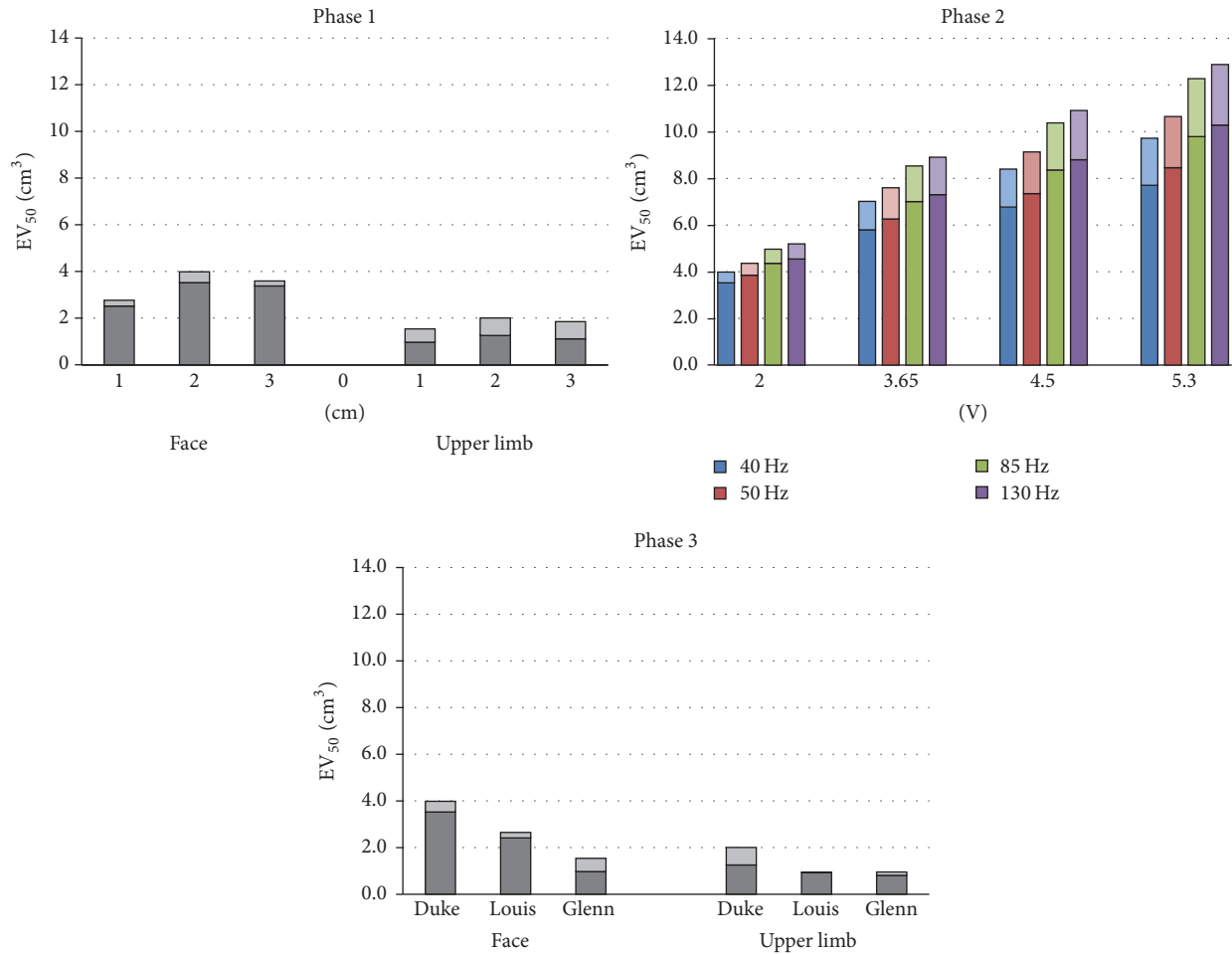


FIGURE 5: Effective volume calculated from the current density distributions by varying the interelectrode distance and positioning (Phase 1), delivered signal settings (Phase 2), and models and positioning (Phase 3). Each bar is the sum of the cortex effective volume (dark) and the white matter effective volume (light).

that all adjustments to them for improving MCS results still depend on iterative empirical testing [24, 43] and are highly individualized.

Lately, different authors [15, 24, 43] have proposed that individual stimulation parameters can be predicted as a percentage of motor threshold activation. A simple way to assess the reliability of this approach can be provided by numerical simulation, actually consistent with experimental data [26].

As discussed in the clinical neurobiology literature [44, 45] the mechanism underlying both the damaging and nondamaging effects of the stimulation are associated with the synchronous activity of a substantially large number of neurons. That supports that the modulation effects are driven by some “mass action” gathered from the simultaneous activation of a critical neuronal volume. Although in our simulations the maximum levels of current density exceed the MCT (see, i.e., white areas in Figure 4), the cortical volume with a current density higher than the MCT is very small and limited to a maximum volume of 1.5 cm³ (across all the stimulation settings and scenarios examined)

distributed mainly under the cathode and the anode. This volume, given that MCS clinical studies that had used the same stimulation parameters did not report side effects [7, 9, 10, 32, 33], is unlikely to induce a neural “mass action” which would lead to an undesired motor response. According to these considerations, in our study we used the 50% of the MCT as a modulation threshold and hence the level that limits the analgesic effect and the efficacy of the technique. However, the goodness of this threshold is an important key factor to be validated in further studies, also in view of the highly individualized actual device settings and the fact that here we modelled the subdural stimulation instead of the epidural stimulation from which stimulus parameters (mainly amplitude and frequency) are taken. One should also note that the MCS threshold was estimated by a transcranial magnetic stimulation (TMS) based study [42]: therefore, given the different J spatial derivative in TMS compared to MCS, it cannot be excluded that neuronal activation in subdural cortical stimulation could be also predicted by different metrics, such as its spatial derivative, as done in previous studies based on the activating function [12, 28, 30,

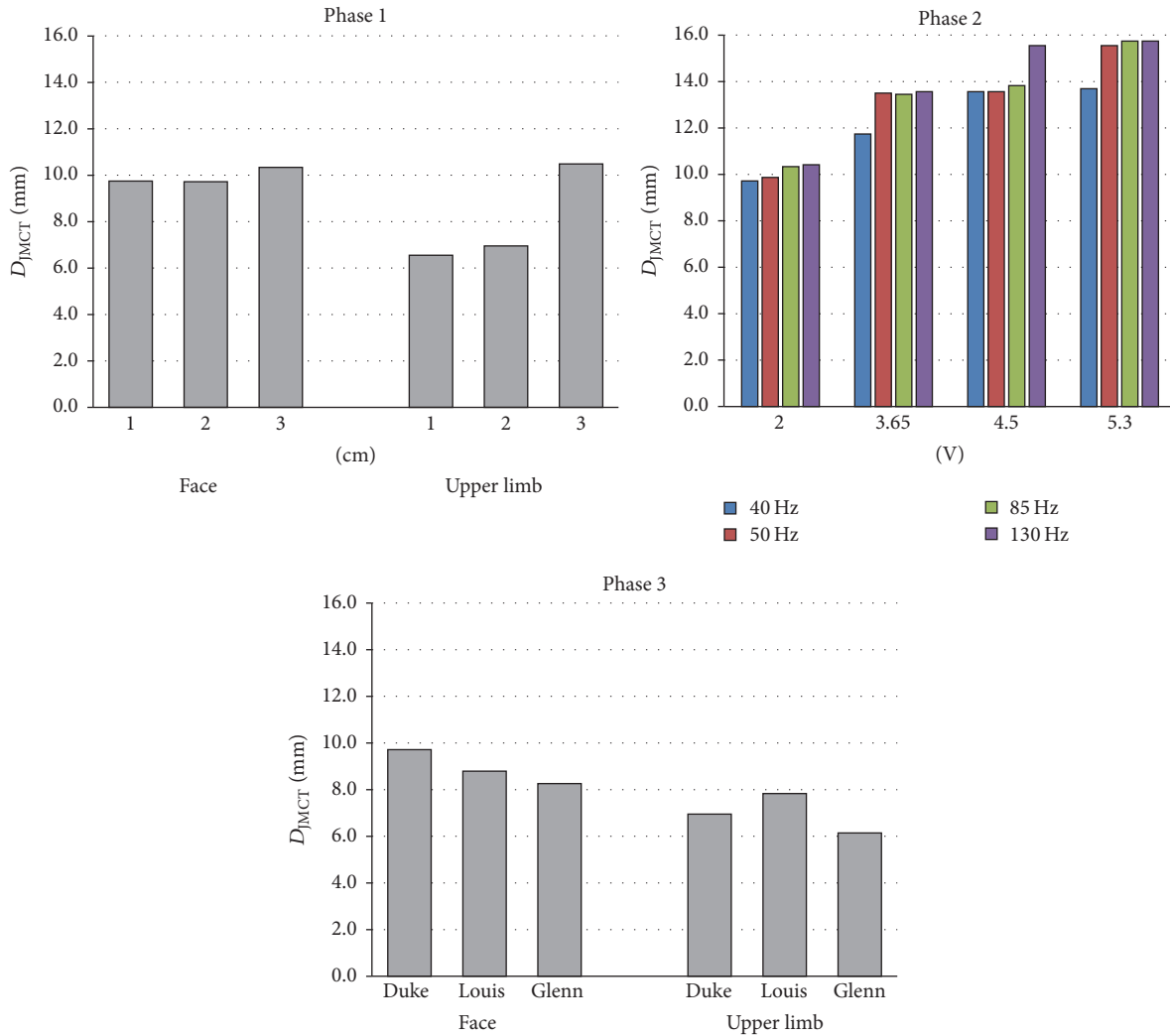


FIGURE 6: Effective depth of penetration calculated from the current density distributions by varying the interelectrode distance and positioning (Phase 1), the delivered signal settings (Phase 2), and the models and positioning (Phase 3).

46]. The authors of [42] numerically calculated the minimum current density peak in the cortex that elicits motor activation from which they estimated the rheobase current and the chronaxie time to determine the strength-duration curve. In the frequency range considered in this study, it slightly varies between 2.49 A/m^2 and 2.62 A/m^2 . This range is in line with the levels for motor cortical activation proposed in the electric stimulation literature, and the 20–50% of that quantity (i.e., $0.5\text{--}1.5 \text{ A/m}^2$) corresponds to the widely accepted range for motor cortex modulation administered through direct current stimulation [30, 47–53].

4.2. Effective Volume Analysis. The first index of efficacy analysed, that is, the effective volume, allows quantifying the percentage of volume of the cerebral cortex and of the white matter that responds to the stimulus. In other words, higher volumes correspond to a broader area stimulated. From Figures 4 and 5, one can notice that, among the three interelectrode distances tested, in both the target areas

and particularly for the facial cortical region, the 2 cm interelectrode distance can stimulate a broader volume. This is probably due to the anatomy of the cerebral cortex that, with its typical convolutions, strongly influences the current density flow, preventing a trivial prediction of its distribution. In an isotropic spherical model, an increasing interelectrode distance linearly raises the values of the volumetric parameters. Conversely, using a realistic anatomical model we show that it happens only as long as the second electrode does not fall in a sulcus of the motor cortex. The central sulcus, which separates the cathode and the anode, prevents indeed that the totality of the area of the cortex between the two electrodes feels a current density sufficient to generate motor cortex neural excitation.

Similarly, the anatomical differences between the different-aged models considerably change both the pattern of stimulation and the indexes examined, with a net contraction of the effective volume in the older men (Figures 5 and 6). That is probably due to the cortical atrophy that

TABLE 2: Schematic representation of the main findings of this study.

	EV_{50} (Figure 5)	D_{MCT} (Figure 6)
Interelectrode distance (Phase 1)	Max @ 2 cm	↑ with distance
Stimulus amplitude (Phase 2)	↑↑ with amplitude	↑ with amplitude
Stimulus frequency (Phase 2)	↑ with frequency	↑ with frequency
Age (Phase 3)	No clear trend with age (less in the elderly)	No clear trend with age (but min in the elderly)

Neuronal response was activated in the volume where $J > 50\%$ MCT (\rightarrow modulation threshold); $\uparrow EV_{50} \rightarrow$ ↑ spread of modulated tissue; $\uparrow D_{MCT} \rightarrow$ ↑ depth of modulated tissue.

usually affects the elderly [51, 52], producing an enlargement of the subarachnoid space (average CSF thickness at the electrodes levels is 0.21 mm, 0.94 mm, and 3.46 mm for Louis, Duke, and Glenn, resp.) and an increase of the CSF volume filling the empty space in the sulci (total CSF volume increases from 214 to 333 and to 619 cm³ in Louis, Duke, and Glenn, resp.). Increasing CSF volume/thickness has a strong impact in epidural cortical stimulation by reducing the amount of current penetrating the cortex and hence reducing the stimulation efficacy, as reported in previous studies [12, 28, 29], but has little effect on the total current entering grey matter in subdural cortical stimulation [41]. However, it is important to consider the CSF volume-related shunting effect when translating the present study's results to epidural motor cortex stimulation.

The thinning of the cortex in Glenn (up to 1.5 mm cortical thickness decrease), visible also in Figure 4, enlarges the space between the convolutions (the sulci) and reduces the spread of the current density in the cerebral cortex in the direction perpendicular to the sulcus, thus increasing the focality of stimulation and hence reducing the effective volume. This is in line with previous modelling studies showing that anatomical differences would highly affect the stimulation efficacy in epidural cortex stimulation [12, 28] and further enforce the need to use anatomical and detailed human models in computational studies addressing current density distribution quantification.

In the case in which it is necessary to stimulate a larger area, our results suggest that the frequency or the amplitude of the stimulus should be increased (Figure 5, Phase 2). The increasing rate of the effective volume scales with the increasing rate of the stimulus amplitude and it agrees with previous calculations performed in two similar studies by Kim's group [27, 41], whereas it is much slower with respect to the increasing rate of the stimulus frequency. Limited effects of frequency could be given by the conductivity variation (Table 1), which however weakly contributes to the electric field distribution variability [54]. However, one should also take into account the fact that increasing frequencies could have other effects on neural activation such as the ones linked to the selective fibers recruitment or to the indirect/synaptic activation of neurons [55].

4.3. Effective Penetration Depth Analysis. The effective volume is strictly linked with the second index examined: the effective penetration depth (Figure 6). As with the previous index, it is greatest in the facial area (Phase 1 and Phase

3). It increases with increasing interelectrode distance, in particular in the upper limb cortical area, when the anode falls into the postcentral gyrus. However, one can notice its limited variability across the different interelectrode distances and across the models. Indeed, this index, which is a sulci-parallel propagation index, is less affected by the elderly cortical atrophy compared to the previous index.

As to the stimulus settings (Figure 6, Phase 2), the effective penetration depth increases very slowly with the frequency increase. While the increase in the frequency can more effectively enlarge the stimulation (Figure 5, Phase 2), it cannot deepen it. The only way to improve that distance of about the 50% within the settings range examined here is to increase the amplitude of the stimulus.

4.4. Relationship between Stimulation Efficacy Related Indexes and Simulation Scenarios/Settings. Table 2 summarizes the main relationships between the indexes and the stimulation scenario and settings analysed.

In terms of absolute values, the indexes of efficacy here evaluated are in good agreement with the values calculated by Kim and colleagues [41] with similar electrode geometry (4 mm versus 5 mm diameter), montage (interelectrode distance of 1 cm, placement over the upper limb area), and stimulation parameters (delivered voltage 2 V at 50 Hz). However, one should take into account the fact that the impact of using typical epidural cortical stimulus settings for a subdural cortical stimulation could not be negligible in terms of both current density values and spatial distribution. As a result of the first remark, the effective volume, the depth of penetration, and the cortical volume above MCT are most likely overestimated here compared to epidural cortical stimulation, thus representing a conservative estimate of side effects related to motor activation in case of epidural cortical stimulation. In addition, moving the electrode from above the dura to directly on the cortex strongly affects also the current density spatial derivative, which in turn impacts on activation of axons (i.e., activating function).

4.5. Stimulation Settings Selection and Safety Related Issues. In the clinical practice, the stimulation settings are chosen based on the available literature and are often modified during the treatment according to the individual response [43]. The need to use, for some patients, increasing frequency and amplitude is indeed probably driven both by the ineffectiveness of the stimulation when the starting settings

are used and by the different patients' motor thresholds. As discussed above, the motor threshold was here kept fixed but the intersubjects physiological variability here examined has to be taken into account when we move from modelling to practice. In the same way, the upper limit of the stimulation settings should assure a sufficient risk margin to prevent the tissue damage. That is indeed the main constraining factor in the choice of stimulation settings for implantable devices used for the treatment of neurological disorders [56]. However, here we verified that the stimulation parameters used in our study stays within the recommended safety margins. Specifically, we evaluated the charge per phase (A·s) and the charge density per phase (measured on the surface of the electrode) (A·s/cm²) for each combination of amplitude and pulsewidth tested and we compared them with the couple limit values reported in the literature [56, 57]. It is believed indeed that both are factors that synergistically determine the stimulation threshold that induces neuronal damage [57]. The results of this analysis (not shown here in detail), indicated, however, that all the possible setting combinations here modelled produce a couple of charge per phase and charge density per phase that guarantees the compliance with the safety limits.

This discussion therefore confirms that our computational study can give important indications about the spatial distribution of the current density during MCS. The use of detailed anatomical models provides indeed a substantial advance in the computational results reliability and have the potential to be included in forward models [58], similar to that used to solve inverse problems in electroencephalography (EEG) analysis, for providing important suggestions about the planning of a more focused stimulation strategy.

Conflicts of Interest

The authors declare that there are no conflicts of interest regarding the publication of this paper.

Acknowledgments

The authors wish to thank Schmid & Partner Engineering AG (<https://www.speag.com>) for having provided the simulation software SEMCAD X/SIM4life. They are also grateful to Dr. Brunella Marzolini for her valuable help and advice.

References

- [1] "International Association for the Study of Pain. IASP Taxonomy," <http://www.iasp-pain.org/Taxonomy?navItemNumber=576#Neuropathicpain>, 2016.
- [2] N. B. Finnerup, S. H. Sindrup, and T. S. Jensen, "The evidence for pharmacological treatment of neuropathic pain," *PAIN*, vol. 150, no. 3, pp. 573–581, 2010.
- [3] S. Tamburin, K. Borg, X. J. Caro et al., "Immunoglobulin G for the Treatment of Chronic Pain: Report of an Expert Workshop," *Pain Medicine*, vol. 15, no. 7, pp. 1072–1082, 2014.
- [4] T. Tsubokawa, Y. Katayama, T. Yamamoto, T. Hirayama, and S. Koyama, "Chronic motor cortex stimulation in patients with thalamic pain," *Journal of Neurosurgery*, vol. 78, no. 3, pp. 393–401, 1993.
- [5] J.-P. Nguyen, J.-P. Lefaucheur, P. Decq et al., "Chronic motor cortex stimulation in the treatment of central and neuropathic pain. Correlations between clinical, electrophysiological and anatomical data," *PAIN*, vol. 82, no. 3, pp. 245–251, 1999.
- [6] D. Carroll, C. Joint, N. Maartens, D. Shlugman, J. Stein, and T. Z. Aziz, "Motor cortex stimulation for chronic neuropathic pain: A preliminary study of 10 cases," *PAIN*, vol. 84, no. 2-3, pp. 431–437, 2000.
- [7] D. Rasche, M. Ruppolt, C. Stippich, A. Unterberg, and V. M. Tronnier, "Motor cortex stimulation for long-term relief of chronic neuropathic pain: a 10 year experience," *PAIN*, vol. 121, no. 1-2, pp. 43–52, 2006.
- [8] D. Fontaine, C. Hamani, and A. Lozano, "Efficacy and safety of motor cortex stimulation for chronic neuropathic pain: Critical review of the literature," *Journal of Neurosurgery*, vol. 110, no. 2, pp. 251–256, 2009.
- [9] W. J. Fagundes-Pereyra, M. J. Teixeira, N. Reyns et al., "Motor cortex electric stimulation for the treatment of neuropathic pain," *Arquivos de Neuro-Psiquiatria*, vol. 68, no. 6, pp. 923–929, 2010.
- [10] A. Balossier, O. Etard, C. Descat, D. Vivien, and E. Emery, "Epidural electrical stimulation to improve chronic poststroke aphasia: A 5-year follow-up," *Brain Stimulation*, vol. 5, no. 3, pp. 364–368, 2012.
- [11] J. A. Brown and N. M. Barbaro, "Motor cortex stimulation for central and neuropathic pain: Current status," *PAIN*, vol. 104, no. 3, pp. 431–435, 2003.
- [12] L. Manola, B. H. Roelofsen, J. Holsheimer, E. Marani, and J. Geelen, "Modelling motor cortex stimulation for chronic pain control: Electrical potential field, activating functions and responses of simple nerve fibre models," *Medical & Biological Engineering & Computing*, vol. 43, no. 3, pp. 335–343, 2005.
- [13] J. P. Nguyen, J. P. Lefaucher, C. Le Guerin et al., "Motor cortex stimulation in the treatment of central and neuropathic pain," *Archives of Medical Research*, vol. 31, no. 3, pp. 263–265, 2000.
- [14] T. Tsubokawa, Y. Katayama, T. Yamamoto, T. Hirayama, and S. Koyama, "Treatment of thalamic pain by chronic motor cortex stimulation," *Pacing and Clinical Electrophysiology*, vol. 14, no. 1, pp. 131–134, 1991.
- [15] G. Monsalve, "Motor cortex stimulation for facial chronic neuropathic pain: A review of the literature," *Surgical Neurology International*, vol. 3, no. 5, pp. S290–S311, 2012.
- [16] J. M. Henderson and S. P. Lad, "Motor cortex stimulation and neuropathic facial pain," *Neurosurg Focus*, vol. 21, no. 6, p. E6, 2006.
- [17] J. M. Lucas, Y. Ji, and R. Masri, "Motor cortex stimulation reduces hyperalgesia in an animal model of central pain," *Pain*, vol. 152, no. 6, pp. 1398–1407, 2011.
- [18] Y. Lazorthes, J. C. Sol, S. Fowo, F. E. Roux, and J. C. Verdié, "Motor cortex stimulation for neuropathic pain," in *Operative Neuromodulation. Acta Neurochirurgica Supplements*, D. E. Sakas and B. A. Simpson, Eds., vol. 97/2, Springer, Vienna, 2007.
- [19] X. Drouot, J.-P. Nguyen, M. Peschanski, and J.-P. Lefaucheur, "The antalgic efficacy of chronic motor cortex stimulation is related to sensory changes in the painful zone," *Brain*, vol. 125, no. 7, pp. 1660–1664, 2002.
- [20] J. P. Brasil-Neto, "Motor cortex stimulation for pain relief: Do corollary discharges play a role?" *Frontiers in Human Neuroscience*, vol. 10, no. 323, 2016.

- [21] S. Zaghi, N. Heine, and F. Fregni, "Brain stimulation for the treatment of pain: A review of costs, clinical effects, and mechanisms of treatment for three different central neuromodulatory approaches," *Journal of Pain Management*, vol. 2, no. 3, pp. 339–352, 2009.
- [22] J. M. Hoogendam, G. M. Ramakers, and V. Di Lazzaro, "Physiology of repetitive transcranial magnetic stimulation of the human brain," *Brain Stimulation*, vol. 3, no. 2, pp. 95–118, 2010.
- [23] R. Melzack, "Pain and the neuromatrix in the brain," *Journal of Dental Education*, vol. 65, no. 12, pp. 1378–1382, 2001.
- [24] P. J. Slotty, S. Chang, and C. R. Honey, "Motor threshold: a possible guide to optimizing stimulation parameters for motor cortex stimulation," *Neuromodulation*, vol. 18, pp. 566–571, 2015.
- [25] D. Kim et al., "Computational study on subdural cortical stimulation - the influence of the head geometry, anisotropic conductivity, and electrode configuration," *PLoS One*, vol. 17, Article ID e108028, p. 9, 2014.
- [26] D. Kim, J. Jeong, S. Jeong, S. Kim, S. C. Jun, and E. Chung, "Validation of Computational Studies for Electrical Brain Stimulation With Phantom Head Experiments," *Brain Stimulation*, vol. 8, no. 5, pp. 914–925, 2015.
- [27] H. Seo, D. Kim, and S. C. Jun, "Effect of anatomically realistic full-head model on activation of cortical neurons in subdural cortical stimulation – a computational study," *Scientific Reports*, vol. 6, Article ID 27353, pp. 1892–1895, 2016.
- [28] A. Wongsarnpigoon and W. M. Grill, "Computational modeling of epidural cortical stimulation," *Journal of Neural Engineering*, vol. 5, no. 4, pp. 443–454, 2008.
- [29] A. Wongsarnpigoon and W. M. Grill, "Computer-based model of epidural motor cortex stimulation: Effects of electrode position and geometry on activation of cortical neurons," *Clinical Neurophysiology*, vol. 123, no. 1, pp. 160–172, 2012.
- [30] L. Manola, J. Holsheimer, P. Veltink, and J. R. Buitenweg, "Anodal vs cathodal stimulation of motor cortex: A modeling study," *Clinical Neurophysiology*, vol. 118, no. 2, pp. 464–474, 2007.
- [31] ResumeTM, Medtronic, Inc., Minneapolis, Minnesota, USA – Technical Manual, <https://www.fda.gov.tw/MLMS/ShowFile.aspx?LicId=06009114&Seq=001&Type=9>.
- [32] J. P. Lefaucheur et al., "Motor cortex stimulation for the treatment of refractory peripheral neuropathic pain," *Brain*, vol. 132, pp. 1463–1471, 2009.
- [33] J. P. Nguyen et al., "Treatment of chronic neuropathic pain by motor cortex stimulation: results of a bicentric controlled crossover trial," *Brain stimulation*, vol. 1, pp. 89–96, 2008.
- [34] A. Christ, W. Kainz, E. G. Hahn et al., "The Virtual Family—development of surface-based anatomical models of two adults and two children for dosimetric simulations," *Physics in Medicine and Biology*, vol. 55, no. 2, pp. N23–N38, 2010.
- [35] M. C. Gosselin et al., "Development of a new generation of high-resolution anatomical models for medical device evaluation: the Virtual Population 3.0," *Physics in Medicine and Biology*, vol. 59, pp. 5287–5303, 2014.
- [36] S. Gabriel, R. W. Lau, and C. Gabriel, "The dielectric properties of biological tissues: II. Measurements in the frequency range 10 Hz to 20 GHz," *Physics in Medicine and Biology*, vol. 41, no. 11, pp. 2251–2269, 1996.
- [37] C. Gabriel, A. Peyman, and E. H. Grant, "Electrical conductivity of tissue at frequencies below 1 MHz," *Physics in Medicine and Biology*, vol. 54, no. 16, pp. 4863–4878, 2009.
- [38] SEMCAD X v14.8 by SPEAG, Schmid & Partner Engineering, AG, Zurich, Switzerland, www.speag.com.
- [39] M. Bikson and A. Datta, "Guidelines for precise and accurate computational models of tDCS," *Brain Stimulation*, vol. 5, no. 3, pp. 430–431, 2012.
- [40] D. Kim, S. C. Jun, and H. I. Kim, "Computational study of subdural and epidural cortical stimulation of the motor cortex," in *Proceedings of the 2011 Annual International Conference of the IEEE Engineering in Medicine and Biology Society*, pp. 7226–7229, Boston, MA, USA, 2011.
- [41] D. Kim, H. Seo, H.-I. Kim, and S. C. Jun, "The computational study of subdural cortical stimulation: a quantitative analysis of voltage and current stimulation," in *Proceedings of the 34th Annual International Conference of the IEEE Engineering in Medicine and Biology Society (EMBC)*, pp. 867–870, San Diego, Calif, USA, 2012.
- [42] T. Kowalski, J. Silny, and H. Buchner, "Current Density Threshold for the Stimulation of Neurons in the Motor Cortex Area," *Bioelectromagnetics*, vol. 23, no. 6, pp. 421–428, 2002.
- [43] C. Nuti, R. Peyron, L. Garcia-Larrea et al., "Motor cortex stimulation for refractory neuropathic pain: four year outcome and predictors of efficacy," *Pain*, vol. 118, no. 1-2, pp. 43–52, 2005.
- [44] W. F. Agnew, T. G. H. Yuen, D. B. McCreery, and L. A. Bullara, "Histopathologic evaluation of prolonged intracortical electrical stimulation," *Experimental Neurology*, vol. 92, no. 1, pp. 162–185, 1986.
- [45] A. M. Lozano and M. Hallett, "Handbook of clinical neurology," *Brain Stimulation*, vol. 116, pp. 9–10, 2013.
- [46] F. Rattay, "Analysis of Models for Extracellular Fiber Stimulation," *IEEE Transactions on Biomedical Engineering*, vol. 36, no. 7, pp. 676–682, 1989.
- [47] J. G. R. Jefferys, "Nonsynaptic modulation of neuronal activity in the brain: Electric currents and extracellular ions," *Physiological Reviews*, vol. 75, no. 4, pp. 689–723, 1995.
- [48] P. C. Miranda, A. Mekonnen, R. Salvador, and G. Ruffini, "The electric field in the cortex during transcranial current stimulation," *NeuroImage*, vol. 70, pp. 48–58, 2013.
- [49] P. C. Miranda, M. Lomarev, and M. Hallett, "Modeling the current distribution during transcranial direct current stimulation," *Clinical Neurophysiology*, vol. 117, no. 7, pp. 1623–1629, 2006.
- [50] A. R. Brunoni, M. A. Nitsche, and N. Bolognini, "Clinical research with transcranial direct current stimulation (tDCS): challenges and future directions," *Brain Stimulation*, vol. 5, no. 3, pp. 175–195, 2012.
- [51] S. Fiocchi, "Assessment of the Electric Field induced by deep Transcranial Magnetic Stimulation in the elderly using H-coil," *ACES Journal*, vol. 31, pp. 636–643, 2016.
- [52] Z. Nahas et al., "Safety and benefits of distance-adjusted prefrontal transcranial magnetic stimulation in depressed patients 55-75 years of age: a pilot study," *Depress Anxiety*, vol. 19, pp. 249–256, 2004.
- [53] M. A. Nitsche, L. G. Cohen, E. M. Wassermann et al., "Transcranial direct current stimulation: State of the art 2008," *Brain Stimulation*, vol. 1, no. 3, pp. 206–223, 2008.
- [54] S. Fiocchi, E. Chiamello, M. Parazzini, P. Ravazzani, and R. M. Lafrenie, "Influence of tissue conductivity on foetal exposure to extremely low frequency magnetic fields at 50 Hz using stochastic dosimetry," *PLoS ONE*, vol. 13, no. 2, Article ID e0192131, 2018.

- [55] C. McIntyre and W. Grill, "Extracellular stimulation of central neurons: Influence of stimulus waveform and frequency on neuronal output," *Journal of Neurophysiology*, vol. 88, no. 4, pp. 1592–1604, 2002.
- [56] S. F. Cogan, K. A. Ludwig, C. G. Welle, and P. Takmakov, "Tissue damage thresholds during therapeutic electrical stimulation," *Journal of Neural Engineering*, vol. 13, no. 2, Article ID 021001, 2016.
- [57] D. B. McCreery, W. F. Agnew, T. G. H. Yuen, and L. Bullara, "Charge density and charge per phase as cofactors in neural injury induced by electrical stimulation," *IEEE Transactions on Biomedical Engineering*, vol. 37, no. 10, pp. 996–1001, 1990.
- [58] J. P. Dmochowski, A. Datta, M. Bikson, Y. Su, and L. C. Parra, "Optimized multi-electrode stimulation increases focality and intensity at target," *Journal of Neural Engineering*, vol. 8, no. 4, Article ID 046011, 2011.

Research Article

Transfer Kernel Common Spatial Patterns for Motor Imagery Brain-Computer Interface Classification

Mengxi Dai,^{1,2} Dezhi Zheng ,^{1,2} Shucong Liu,^{1,2} and Pengju Zhang^{1,2}

¹Beijing Advanced Innovation Center for Big Data-Based Precision Medicine, Beihang University, Beijing 100191, China

²Key Laboratory of Precision Opto-Mechatronics Technology, Ministry of Education, School of Instrumentation Science and Opto-Electronics Engineering, Beihang University, Beijing 100191, China

Correspondence should be addressed to Dezhi Zheng; zhengdezhi@buaa.edu.cn

Received 15 November 2017; Revised 2 February 2018; Accepted 12 February 2018; Published 18 March 2018

Academic Editor: Marta Parazzini

Copyright © 2018 Mengxi Dai et al. This is an open access article distributed under the Creative Commons Attribution License, which permits unrestricted use, distribution, and reproduction in any medium, provided the original work is properly cited.

Motor-imagery-based brain-computer interfaces (BCIs) commonly use the common spatial pattern (CSP) as preprocessing step before classification. The CSP method is a supervised algorithm. Therefore a lot of time-consuming training data is needed to build the model. To address this issue, one promising approach is transfer learning, which generalizes a learning model can extract discriminative information from other subjects for target classification task. To this end, we propose a transfer kernel CSP (TKCSP) approach to learn a domain-invariant kernel by directly matching distributions of source subjects and target subjects. The dataset IVa of BCI Competition III is used to demonstrate the validity by our proposed methods. In the experiment, we compare the classification performance of the TKCSP against CSP, CSP for subject-to-subject transfer (CSP SJ-to-SJ), regularizing CSP (RCSP), stationary subspace CSP (ssCSP), multitask CSP (mtCSP), and the combined mtCSP and ssCSP (ss + mtCSP) method. The results indicate that the superior mean classification performance of TKCSP can achieve 81.14%, especially in case of source subjects with fewer number of training samples. Comprehensive experimental evidence on the dataset verifies the effectiveness and efficiency of the proposed TKCSP approach over several state-of-the-art methods.

1. Introduction

The brain-computer interface (BCI) offers a new pathway of communication between an external device and the brain through transforming metabolic or electrophysiological brain activities to control messages for devices and applications. The electroencephalogram (EEG) obtains time series data with multiple variants recorded at several sensors pressed on the scalp. It thereby presents electrical potentials under the induction of brain activities. These are used by noninvasive BCI systems to convert the mind or intention of a subject into a control message for certain device, such as a computer, a neuroprosthesis, or a wheelchair [1–4].

Currently, classification performance promotion of BCI systems based on the EEG has significant challenges. For one, it is necessary for a fresh subject to conduct a lengthy calibration session for sufficient training sample collection to establish classifiers and extractors of subject-specific features. The test session later employs the classifiers and extractors

to classify the subjects brain signals. In a recent study on BCIs, it was shown to be very important to reduce training sessions on account of the time-consuming, tedious process of a calibration session. As a result, conducting a performance promotion using a scarce labeled set is more desirable compared with using a large one. Nevertheless, suitable methods must be identified to strengthen the performance. This is because a short calibration session means the availability of merely a few training samples for target users, which may result in overfitting or suboptimal feature classifiers or extractors.

To address the above problem, transfer learning is a promising approach [5, 6]. It applies data represented in various feature spaces or obtained from various distributions for compensating the insufficient labeled data. In the BCI field, transfer learning has attracted considerable attention because it enables the establishing of subject-independent spatial classifiers and/or filters, and it lowers calibration times. Some studies concentrated on feature representation

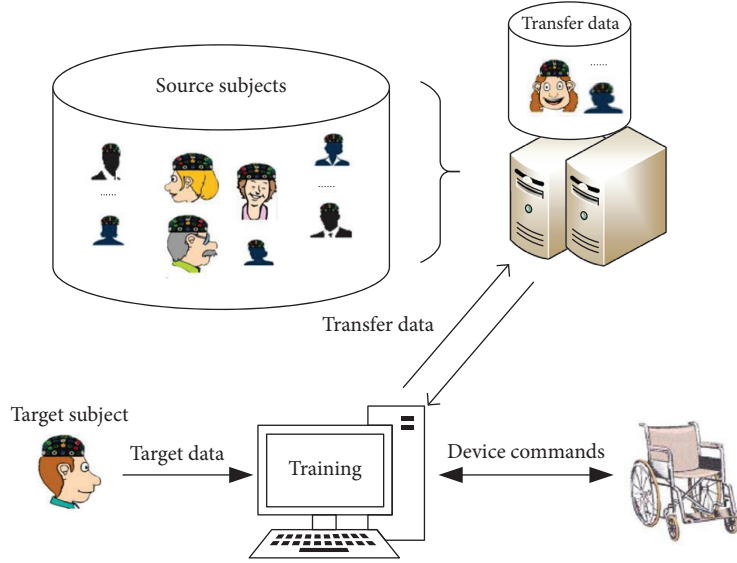


FIGURE 1: An illustration of subject transfer based BCI system.

transfer methods in EEG classification [7–11]. In this situation, we encode the knowledge that traverses domains into a fresh feature representation. Accordingly, precise classification performance is thereby expected in settings with a small sample.

A proposed schedule for practical applications of BCI systems based on subject transfer is presented in Figure 1 [12]. The datasets provided by the source subjects can be stored as a dataset group. Next, the BCI device can first acquire transfer data from the source subject groups when it is prepared to execute classification for the user. In this paper, we thus propose the transfer kernel common spatial patterns (TKCSP) method. The TKCSP computation is formulated by BCI as an optimization problem with multiple subjects, thereby incorporating data from other subjects to establish a common feature space.

2. Transfer Kernel Common Spatial Patterns

This section mentioned a new feature extraction method, TKCSP, which combines two previous approaches, kernel common spatial patterns (KCSP) [13] and transfer kernel learning (TKL) [6]. KCSP is an extraction approach for motor imagery, and TKL is a promising transfer learning method. In Sections 2.1 and 2.2, we describe the KCSP algorithm and the TKL algorithm, respectively. In Section 2.3, we would propose the TKCSP algorithm in combination with the above two algorithms.

2.1. Kernel Common Spatial Patterns. The KCSP algorithm based on CSP is used to find the components with the largest energy difference between the two experimental conditions [13–15]. Its basic idea is to find the optimal spatial filter to maximize the component energy under two sets of experimental conditions after the spatial filtering.

The first step is to calculate the covariance between the two signals. Consider E_i as an $M \times T$ matrix representing the

i th trial of EEG signals, wherein M represents the channel amount and T represents the points of time. The class-specific spatial covariance matrix can hence be acquired by the steps below.

$$R_i = \frac{K(E_i E_i^T)}{\text{trace}(K(E_i E_i^T))}, \quad (1)$$

where i represents the class label, $K(E_i E_i^T) = \langle \varphi(E_i), \varphi(E_i) \rangle$ represents the kernel function, and $\langle \cdot \rangle$ denotes the inner product. Thus we can replace the computation of the aggregate spatial covariance matrix with $R_c = R_1 + R_2$.

Additionally, we can factor R_c to be $R_c = U_0 \Lambda_c U_0^T$, where $U_0 \in \mathbf{R}^{n \times n}$ represents a matrix with eigenvectors in a row, while Λ_c represents the diagonal matrix of eigenvalues classified in declining order.

The variances can be equalized by using a whitening transmission P within space that the eigenvectors span in U_0 such that P equals

$$P = \lambda^{1/2} U_0^T. \quad (2)$$

Thirdly, the whitening matrix P can be used to transform R_1 and R_2 into S_1 and S_2 as

$$\begin{aligned} S_1 &= P R_1 P^T, \\ S_2 &= P R_2 P^T. \end{aligned} \quad (3)$$

S_1 and S_2 have the same eigenvectors, that is, if

$$\begin{aligned} S_1 &= B \lambda_1 B^T, \\ S_2 &= B \lambda_2 B^T, \\ \lambda_1 + \lambda_2 &= I, \end{aligned} \quad (4)$$

where I represents the identity matrix. At this point, the sum is always one for these two corresponding eigenvalues. Hence,

Input: Data E .
Output: Common spatial patterns W^{-1} ,
and common spatial filters W .

- (1) Compute spatial covariance matrix R_i , $i = 1, 2$ by (1)
and the total spatial covariance matrix is $R_c = R_1 + R_2$.
- (2) Eigen decomposition $R_c = U_c \Lambda_c U_c^T$;
whitening transformation $P = \lambda^{1/2} U_c^T$.
- (3) Transform covariance matrices $S_1 = PR_1 P^T$, $S_2 = PR_2 P^T$.
and eigen decomposition $S_1 = B\lambda_1 B^T$, $S_2 = B\lambda_2 B^T$.
- (4) Construct the spatial filter $W = (B^T P)^T$.

ALGORITHM 1: Kernel common spatial pattern algorithms.

the eigenvectors having the smallest eigenvalues for S_1 have the largest eigenvalues for S_2 and vice versa. This property enables eigenvector B to sort these two classes.

Finally, owing to $W = (B^T P)^T$ as the common spatial filters, the common spatial patterns are columns of W^{-1} , which can be regarded as the source distribution vectors for time-invariant EEG. Algorithm 1 shows the summary of a complete KCSP procedure.

2.2. Transfer Kernel Learning. TKL can directly match the source distribution and target distribution to learn a domain-invariant kernel space, using the knowledge of the source domain to help complete the learning tasks in the target domain. This section begins with definitions of terminology used, and Notations section presents a summary of commonly used notations.

Definition 1. A domain D includes a d -dimensional feature space \mathcal{F} as well as a marginal probability distribution $P(x)$; that is, $\mathcal{D} = \{\mathcal{F}, P(x)\}$, $x \in \mathcal{F}$.

In general, if two domains Z and X have different marginal distributions or feature spaces, they will have difference; that is, $\mathcal{F}_Z \neq \mathcal{F}_X \vee P(z) \neq P(x)$.

Definition 2. Given domain \mathcal{D} , a classifier $f(x)$ and a cardinality label set \mathcal{Y} compose a task \mathcal{T} ; that is, $\mathcal{T} = \{\mathcal{Y}, f(x)\}$, in which $y \in \mathcal{Y}$, and the interpretation of $f(x) = P(y | x)$ can be conditioned probability distribution.

In general, if two tasks \mathcal{T}_Z and \mathcal{T}_X have different conditioned distributions or label spaces, they will have a difference; that is, $\mathcal{Y}_Z \neq \mathcal{Y}_X \vee P(y | z) \neq P(y | x)$.

Problem 3 (transfer kernel learning). Given an unlabeled target domain $X = \{x_1, \dots, x_n\}$ and a labeled source domain $Z = \{(z_1, y_1), \dots, (z_m, y_m)\}$ with $\mathcal{F}_Z = \mathcal{F}_X$, $\mathcal{Y}_Z = \mathcal{Y}_X$, $P(z) \neq P(x)$, and $P(y | z) \neq P(y | x)$, a kernel $k(z, x) = \langle \phi(z), \phi(x) \rangle$ with an invariable domain is learned so that $P(\phi(z)) \approx P(\phi(x))$. Suppose $P(y | \phi(z)) \approx P(y | \phi(x))$, then a kernel machine targeting Z can effectively generalize X .

Firstly, calculate the target kernel function, the source kernel function, and the cross-kernel function. Assume an

input kernel function k is given to us, for example, Laplacian kernel $k(z, x) = e^{\gamma|z-x|}$ or Gaussian kernel $k(z, x) = e^{\gamma\|z-x\|^2}$, then the target kernel K_X , the source kernel K_Z , and the cross-domain kernel K_{ZX} can be computed. A domain-invariant kernel \bar{K}_{ZUX} can be learned by utilizing these three kernels. Under this challenging situation, the sufficient matching of marginal distributions plays an indispensable role in efficient learning of the domain transfer.

To require two datasets (for example, target data X and source data Z) to conform to similar distributions of the feature space, that is, $P(\phi(z)) \approx P(\phi(x))$, requiring them to have similar kernel matrices is sufficient, that is, $K_Z \approx K_X$ [16]. Nevertheless, kernel matrices depend on data and the direct evaluation of closeness between varied kernels is improbable because of the varying dimensions; that is, $K_Z \in R^{m \times m}$, $K_X \in R^{n \times n}$ [17]. To solve this issue, the Nyström kernel approximation idea is adopted for the generation of an extrapolated source kernel $\bar{K}_Z \in R^{m \times m}$ by an eigensystem of target kernel K_X . Next, \bar{K}_Z can arise to kernel K_Z as the ground truth source and can be comparable to a spectral kernel design. Figure 2 shows the whole learning procedure.

Secondly, Nyström kernel approximation is adopted to execute eigensystem extrapolation [16]. To this end, standard eigendecomposition is adopted on the target kernel K_X

$$K_X \Phi_X = \Phi_X \Lambda_X, \quad (5)$$

which provides the eigensystem $\{\Lambda_X, \Phi_X\}$ of target kernel K_X .

Thirdly, we assess the eigensystem on source data Z by utilizing the Nyström approximation theorem. The derivation of the eigenvectors $\bar{\Phi}_Z$ for extrapolated source kernel \bar{K}_Z is

$$\bar{\Phi}_Z \approx K_{ZX} \Phi_X \Lambda_X^{-1}, \quad (6)$$

where $K_{ZX} \in R^{m \times n}$ is the cross-domain kernel matrix between Z and X , assessed by kernel function k .

The initial Nyström method directly utilizes target eigenvalues Λ_X and extrapolated source eigenvectors $\bar{\Phi}_Z$ to make approximation for the source kernel K_Z . In essence, the distribution difference across domains is embodied by the Nyström approximation error; that is, error is close to 0 if and only if $P(z) \approx P(x)$. An invariant kernel extrapolated to varied domains will be achieved if an extrapolated kernel

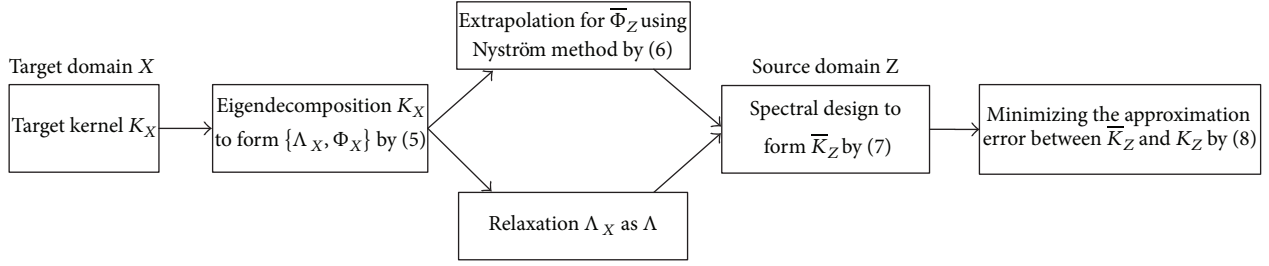


FIGURE 2: Complete procedure of transfer kernel learning.

can be found for realizing a minimized Nyström approximation error, thereby facilitating a more efficient cross-domain generalization.

The spectral kernel design idea is adopted to establish a new kernel matrix from extrapolated eigensystem to reduce the Nyström approximation error [18]. The key construction of target kernel K_X can thus be preserved by the kernel matrix generated via extrapolated eigensystem Φ_Z ; however, the flexibility of the reshaping could be retained to keep the distribution difference minimized.

Fourthly, eigenspectrum Λ_X can be relaxed in the primary Nyström approach to be parameters Λ that can be learned resulting in a kernel family extrapolated from the target eigensystem yet assessed on the source data. The extrapolated source kernel \bar{K}_Z is obtained as follows:

$$\bar{K}_Z = \bar{\Phi}_Z \Lambda \bar{\Phi}_Z^T. \quad (7)$$

The critical structures of the target domain can be preserved by this kernel family, that is, eigenvectors $\bar{\Phi}_Z$. Moreover, the free eigenspectrum Λ remains undetermined. Unlike a conventional spectral kernel design that learns the parameters through Λ trained on the spectral kernel towards a previous kernel calculated in the same domain, kernel matching can be performed across domains.

Fifthly, we strive to minimize the approximation error between the ground truth source kernel K_Z and the extrapolated source kernel \bar{K}_Z for explicitly minimizing the distribution difference herein by utilizing the squared loss

$$\begin{aligned} \min_{\Lambda} \quad & \|\bar{K}_Z - K_Z\|_{\mathcal{F}}^2 = \|\bar{\Phi}_Z \Lambda \bar{\Phi}_Z^T - K_Z\|_{\mathcal{F}}^2 \\ & \lambda_i \geq \zeta \lambda_{i+1}, \quad i = 1, \dots, n-1 \\ & \lambda_i \geq 0, \quad i = 1, \dots, n, \end{aligned} \quad (8)$$

where $\Lambda = \text{diag}(\lambda_1, \dots, \lambda_n)$ belongs to the n nonnegative eigenspectrum parameters, while $\zeta \geq 1$ belongs to the eigenspectrum damping factor [19].

The marginal distributions of multiple source domains can be matched with the target domain using the generalized transfer kernel learning (TKL) approach. This approach can be conducted by the source-specific eigenspectrum Λ learning for every source domain separately in the initial place. Secondly, existing learning algorithms of multiple sources are used to implement consensus forecasting for the target

domain on the basis of predicting multiple source domains [20, 21].

Sixthly, the standard quadratic programming possessing (QP) linear constraints are used herein to show the solution of the TKL optimization problem (8). Here, n eigenspectrum parameter is denoted as $\lambda = (\lambda_1, \dots, \lambda_n)$; that is, $\Lambda = \text{diag}(\lambda)$. Equation (8) is reformulated in the matrix form by linear algebra

$$\begin{aligned} \min_{\lambda} \quad & \lambda^T Q \lambda - 2\gamma^T \lambda \\ & C \lambda \geq 0 \\ & \lambda \geq 0. \end{aligned} \quad (9)$$

The following are the respective definitions of QP coefficient matrices Q , γ and constraint matrix

$$\begin{aligned} Q &= (\Phi_Z^T \Phi_Z) \odot (\Phi_Z^T \Phi_Z) \\ \gamma &= \text{diag}(\Phi_Z^T K_Z \Phi_Z) \\ C &= I - \zeta \bar{I}, \end{aligned} \quad (10)$$

where $\zeta \geq 1$ represents the eigenspectrum damping factor, which is also the only tunable parameter within TKL. Additionally, $I \in \mathbf{R}^{n \times n}$ denotes the identity matrix, and $\bar{I} \in \mathbf{R}^{n \times n}$ represents the first diagonal matrix with the nonvanishing elements.

Finally, constructing the domain-invariant kernel \bar{K}_A on the target and source data $A = Z \cup X$ is straightforward with the learned optimal eigenspectrum parameters Λ . According to spectral kernel design, we can generate \bar{K}_A from the eigensystem $\{\Lambda, \bar{\Phi}_A\}$ invariant to domain

$$\bar{K}_A = \begin{bmatrix} \bar{\Phi}_Z \Lambda \bar{\Phi}_Z^T & \bar{\Phi}_Z \Lambda \bar{\Phi}_X^T \\ \bar{\Phi}_X \Lambda \bar{\Phi}_Z^T & \bar{\Phi}_X \Lambda \bar{\Phi}_X^T \end{bmatrix} = \bar{\Phi}_A \Lambda \bar{\Phi}_A^T, \quad (11)$$

where $\bar{\Phi}_A \triangleq [\bar{\Phi}_Z; \bar{\Phi}_X]$ belongs to extrapolated eigenvectors on all data A . We can directly feed the kernel \bar{K}_A invariant to the domain to normal kernel machines, for example, KCSF, for facilitating the cross-domain generalization and prediction. Algorithm 2 shows the summary of a complete procedure.

Input: Data X ; kernel k ; eigen-damping factor ζ .
Output: Domain-invariant kernel \bar{K}_A .

- (1) Compute the target kernel function K_X , the source kernel function K_Z , and cross-domain kernel function K_{ZX} by kernel k .
- (2) Eigendecompose the target kernel function K_X for the eigensystem $\{\Lambda_X, \Phi_X\}$ by (5).
- (3) Extrapolate for source eigenvector $\bar{\Phi}_Z$ via Nyström approximation by (6).
- (4) Generate the extrapolated source kernel \bar{K}_Z by (7)
- (5) Minimize the approximation error between the ground truth source kernel K_Z and the extrapolated source kernel \bar{K}_Z by (8).
- (6) Solve QP problem (9) for eigenspectrum λ .
- (7) Construct domain-invariant kernel \bar{K}_A by (11).

ALGORITHM 2: TKL algorithm.

Input: Data E_X, E_Z .
Output: Common Spatial Patterns W^{-1} .

- (1) Compute transfer kernel \bar{K}_A by Algorithm 2.
- (2) Compute spatial covariance matrix $R_i = \bar{K}_A / \text{trace}(\bar{K}_A)$, $i = 1, 2$.
And the total spatial covariance matrix is $R_c = R_1 + R_2$.
- (3) Eigen decomposition $R_c = U_c \Lambda_c U_c^T$;
whitening transformation $P = \lambda^{1/2} U_0^T$.
- (4) Transform covariance matrices $S_1 = P R_1 P^T$, $S_2 = P R_2 P^T$
and eigen decomposition $S_1 = B \lambda_1 B^T$, $S_2 = B \lambda_2 B^T$.
- (5) Construct the spatial filter $W = (B^T P)^T$.

ALGORITHM 3: Transfer kernel common spatial pattern algorithm.

2.3. Transfer Kernel CSP. When transfer kernel \bar{K}_A replaces kernel $K(E_i E_i^T)$ in (1), we can build the TKCSP. For all methods based on the kernel, linear kernel is adopted by us; that is, $K(x_i, x_j) = x_i^T x_j$. Then $R_i = K_A / \text{trace}(K_A)$ can be used to estimate the spatial covariance. Algorithm 3 presents a summary of a complete TKCSP procedure.

We can compute the filtration of a trial E_j by $W = (B^T P)^T$ as the projection matrix [14]:

$$Z_i = W \times E_i. \quad (12)$$

Decomposing the EEG based on (6) can be used to obtain the features utilized for classification. For every imagined movement direction, the classifier construction employs the variances owned by merely a small amount of m signals that are the fittest for discrimination. The signals Z_p ($p = 1 \cdots 2m$) maximizing the variance difference of motor imagery EEG on the left versus the right belong to those associated with the largest eigenvalues λ_1 and λ_2 . These signals are blank in the last and first rows in Z because of the computation of W

$$f_p = \frac{\text{var}(Z_p)}{\sum_{i=1}^{2m} \text{var}(Z_i)}. \quad (13)$$

TABLE 1: Data description for dataset IVa in BCI Competition III.

Subject	aa	al	av	aw	ay
Number of training samples	168	224	84	56	28
Number of test samples	112	56	196	224	252

The linear classifier can be calculated by using the feature vectors f_p of right and left trials. The log-transformation contributes to approximating the standard data distribution.

3. Experiments

3.1. Data Preparation. In this study, we employed the IVa dataset from BCI Competition III [22]. The dataset includes EEG data containing a classification task of motor imagery with two levels: (1) imagery movement of the right hand (denoted by R) and (2) imagery movement of the right foot (denoted by F). We employed 118 electrodes to measure EEG signals in every trial from five different subjects, and each subject involved the performance of 280 trials. Table 1 presents a summary of the data descriptions, in which the number of subjects av, aw, ay of training samples is fewer than those of the test samples.

TABLE 2: Classification accuracy of TKCSP on the dataset.

Source	Target				
	aa (%)	al (%)	av (%)	aw (%)	ay (%)
aa	-	80.58	50.17	84.33	80.41
al	67.20	-	63.87	90.58	81.98
av	50.00	86.11	-	80.10	55.13
aw	62.23	93.88	54.39	-	50.00
ay	50.00	91.00	65.67	50.00	-
aa + al	-	-	57.43	87.69	84.65
aa + av	-	84.58	-	81.56	74.11
aa + aw	-	87.80	51.76	-	51.53
aa + ay	-	84.58	-	81.56	74.11
al + av	59.27	-	-	88.35	50.00
al + aw	68.10	-	61.96	-	50.00
al + ay	62.92	-	68.47	78.16	-
av + aw	52.44	93.11	-	-	50.00
av + ay	45.30	89.38	-	74.98	-
aw + ay	58.60	91.65	61.25	-	-
aa + al + av	-	-	-	88.10	73.25
aa + al + aw	-	-	50.00	-	58.60
aa + al + ay	-	-	58.47	80.01	-
aa + av + aw	-	83.37	-	-	50.00
aa + av + ay	-	85.68	-	78.10	-
aa + aw + ay	-	89.59	50.00	-	-
al + av + aw	62.56	-	-	-	50.00
al + av + ay	52.10	-	-	75.48	-
al + aw + ay	63.13	-	52.47	-	-
av + aw + ay	55.65	91.67	-	-	-
al + av + aw + ay	62.07	-	-	-	-
aa + av + aw + ay	-	87.68	-	-	-
aa + al + aw + ay	-	-	60.63	-	-
aa + al + av + ay	-	-	-	81.20	-
aa + al + av + aw	-	-	-	-	53.19

Each trial was considered an $M \times T$ matrix E_i , in which M represents the electrode amount and the time point amount sampled. EEG signals measured were band-pass decomposed (8–30 Hz). SVM (Support Vector Machine) involving linear kernel was utilized as the classifier. The proportion of the number of samples properly classified to the aggregate number of used samples in this test was employed to evaluate the classification precision.

Our establishment of a dataset (containing the target domain and source domain) for cross-domain classification is described as follows. The dataset of each subject could become the target domain (ay, aw, av, al, aa), while the dataset of other subjects could become the source domains. This strategy of dataset construction ensured the relevance between domains of unlabeled and labeled data, as they were located in the same top-level categories. Accordingly, $C_4^1 + C_4^2 + C_4^3 + C_4^4 = 15$ datasets of the source domains were generated for each target domain. It was possible to generate five dataset groups, including $5 \times 15 = 75$ datasets.

3.2. Experimental Results. In this section, TKCSP and six competitive methods are evaluated based on classification accuracy [8, 11, 23]. We established five dataset groups from the dataset described above. Each dataset group includes four source subjects in source domains and one target subject as target domain. If one subject is the target domain, it will no longer appear in the source domains, so that each target domain corresponds to 15 different source domains. The first column of Table 2 shows the different source domains, and the second column to the sixth column of Table 2 show the classification accuracy of each target domain in its source domains, respectively. Among them, the highest classification accuracy of target domain aa was 68.10% and the corresponding source domain was al + aw; the highest classification accuracy of target domain al was 93.88% and the corresponding source domain was aw; the highest classification accuracy of target domain av was 68.47% and the corresponding source domain was al + ay; the highest classification accuracy of target domain aw is 68.10% and the

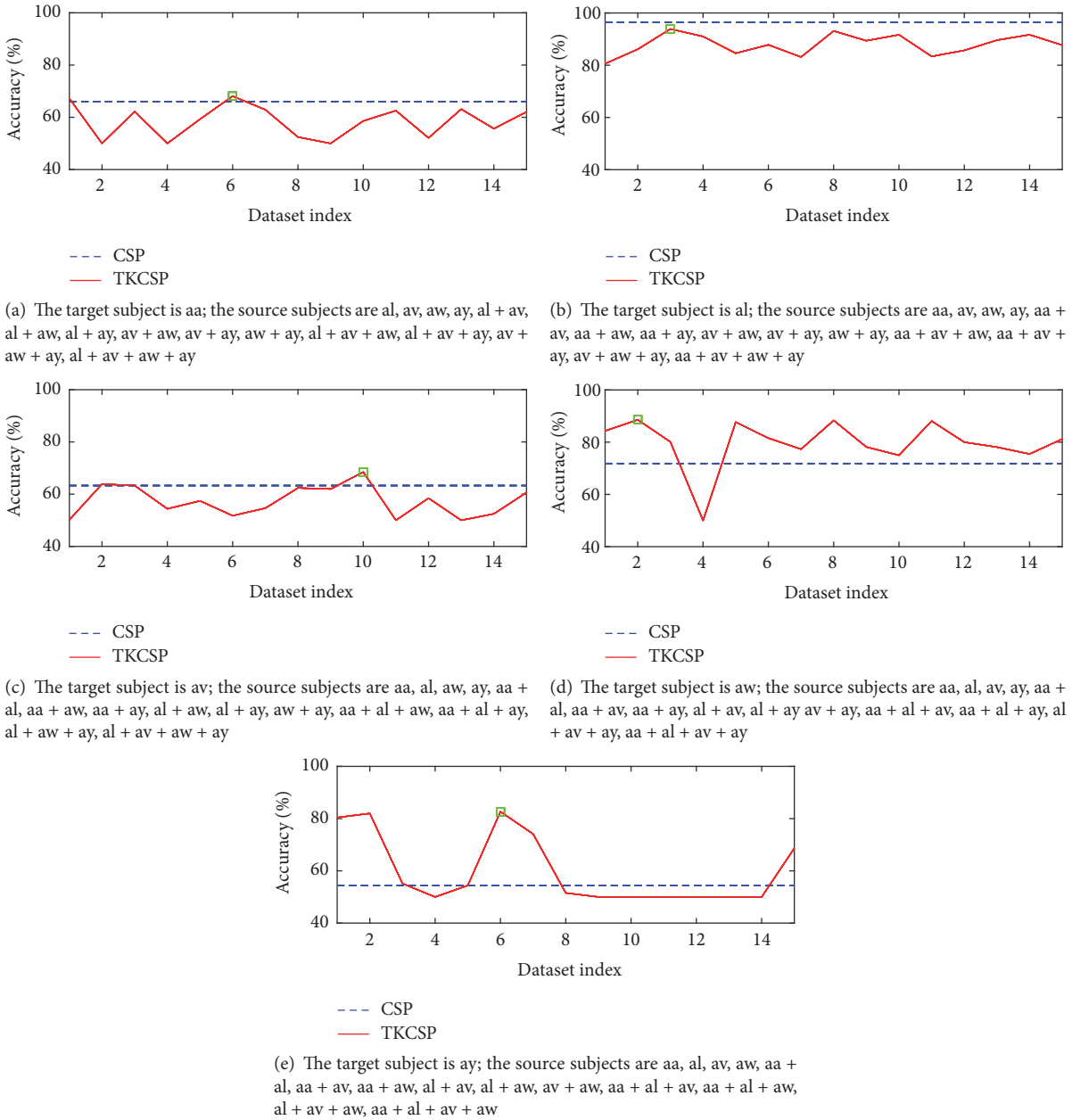


FIGURE 3: Classification accuracy of TKCSP and CSP on the dataset.

corresponding source domain is al; the highest classification accuracy of target domain ay is 68.10% and the corresponding source domain is aa + al.

To be complete, we detail the results of TKCSP method and CSP approach on all of 5 dataset groups in Figures 3(a), 3(b), 3(c), 3(d), and 3(e), where each figure presents the results of each group. In Figure 3, the blue dashed line indicates the classification accuracy of CSP algorithm, the red solid line indicates the classification accuracy of TKCSP algorithm in different source domains, and the green square indicates the best classification accuracy of TKCSP. The horizontal axis of green square is corresponding to the optimal source domain. The results show that the

classification accuracy of TKCSP method is better than that of CSP algorithm.

Table 3 lists the classification (recognition) precisions of five comparison approaches and TKCSP on dataset IVa. Figure 4 visually depicts the results for improved accessibility. The performance achieved by TKCSP is significantly better than those achieved by the five comparison approaches. Several observations can be made from these results.

Firstly, TKCSP achieves classification precision on the aw and aa datasets as 90.58% and 68.47%, respectively. These are higher than those of the five comparison approaches. Moreover, TKCSP achieves an average classification precision on these datasets as 81.14%, providing a significant performance

TABLE 3: Comparison of classification accuracy for TKCSP and 6 competitive methods.

Subject	aa (%)	al (%)	av (%)	aw (%)	ay (%)	Mean (%)
CSP	66.07	96.43	63.30	71.88	54.40	70.42
RCSP	71.43	96.43	63.30	71.88	86.90	77.98
CSP SJ-to-SJ	67.76	98.41	60.20	78.72	74.78	75.97
ssCSP	67.00	94.62	58.26	89.35	85.71	78.99
mtCSP	72.33	94.62	68.39	65.57	83.14	76.81
ss + mtCSP	71.43	94.63	66.32	88.40	74.93	79.17
TKCSP	68.10	93.88	68.47	90.58	84.65	81.14

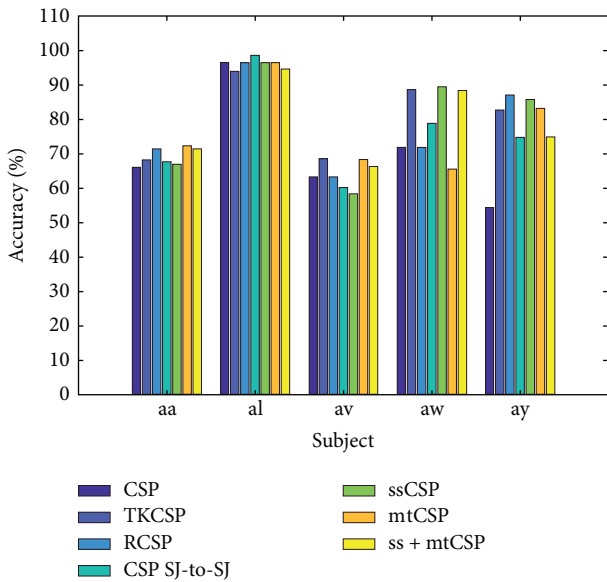


FIGURE 4: Comparison of classification accuracies for TKCSP and 6 competitive methods.

improvement of 1.97% over ss + mtCSP, the best competitive approach. It is strongly verified by the consistent performance improvements on these datasets that TKCSP can successfully establish powerful domain kernels for classification of cross-domain motor imagery.

Then, a composite covariance matrix as a weighted total of covariance matrices, including subjects resulting in a composite CSP, is determined by CSP for subject-to-subject transfer (CSP SJ-to-SJ). This approach thus achieves an average classification precision of 75.97%.

Thirdly, regularizing CSP (RCSP) is intended to regularize the covariance matrix to the mean covariance matrix of other subjects for improving its estimation performance. Such regularization is particularly promising in settings with small samples. Furthermore, this approach achieves an average classification precision of 77.98%.

Finally, the stationary subspace CSP (ssCSP) focuses on the nonstationarity issue while multitask CSP (mtCSP) focuses on the estimation issue. The combined mtCSP and

ssCSP (ss + mtCSP) method employs both approaches. That is, the nonstationary subspace acquired by ssCSP is firstly projected, and then the spatial filters are computed with mtCSP by regularization parameters acquired when it is applied to the initial data. The three above approaches achieve an average classification precision of 78.99%, 76.81%, and 79.17%, respectively.

In particular, TKCSP can assess the various cluster structures and naturally matches them between multiple domains. This procedure is achieved by TKCSP through the matching between the source domain kernel and kernel extrapolated from the target domain, while simultaneously increasing (declining) the domain-invariant (domain independent) eigenspectrum. The superior performance of TKCSP can be explained by this advantage.

4. Conclusion

In this paper, we proposed the TKCSP method to lower the training trial amount and improve the performance via learning a domain-independent kernel. To this end, direct matching of distributions between target subjects and source subjects within the kernel space is conducted. TKCSP and six competitive approaches were evaluated on EEG datasets provided by BCI Competition III. The results showed that the performance of the best approach, RCSP, was better than that of CSP by nearly 1.97% in terms of the mean classification precision. The results also revealed that RCSP can perform effective subject-to-subject transfer. Therefore, the behaviors matched with knowledge of neurophysiology could be classified by the TKCSP approach.

Notations

Z, X : Source/target domain
 m, n : Source/target examples
 d, c : Features/classes
 γ, ζ : Eigenvectors/damping factor
 \mathbf{X} : Input data matrix
 \mathbf{K} : Kernel matrix
 Φ : Eigenvector matrix
 Λ : Eigenvalue matrix.

Conflicts of Interest

The authors declare that there are no conflicts of interest.

Acknowledgments

This work was supported in part by the Department of S and T for Social Development of China (2014BAF08B01); Program for Innovative Research Team of Ministry of Education of China (IRT1203); the youth talent support program of Beihang University, Key Laboratory of Precision Opto-Mechatronics Technology (Beihang University), Ministry of Education. The authors would like to thank the Laboratory of Brain-Computer Interfaces at the Graz University of Technology for providing their data.

References

- [1] A. Cichocki, Y. Washizawa, T. Rutkowski et al., “Noninvasive BCIs: multiway signal-processing array decompositions,” *The Computer Journal*, vol. 41, no. 10, pp. 34–42, 2008.
- [2] T. Ebrahimi, J.-M. Vesin, and G. Garcia, “Brain-computer interface in multimedia communication,” *IEEE Signal Processing Magazine*, vol. 20, no. 1, pp. 14–24, 2003.
- [3] J. R. Wolpaw, N. Birbaumer, D. J. McFarland, G. Pfurtscheller, and T. M. Vaughan, “Brain-computer interfaces for communication and control,” *Clinical Neurophysiology*, vol. 113, no. 6, pp. 767–791, 2002.
- [4] Y. Ma, X. Ding, Q. She, Z. Luo, T. Potter, and Y. Zhang, “Classification of motor imagery EEG signals with support vector machines and particle swarm optimization,” *Computational and Mathematical Methods in Medicine*, vol. 2016, Article ID 4941235, 8 pages, 2016.
- [5] S. J. Pan and Q. Yang, “A survey on transfer learning,” *IEEE Transactions on Knowledge and Data Engineering*, vol. 22, no. 10, pp. 1345–1359, 2010.
- [6] M. Long, J. Wang, J. Sun, and P. S. Yu, “Domain invariant transfer kernel learning,” *IEEE Transactions on Knowledge and Data Engineering*, vol. 27, no. 6, pp. 1519–1532, 2015.
- [7] A. Satti, C. Guan, D. Coyle, and G. Prasad, “A covariate shift minimization method to alleviate non-stationarity effects for an adaptive brain-computer interface,” in *Proceedings of the 2010 20th International Conference on Pattern Recognition, ICPR 2010*, pp. 105–108, Turkey, August 2010.
- [8] H. Kang, Y. Nam, and S. Choi, “Composite common spatial pattern for subject-to-subject transfer,” *IEEE Signal Processing Letters*, vol. 16, no. 8, pp. 683–686, 2009.
- [9] F. Lotte and C. Guan, “Learning from other subjects helps reducing brain-computer interface calibration time,” in *Proceedings of the 35th IEEE International Conference on Acoustics, Speech, and Signal Processing (ICASSP '10)*, pp. 614–617, Dallas, Tex, USA, March 2010.
- [10] D. Devlaminc, B. Wyns, M. Grosse-Wentrup, G. Otte, and P. Santens, “Multisubject learning for common spatial patterns in motor-imagery BCI,” *Computational Intelligence and Neuroscience*, vol. 2011, Article ID 217987, 9 pages, 2011.
- [11] W. Samek, F. C. Meinecke, and K. Muller, “Transferring subspaces between subjects in brain—computer interfacing,” *IEEE Transactions on Biomedical Engineering*, vol. 60, no. 8, pp. 2289–2298, 2013.
- [12] W. Tu and S. Sun, “A subject transfer framework for EEG classification,” *Neurocomputing*, vol. 82, pp. 109–116, 2012.
- [13] H. Albalawi and X. Song, “A study of kernel CSP-based motor imagery brain computer interface classification,” in *Proceedings of the 2012 IEEE Signal Processing in Medicine and Biology Symposium, SPMB 2012*, USA, December 2012.
- [14] H. Ramoser, J. Müller-Gerking, and G. Pfurtscheller, “Optimal spatial filtering of single trial EEG during imagined hand movement,” *IEEE Transactions on Neural Systems and Rehabilitation Engineering*, vol. 8, no. 4, pp. 441–446, 2000.
- [15] X. Yin, B. Xu, C. Jiang et al., “A hybrid BCI based on EEG and fNIRS signals improves the performance of decoding motor imagery of both force and speed of hand clenching,” *Journal of Neural Engineering*, vol. 12, no. 3, Article ID 036004, 2015.
- [16] K. Zhang, I. W. Tsang, and J. T. Kwok, “Improved Nystrom lowrank approximation and error analysis,” in *Proceedings of the 25th International Conference on Machine Learning*, 2008.
- [17] C. Williams and M. Seeger, “Using the Nystrom method to speed up kernel machines,” in *Proceedings of the Advances in Neural Information Processing Systems*, 2001.
- [18] R. Johnson and T. Zhang, “Graph-based semi-supervised learning and spectral kernel design,” *IEEE Transactions on Information Theory*, vol. 54, no. 1, pp. 275–288, 2008.
- [19] R. Jin, T. Yang, M. Mahdavi, Y.-F. Li, and Z.-H. Zhou, “Improved bounds for the Nystrom method with application to kernel classification,” *Institute of Electrical and Electronics Engineers Transactions on Information Theory*, vol. 59, no. 10, pp. 6939–6949, 2013.
- [20] L. Duan, D. Xu, and I. W.-H. Tsang, “Domain adaptation from multiple sources: a domain-dependent regularization approach,” *IEEE Transactions on Neural Networks and Learning Systems*, vol. 23, no. 3, pp. 504–518, 2012.
- [21] W. Dai, G. Xue, Q. Yang, and Y. Yu, “Co-clustering based classification for out-of-domain documents,” in *Proceedings of the 13th ACM SIGKDD international conference*, p. 210, San Jose, Calif, USA, August 2007.
- [22] B. Blankertz, K.-R. Müller, D. J. Krusienski et al., “The BCI competition III: validating alternative approaches to actual BCI problems,” *IEEE Transactions on Neural Systems and Rehabilitation Engineering*, vol. 14, no. 2, pp. 153–159, 2006.
- [23] F. Lotte and C. Guan, “Regularizing common spatial patterns to improve BCI designs: unified theory and new algorithms,” *IEEE Transactions on Biomedical Engineering*, vol. 58, no. 2, pp. 355–362, 2011.

Research Article

Direct-Current Electric Field Distribution in the Brain for Tumor Treating Field Applications: A Simulation Study

Yung-Shin Sun 

Department of Physics, Fu-Jen Catholic University, New Taipei City 24205, Taiwan

Correspondence should be addressed to Yung-Shin Sun; 089957@mail.fju.edu.tw

Received 25 October 2017; Revised 25 December 2017; Accepted 30 January 2018; Published 22 February 2018

Academic Editor: Marta Parazzini

Copyright © 2018 Yung-Shin Sun. This is an open access article distributed under the Creative Commons Attribution License, which permits unrestricted use, distribution, and reproduction in any medium, provided the original work is properly cited.

Tumor Treating Fields (TTFields) in combination with chemotherapy and/or radiotherapy have been clinically reported to provide prolonged overall survival in glioblastoma patients. Alternating electric fields with frequencies of 100~300 kHz and magnitudes of 1~3 V/cm are shown to suppress the growth of cancer cells via interactions with polar molecules within dividing cells. Since it is difficult to directly measure the electric fields inside the brain, simulation models of the human head provide a useful tool for predicting the electric field distribution. In the present study, a three-dimensional finite element head model consisting of the scalp, the skull, the dura, the cerebrospinal fluid, and the brain was built to study the electric field distribution under various applied potentials and electrode configurations. For simplicity, a direct-current electric field was used in the simulation. The total power dissipation and temperature elevation due to Joule heating in different head tissues were also evaluated. Based on the results, some guidelines are obtained in designing the electrode configuration for personalized glioblastoma electrotherapy.

1. Introduction

Glioblastoma, or glioblastoma multiforme (GBM), is the most aggressive malignant brain tumor, having an incidence of about 4.43 out of 100,000 persons in the United States [1]. Initial symptoms of glioblastoma include headaches, personality changes, epilepsy, nausea, and hemiparalysis, and unconsciousness may be the sign of exacerbation [2]. Surgery, if applicable, is the first step of GBM treatment, and then radiotherapy and chemotherapy could follow. For radiotherapy, patients who received total radiation doses of 50~60 Gy were reported to have 1.6~2.3 times longer life expectancy compared with those receiving no radiotherapy [3]. For chemotherapy, patients given standard radiation plus temozolomide (an oral chemotherapy drug) survived a median of 14.6 months compared to 12.1 months for those receiving radiation alone [4]. Recently, immunotherapy and gene therapy have also been applied in GBM treatment [5–7]. Although various novel therapies were clinically reported to extend patient survival rate, glioblastoma is considered incurable, with a medium survival period of 14.6 months and a two-year survival rate of 30% [8].

As a new therapeutic technology for treating GBM, Tumor Treating Fields (TTFields) suppress the growth of cancer cells by applying alternating electric fields (EFs) with frequencies of 100~300 kHz and magnitudes of 1~3 V/cm. EFs were shown to play important roles in various physiological processes such as cell division and wound healing [9, 10]. Direct-current (dc) or alternating current (ac) EFs were reported to induce collective and directional migration of adherent cells, phenomena termed electrotaxis [11–13]. Compared to radiotherapy or chemotherapy, TTFields are considered safer and produce fewer side effects. Kirson et al. found that TTFields inhibit cancerous cell growth via an antimicrotubule mechanism of action [14]. In brief, applied alternating EFs interact with polar molecules (i.e., microtubules) within dividing cells, leading to the disruption of microtubule spindle formation during the mitotic phase [15]. Such TTFields have also been shown to arrest *in vitro* cell proliferation of various cancers in frequency- and dose-dependent manners. For example, the optimal frequency was 100 kHz for mouse melanoma, 150 kHz for human breast carcinoma, and 200 kHz for rat glioma [14]. And to kill 80% of cancer cells, the required intensity was 1.3 V/cm for mouse

melanoma, 2.2 V/cm for rat glioma, 2.7 V/cm for human non-small cell lung carcinoma, and 3 V/cm for human breast carcinoma [14]. TTFields were considered most effective when applied for 24 hours to cells which undergo mitosis and are oriented roughly along the direction of EFs [16].

Clinically, when combined with chemotherapy, TTFields worked well in treating various cancers. For example, Gharaee et al. demonstrated that TTFields of 150 kHz coadministered with doxorubicin can be used as an alternative strategy for breast cancer therapy to improve the effects of the drugs and increase the sensitivity of cancer cells [17]. Giladi et al. investigated the response of Lewis lung carcinoma and KLN205 squamous cell carcinoma in mice treated with TTFields in combination with pemetrexed, cisplatin, or paclitaxel and concluded that combining TTFields with these therapeutic agents enhanced treatment efficacy in comparison with the respective single agents and control groups in all animal models [18]. Moreover, TTFields in combination with paclitaxel and gemcitabine were reported therapeutically effective against ovarian and pancreatic cancers, respectively [19, 20]. The Optune™ (formerly NovoTTF™-100A) system developed by Novocure (<https://www.novocure.com>) is a portable medical device used to deliver low-intensity (>0.7 V/cm), intermediate-frequency (200 kHz) alternating EFs to the brain via noninvasive transducer arrays attached to the shaved scalp of glioblastoma patients. It has been approved for the treatment of GBM in the European Union, Switzerland, Australia, Israel, Japan, and the United States. As a pilot clinical trial, 10 patients with recurrent glioblastoma were treated with TTFields as a monotherapy. No device-induced serious side effects were observed after more than 70 months of cumulative treatment except mild to moderate contact dermatitis due to electrodes [14]. In 2012, a phase III trial of NovoTTF (20–24 h/day) in the treatment of patients with recurrent glioblastoma was conducted. Although no improvement in overall survival was observed, efficacy and activity of this chemotherapy-free treatment system appeared comparable to traditional chemotherapy [21]. Wong et al. treated a series of patients with NovoTTF-100A and bevacizumab alone or in combination with a regimen consisting of 6-thioguanine, lomustine, capecitabine, and celecoxib (TCCC) and found that, compared to the former group, the latter group exhibited a trend for prolonged overall survival [22]. Recently, an international, multicenter, prospective, and randomized phase III trial (EF-14) was conducted for testing the efficacy of combining TTFields with standard chemotherapy of temozolomide (TMZ) in 695 newly diagnosed GBM patients. The results demonstrated better progression free survival and overall survival in patients treated with a combined therapy of TTFields and TMZ compared with those receiving TMZ alone [23].

In a TTFIELD-based device, transducer arrays of electrodes are placed on the patient's shaved scalp. As mentioned earlier, it is of importance to be able to deliver alternating EFs of desired intensity to the tumor inside the brain. However, with exosomatic applied TTFields, it is difficult to measure the distribution of the EFs inside the brain. The only one intracranial measurement conducted by Kirson et al. indicated that effective (1–2 V/cm) TTFields could be generated at the center of

the brain by applying 50 V to surface electrodes placed on the scalp [14]. Therefore, simulation models of the human head provide a useful tool for predicting the EF distribution inside the brain. It may also help to personalize the treatment by adjusting the positions of electrodes to better treat tumors at certain locations with desired intensities. In this study, I built a three-dimensional (3D) head model consisting of the scalp, the skull, the dura, the cerebrospinal fluid, and the brain. Each type of tissue has its own conductivity, relative permittivity, density, and heat capacity. Using the finite element method (FEM) and the commercial software COMSOL Multiphysics, I simulated the distribution of EFs inside the brain under different electrode configurations and applied intensities. For simplicity, a direct-current electric field was used in the simulation. The total power dissipation due to Joule heating in different head tissues was also evaluated. The results are believed to be helpful in designing the electrode configuration for personalized GBM electrotherapy.

2. Materials and Methods

To investigate how the magnitudes of applied voltage affect the intensities of EFs generated inside the brain, a dc module instead of ac module is used. Within various head tissues, the EF resulting from a constant dc can be treated as quasi-stationary over time. By flowing a constant dc through volume conductors of homogeneous and isotropic electrical properties, steady dcEFs are generated. The distribution of electric potential (V) is then governed by the Laplace equation, $\nabla^2 V = 0$, with appropriate boundary conditions. In the Dirichlet boundary condition, a fixed scalar potential (i.e., the applied voltage) is specified on the surface of the model.

2.1. The Head Model. A 3D finite element head model was built using the software COMSOL Multiphysics (Version 4.4, MI, USA). The geometry of the head is shown in Figure 1(a) [24]. The scalp, consisting of five layers, has a thickness of 0.6 mm. The skull, supporting the structures of the face and providing a protective cavity for the brain, has a thickness of 1 mm. The dura, having a thickness of 0.3 mm, is a thick membrane surrounding the brain and spinal cord. The cerebrospinal fluid, a clear, colorless body fluid acting as a cushion for the brain, has a thickness of 0.75 mm. The brain, having a radius of 50 mm, is composed of 40% of grey matter and 60% of white matter. As shown in Figure 1(b), the whole head is modeled as a half sphere with a radius of 52.65 mm. Figure 1(c) shows the finite element mesh made of 220,620 tetrahedral elements, 67,626 triangular elements, 2,642 edge elements, and 180 vertex elements.

2.2. Tissue Properties. The electrical properties of different head tissues are listed in Table 1. For simplicity, all tissues were modeled as homogenous, isotropic conductors with constant conductivities and relative permittivities throughout. The conductivities of the scalp, the skull, the dura, the cerebrospinal fluid, and the brain are 0.00105, 0.0529, 0.502, 2, and 0.108 Sm^{-1} , respectively. The relative permittivities of these five tissues were 1100, 295.5, 290, 109, and 1578, respectively. To evaluate temperature elevation due to Joule

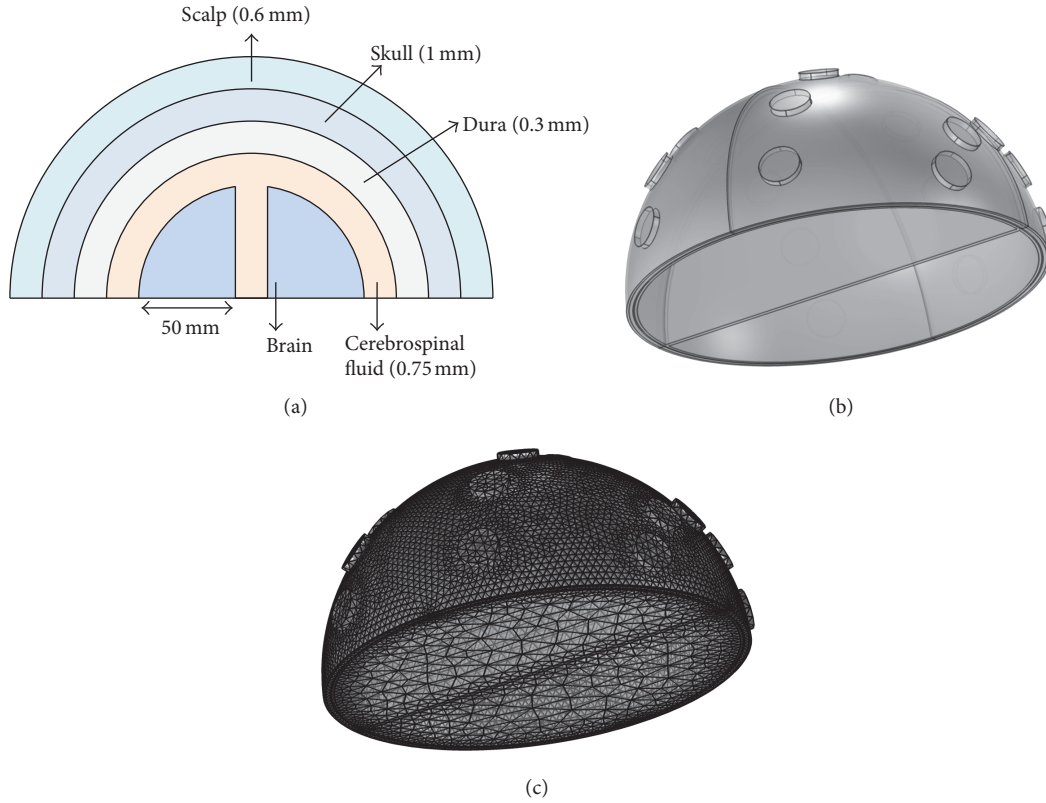


FIGURE 1: (a) The geometry of the head (not to scale). (b) The head model constructed in COMSOL. (c) The finite element mesh constructed in COMSOL.

TABLE 1: Dielectric properties, densities, and heat capacities of various brain tissues relevant to numerical simulations. Data obtained from the Foundation for Research on Information Technologies in Society (<https://www.itis.ethz.ch/virtual-population/tissue-properties/database/dielectric-properties/>).

	Conductivity ^a σ (S/m)	Relative permittivity ^a ϵ_r	Density D (kg/m ³)	Heat capacity s (J/kg°C)
Scalp	0.00105	1100	1109	3391
Skull	0.0529	295.5	1543	1793
Dura	0.502	290	1174	3364
Cerebrospinal fluid	2	109	1007	4096
Brain	0.108	1578	1043	3628

^aat 200 kHz.

heating, the densities and heat capacities of different head tissues are also listed in Table 1. The densities of the scalp, the skull, the dura, the cerebrospinal fluid, and the brain are 1109, 1543, 1174, 1007, and 1043 kgm⁻³, respectively. The heat capacities of these five tissues were 3391, 1793, 3364, 1096, and 3628, respectively.

2.3. Simulation Conditions. The head model is used to simulate the distribution of endogenous dcEF inside the brain. The Electric Currents (ec) module of the COMSOL Multiphysics

is used to solve the steady-state EF distribution. The following equations are used:

$$\begin{aligned}
 \nabla \cdot \mathbf{J} &= \mathbf{Q}, \\
 \mathbf{J} &= \sigma \mathbf{E} + \mathbf{J}_e, \\
 \mathbf{E} &= -\nabla V.
 \end{aligned} \tag{1}$$

In these equations, \mathbf{J} is the current density, \mathbf{Q} is the electric charge, σ is the electrical conductivity, \mathbf{E} is the electric

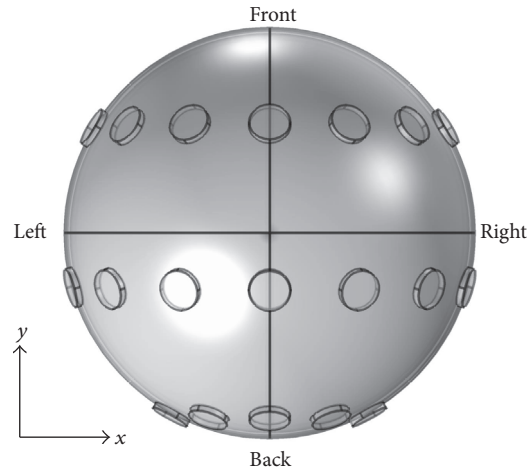


FIGURE 2: The configuration of the electrodes used in the head model.

field, \mathbf{J}_e is the externally generated current density, and V is the electric potential. The configuration of the electrodes is shown in Figure 2. As indicated, there are 19 copper electrodes in total, with 7 in the front, 7 in the middle, and 5 in the back. Each electrode is assigned a potential V (positive electrode, shown as “+”), a ground (negative electrode, shown as “-”), or a nude (neither positive nor negative). The x -, y -, and z -axes of the head model are also illustrated. The endogenous dcEF is shown in a cross-sectional view (of the xy , yz , or zx plane) and a line profile (along a given direction). The distributions of dcEFs inside the brain under different positive/negative electrode configurations and applied dcEF strengths are investigated. To achieve personalized treatment for GBM, various positive/negative electrode configurations are tested to focus the dcEFs on certain locations. Finally, the total power dissipation and temperature elevation due to Joule heating in different head tissues are evaluated using the densities and heat capacities of these tissues. Hyperpyrexia due to excessive Joule heating can cause serious side effects such as headache and burn.

3. Results and Discussion

First, a potential of 0.5 V was applied to the left 3 electrodes of the middle array, and the right 3 electrodes of the middle array were grounded, as shown in Figure 3(a). The x - y plane cross-sectional views of the endogenous dcEFs are shown in Figure 3(c) ($z = 47, 33,$ and 13 mm from left to right in Figure 3(b)). In all 3 subfigures, the dcEF strengths are the highest near the electrodes, but these values decrease rapidly as they cross the dura and the cerebrospinal fluid. dcEFs of only around 0.1 V/cm are attained near the outmost layer of brain and they are partially localized in very narrow regions. This dcEF strength is obviously not enough for GBM treatment, and a higher applied voltage is required. Figure 4 shows the x - y plane cross-sectional views ($z = 33$ mm) of the endogenous dcEFs with applied potentials of 2.5, 5, and 10 V (resp., from left to right). The electrode configuration is the same as that in Figure 3(a). Under an applied voltage of

2.5 V, dcEFs of 0.4~1 V/cm are generated in the cerebrospinal fluid and the outmost layer of the brain. Similar results are observed when the applied potential is increased to 5 V: dcEFs of 0.8~1.4 V/cm are generated in the cerebrospinal fluid and the outmost layer of the brain. At an applied potential of 10 V, dcEFs of >1.8 V/cm are attained in similar regions. In all 3 subfigures, the dcEFs are partially localized near the electrodes from this point of view (i.e., the x - y plane cross-sectional view). I will now check the distributions of dcEFs from different cross-sections.

Figure 5(a) shows another electrode configuration where potentials were applied to all electrodes of the front array, and all electrodes of the middle array were grounded. At an applied voltage of 5 V, the x - z plane cross-sectional view ($y = 0$ mm, as shown in Figure 5(b)) of the endogenous dcEF is illustrated in Figure 5(c). The dcEFs are distributed more or less uniformly throughout the cross-section and have strengths of only 0.025~0.04 V/cm. These intensities are not enough for GBM treatment. When the applied potential is increased to 100 V, the dcEF distribution is shown in Figure 5(d). The dcEF strengths increase to 0.5~1 V/cm, suitable for electrotherapy applications. These values are close to those reported by Kirson et al.: an applied potential difference of 50 V could generate a TTF field of 1~2 V/cm at the center of the brain [14]. Nine lines along the x -axis in that plane are shown in Figure 6(a). The dcEF profiles at applied potentials of 5 V and 100 V along these lines are illustrated in Figures 6(b) and 6(c), respectively. At 5 V, the dcEF strengths go from small (around 0.005~0.01 V/cm in the first 5 mm) to large (around 0.025~0.04 V/cm in the middle range) and then to small again (around 0.005~0.01 V/cm in the last 5 mm). Similarly at 100 V, the dcEF strengths go from small (around 0.1~0.3 V/cm in the first 5 mm) to large (around 0.5~1 V/cm in the middle range) and then to small again (around 0.1~0.3 V/cm in the last 5 mm).

Figure 7(a) shows another electrode configuration similar to that in Figure 5(a). Potentials were applied to all electrodes of the front array, and all electrodes of the back array were grounded. At an applied potential of 100 V, Figure 7(b)

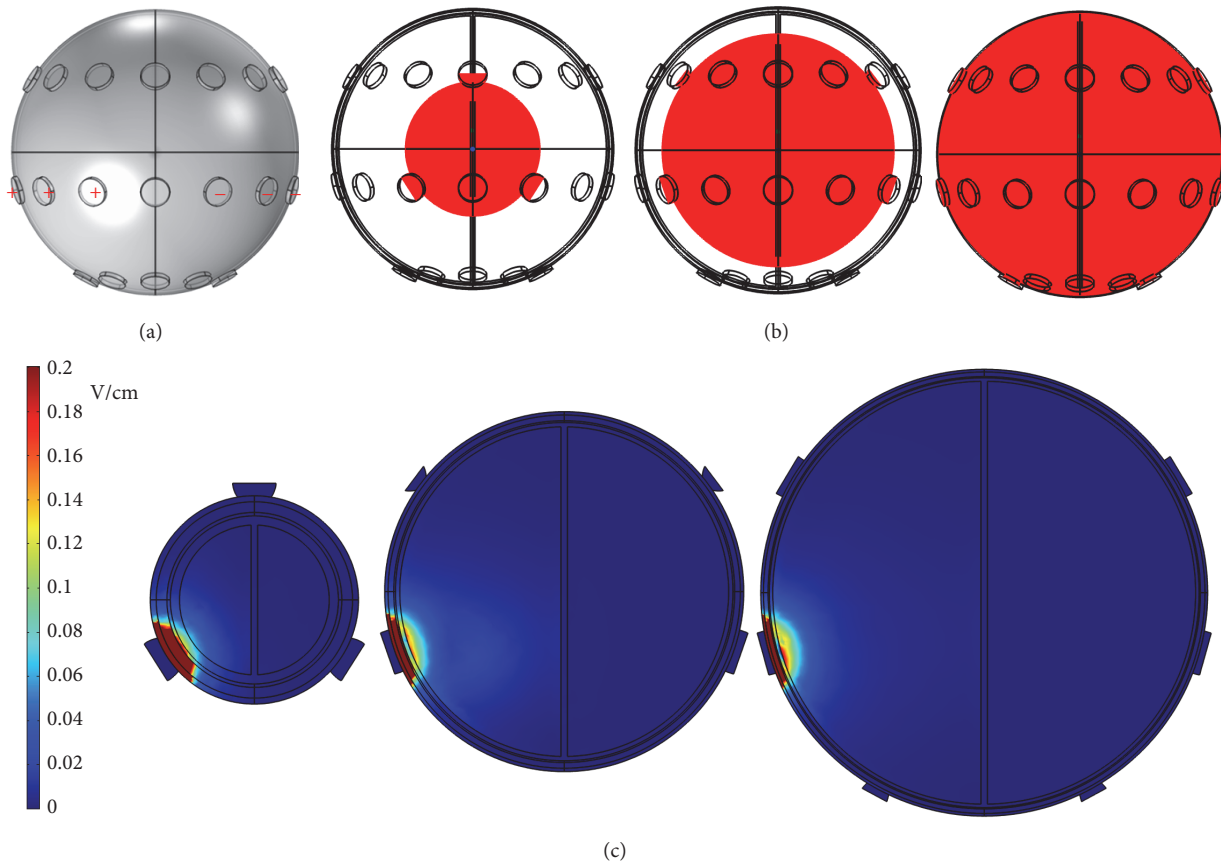


FIGURE 3: (a) The electrode configuration used to apply a potential of 0.5 V. (b) The x - y plane cross-sectional views at $z = 47, 33,$ and 13 mm from left to right. (c) The x - y plane cross-sectional views of the endogenous dcEFs corresponding to (b).

displays the dcEF distribution in the x - z plane cross-section ($y = 0$ mm), and Figure 7(c) shows 9 dcEF profiles along the x -axis in that plane. As indicated, the dcEFs are distributed more or less uniformly throughout the cross-section and have strengths of 0.5~1 V/cm, similar to those in Figures 5(d) and 6(c). The electrode configuration is then changed to that in Figure 8(a), where all electrodes of the front and middle arrays were assigned potentials and all others were grounded. At an applied voltage of 100 V, the dcEF distribution in the x - z plane cross-section ($y = 0$ mm) indicates that dcEFs are localized mainly along the boundary of the brain, as shown in Figure 8(b). Nine line profiles along the x -axis in that plane show that the dcEF strengths go from large (around 3~5 V/cm in the first 10 mm) to small (around 1~3 V/cm in the middle range) and then to large again (around 3~5 V/cm in the last 10 mm), as displayed in Figure 8(c).

Next, different electrode configurations are tested to see whether it is possible to focus the dcEFs on certain locations. Figure 9(a) shows the electrode configuration where the right 4 electrodes of the front array were assigned potentials and the right 4 electrodes of the middle array were grounded. At an applied potential of 100 V, the dcEF distribution in the x - z plane cross-section ($y = 0$ mm) is displayed in Figure 9(b). As illustrated, the dcEFs are distributed more or less uniformly

throughout one-half of the cross-section where positive and negative electrodes are assigned. The dcEF strengths range from 0.5 to 1 V/cm. When the left 4 electrodes of the front array were assigned potentials and the left 4 electrodes of the middle array were grounded (as shown in Figure 9(c)), the x - z plane cross-sectional view indicates that the dcEFs are distributed more or less uniformly throughout the other half of the cross-section. In the electrode configuration shown in Figure 10(a) where the left 2 electrodes of the front array are assigned potentials and the left 2 electrodes of the middle array are grounded, the dcEF distribution in the x - z plane cross-section ($y = 0$ mm) is displayed in Figure 10(b). The dcEFs, having strengths of 0.5~0.8 V/cm, are localized in the leftmost one-quarter of the cross-section where positive and negative electrodes are assigned. When the electrodes are switched to the next 2 electrodes on the right (see Figure 10(c)), the x - z plane cross-sectional view indicates that the dcEFs are localized in the top half of the second one-quarter of the cross-section, as displayed in Figure 10(d). Figure 11 shows the x - z plane cross-sectional views ($y = 0$ mm) of the endogenous dcEFs when (a) the leftmost electrodes of the front and middle arrays are assigned potentials and grounded, respectively; (b) the second electrodes from the left of the front and middle arrays are assigned potentials and

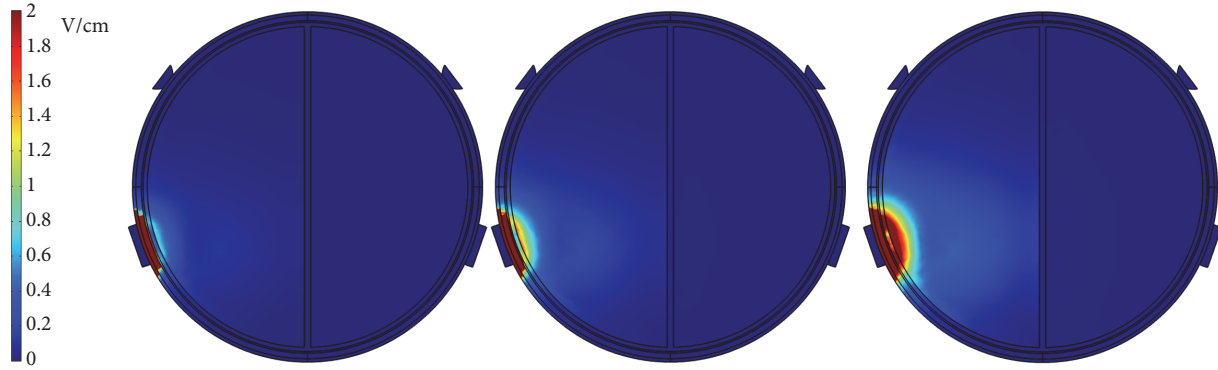


FIGURE 4: The x - y plane cross-sectional views ($z = 33$ mm) of the endogenous dcEFs with applied potentials of 2.5, 5, and 10 V from left to right.

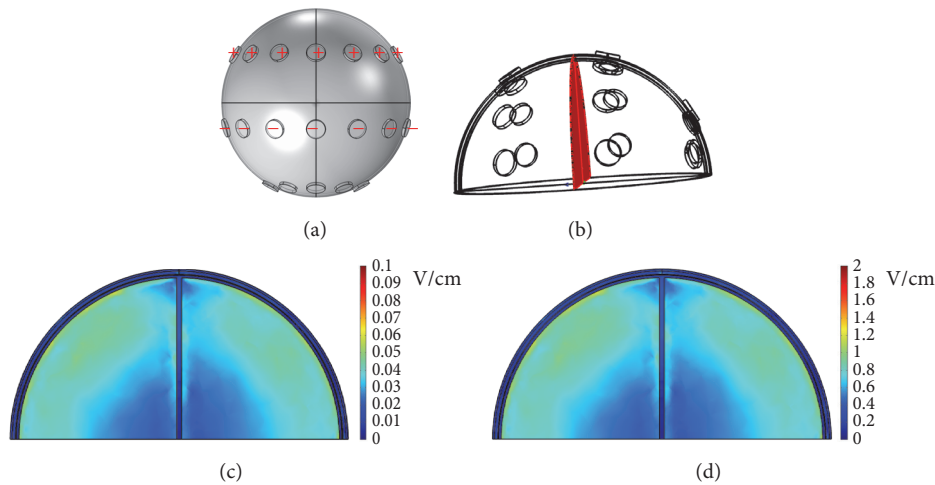


FIGURE 5: (a) The electrode configuration used to apply potentials of 5 V and 100 V. (b) The x - z plane cross-sectional view at $y = 0$ mm. (c) The x - z plane cross-sectional view of the endogenous dcEF at an applied potential of 5 V. (d) The x - z plane cross-sectional view of the endogenous dcEF at an applied potential of 100 V.

grounded, respectively; (c) the third electrodes from the left of the front and middle arrays are assigned potentials and grounded, respectively; (d) the center electrodes of the front and middle arrays are assigned potentials and grounded, respectively. As clearly shown, when the positive and negative electrodes move from left to right, the dcEFs shift accordingly. These dcEFs have similar strengths of 0.4~0.7 V/cm. These results indicate that the dcEFs can be focused on specific locations by suitably assigning the positive and negative electrodes (numbers and relative locations). This is helpful in conducting personalized GBM treatment.

To visualize the dcEF distributions from different points of view, various electrode configurations are tested. Figure 12(a) shows the y - z plane cross-section located at $x = 25$ mm. In the electrode configuration where the rightmost electrode of the front array was assigned potentials and the center electrode of the front array was grounded (see Figure 12(b)), the dcEF distribution in that plane is displayed

in Figure 12(d). At an applied potential of 100 V, the dcEFs are localized in the region between positive and negative electrodes. The dcEF strengths are around 0.6~1.4 V/cm. As the electrode configuration is changed to that in Figure 12(c) where the rightmost electrodes of the front and middle arrays were assigned potentials and the center electrodes of the front and middle arrays were grounded, the dcEF distribution is shown in Figure 12(e). Similarly, the dcEFs are distributed in regions between positive and negative electrodes, but the dcEF strengths in the middle array (0.6~0.8 V/cm, the center part of Figure 12(e)) are smaller than those in the front array (0.6~1.4 V/cm, the right part of Figure 12(e)). Figure 13(a) shows the x - y plane cross-section located at $z = 33$ mm. In the electrode configuration where the center electrodes of the front and back arrays were assigned potentials and grounded, respectively (see Figure 13(b)), the dcEF distribution in that plane is displayed in Figure 13(d). At an applied potential of 100 V, the dcEFs are localized close to the positive electrode,

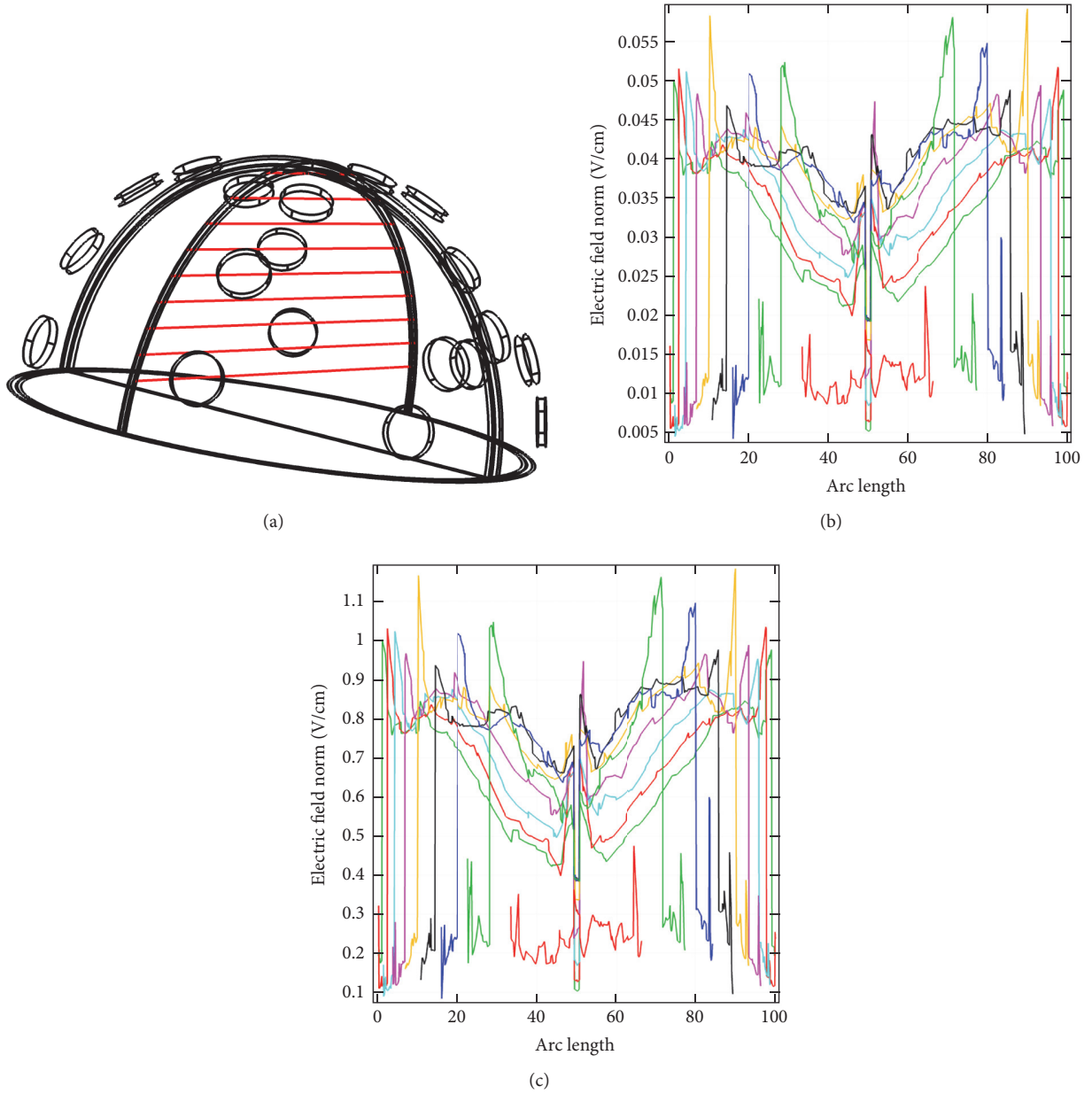


FIGURE 6: (a) Nine lines along the x -axis in the plane shown in Figure 5(b). (b) The dcEF profiles at an applied potential of 5 V along these lines. (c) The dcEF profiles at an applied potential of 100 V along these lines.

with strengths of 2.5~4.5 V/cm. Figure 13(c) shows another electrode configuration where the middle 3 electrodes of the front array were assigned potentials and the middle 3 electrodes of the back array were grounded. Figure 13(e), displaying the dcEF distribution in that plane, indicates again that the dcEFs are localized close to the positive electrodes.

Finally, I investigate the total power dissipation density and temperature elevation due to Joule heating in different head tissues. The total power dissipation density (P in W/m^3) is evaluated in each of the head tissues using the COMSOL Multiphysics software. The following equation is used:

$$Q = ms\Delta T. \quad (2)$$

In this equation, Q is the electrically generated heat in the tissue, m is the mass of the tissue, s is the heat capacity of the tissue, and ΔT is the temperature elevation in the tissue. By using $m = DV$, where D is the density of the tissue, the following equation is derived:

$$PV\Delta t = DVs\Delta T, \text{ or} \quad (3)$$

$$\frac{\Delta T}{\Delta t} = \frac{P}{Ds}.$$

The temperature increase per second can be calculated from total power dissipation density, density, and heat

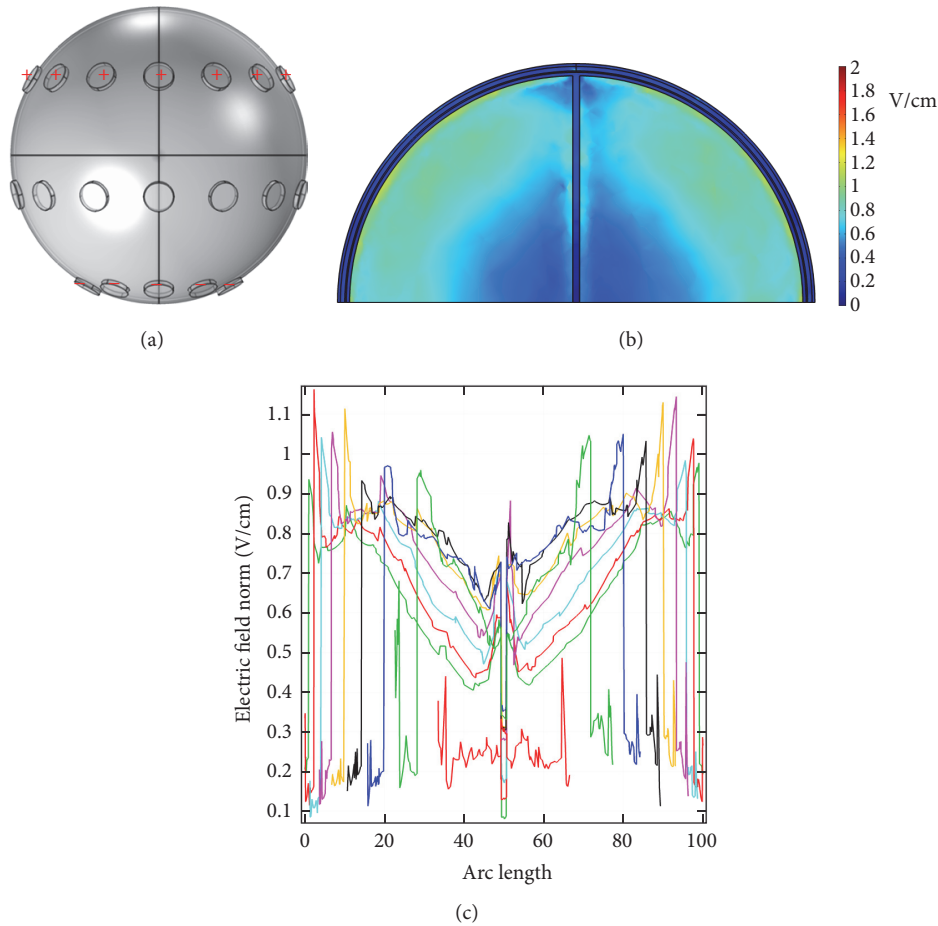


FIGURE 7: (a) The electrode configuration used to apply a potential of 100 V. (b) The x - z plane cross-sectional view ($y = 0$ mm) of the endogenous dcEF. (c) The dcEF profiles corresponding to 9 lines in the x - z plane cross-section.

TABLE 2: Total power dissipation densities and temperature increases per second of various brain tissues under an applied potential of 100 V in the electrode configuration shown in Figure 7(a).

	Total power dissipation density (W/m^3)	Temperature increase per second ($^{\circ}\text{C}/\text{s}$)
Scalp	9.99×10^5	0.27
Skull	1.81×10^4	6.54×10^{-3}
Dura	2.42×10^3	6.12×10^{-4}
Cerebrospinal fluid	2.19×10^3	5.31×10^{-4}
Brain	41.97	1.11×10^{-5}

capacity. Table 2 lists these values under an applied potential of 100 V in the electrode configuration shown in Figure 7(a). As indicated, the total power dissipation density in the scalp is $9.99 \times 10^5 \text{ W}/\text{m}^3$, and this value decreases to $1.81 \times 10^4 \text{ W}/\text{m}^3$ in the skull, to $2.42 \times 10^3 \text{ W}/\text{m}^3$ in the dura, to $2.19 \times 10^3 \text{ W}/\text{m}^3$ in the cerebrospinal fluid, and finally to $41.97 \text{ W}/\text{m}^3$ in the brain. The corresponding temperature increases per second

TABLE 3: Total power dissipation densities and temperature increases per second of various brain tissues under an applied potential of 100 V in the electrode configuration shown in Figure 8(a).

	Total power dissipation density (W/m^3)	Temperature increase per second ($^{\circ}\text{C}/\text{s}$)
Scalp	1.87×10^6	0.5
Skull	3.39×10^4	0.012
Dura	4.12×10^3	1.04×10^{-3}
Cerebrospinal fluid	2.74×10^3	6.6×10^{-4}
Brain	46.5	1.23×10^{-5}

in these 5 tissues are 0.27, 6.54×10^{-3} , 6.12×10^{-4} , 5.31×10^{-4} , and $1.11 \times 10^{-5} \text{ }^{\circ}\text{C}$, respectively. For all tissues except the scalp, these increases are too small to be considered harmful. Since the scalp is in direct contact with the electrodes, a significant temperature elevation is noticed. This increase can be balanced via suitable conduction as the scalp is exposed to surrounding air at a constant room temperature. Table 3

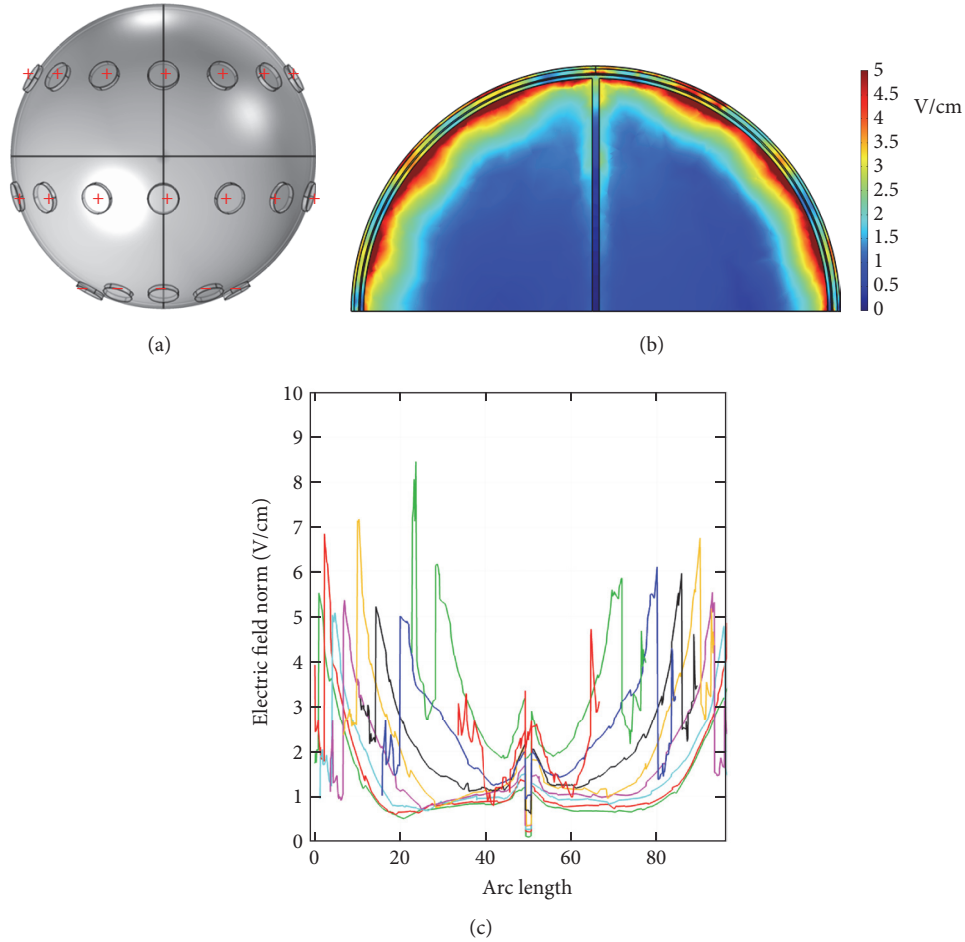


FIGURE 8: (a) The electrode configuration used to apply a potential of 100 V. (b) The x - z plane cross-sectional view ($y = 0$ mm) of the endogenous dcEF. (c) The dcEF profiles corresponding to 9 lines in the x - z plane cross-section.

lists the total power dissipation densities and temperature increases per second of various brain tissues under an applied potential of 100 V in the electrode configuration shown in Figure 8(a). Temperature increases per second of 0.5, 0.012, 1.04×10^{-3} , 6.6×10^{-4} , and 1.23×10^{-5} °C are calculated in the scalp, the skull, the dura, the cerebrospinal fluid, and the brain, respectively. To evaluate the maximum possible temperature increase, I employ a new electrode configuration where all electrodes were assigned potentials except the center one of the back array which was grounded. Table 4 lists all simulated and calculated values. The temperature increases per second in these 5 tissues are 0.65, 0.016, 1.36×10^{-3} , 8.53×10^{-4} , and 1.62×10^{-5} °C, respectively. This heat produced due to Joule heating can be easily dissipated via conduction, convection, and radiation from the scalp to the air. These results indicate that, under an applied voltage of 100 V, these EFs are thought to be harmless to the brain and all surrounding tissues.

4. Conclusion

In this paper, a 3D head model consisting of different head tissues was constructed to study the effects of applied potentials

TABLE 4: Total power dissipation densities and temperature increases per second of various brain tissues under an applied potential of 100 V in the electrode configuration where all electrodes were assigned potentials except the center one of the back array which was grounded.

	Total power dissipation density (W/m ³)	Temperature increase per second (°C/s)
Scalp	2.44×10^6	0.65
Skull	4.43×10^4	0.016
Dura	5.38×10^3	1.36×10^{-3}
Cerebrospinal fluid	3.52×10^3	8.53×10^{-4}
Brain	61.29	1.62×10^{-5}

and electrode configurations on the dcEF distribution inside the brain. From the simulation results, the following findings are noticeable. First, an applied potential of 100 V is able to generate dcEF strengths of 0.5~1 V/cm inside the brain. These magnitudes are suitable for GBM treatment. Second, by suitably assigning the positive and negative electrodes

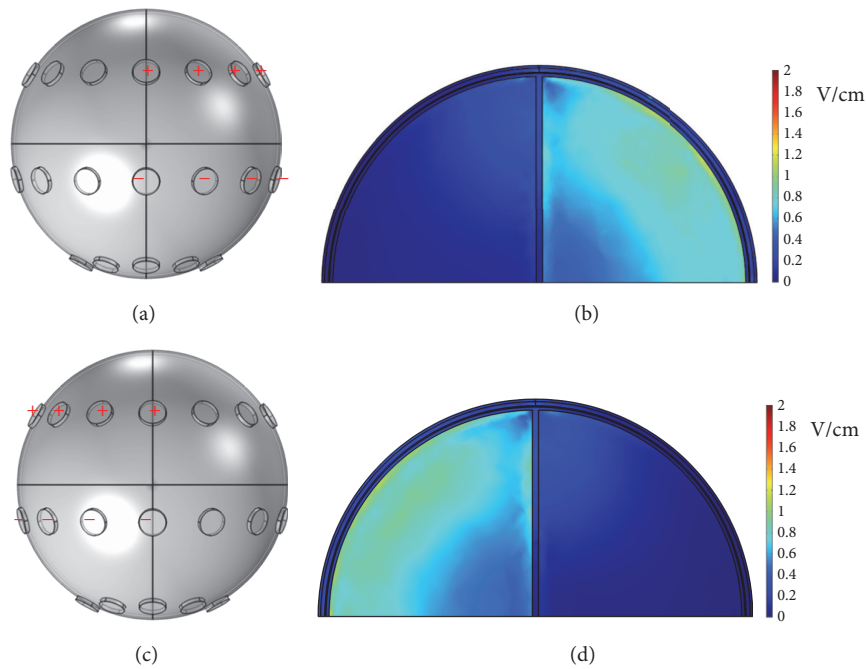


FIGURE 9: (a) The electrode configuration where the right 4 electrodes of the front array are assigned potentials and the right 4 electrodes of the middle array are grounded. (b) The x - z plane cross-sectional view ($y = 0$ mm) of the endogenous dcEF corresponding to (a). (c) The electrode configuration where the left 4 electrodes of the front array are assigned potentials and the left 4 electrodes of the middle array are grounded. (d) The x - z plane cross-sectional view ($y = 0$ mm) of the endogenous dcEF corresponding to (c).

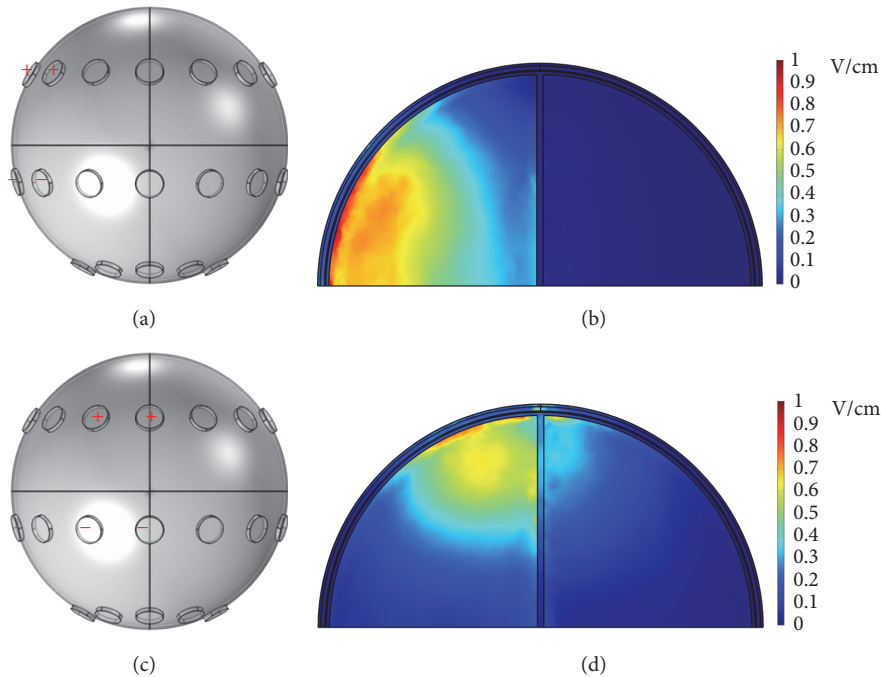


FIGURE 10: (a) The electrode configuration where the left 2 electrodes of the front array are assigned potentials and the left 2 electrodes of the middle array are grounded. (b) The x - z plane cross-sectional view ($y = 0$ mm) of the endogenous dcEF corresponding to (a). (c) The electrode configuration where the middle 2 electrodes of the front array are assigned potentials and the middle 2 electrodes of the middle array are grounded. (d) The x - z plane cross-sectional view ($y = 0$ mm) of the endogenous dcEF corresponding to (c).

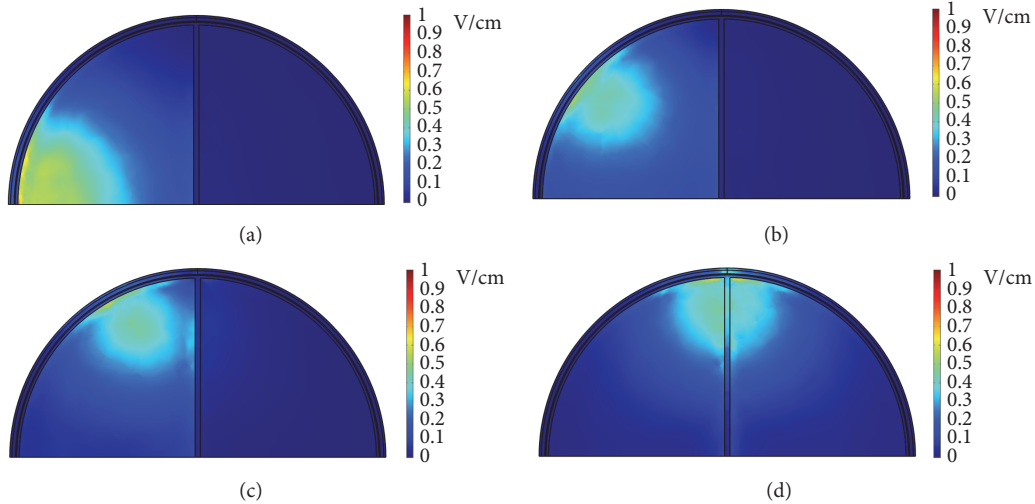


FIGURE 11: The x - z plane cross-sectional views ($y = 0$ mm) of the endogenous dcEFs corresponding to the electrode configurations where (a) the leftmost electrodes of the front and middle arrays are assigned potentials and grounded, respectively; (b) the second electrodes from the left of the front and middle arrays are assigned potentials and grounded, respectively; (c) the third electrodes from the left of the front and middle arrays are assigned potentials and grounded, respectively; (d) the center electrodes of the front and middle arrays are assigned potentials and grounded, respectively.

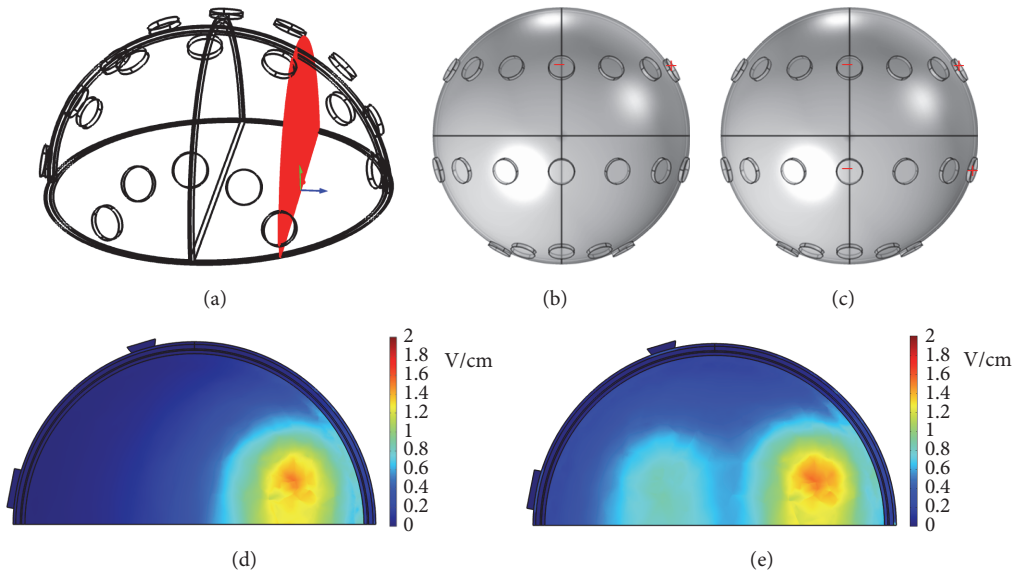


FIGURE 12: (a) The y - z plane cross-section located at $x = 25$ mm. (b) The electrode configuration where the rightmost electrode of the front array was assigned potentials and the center electrode of the front array was grounded. (c) The electrode configuration where the rightmost electrodes of the front and middle arrays were assigned potentials and the center electrodes of the front and middle arrays were grounded. (d) The dcEF distribution corresponding to the electrode configuration in (b). (e) The dcEF distribution corresponding to the electrode configuration in (c).

(numbers and relative locations), the dcEFs can be focused on specific locations. This is helpful in conducting personalized electrotherapy. Finally, under an applied voltage of 100 V, a maximum possible temperature increase per second of 0.65°C is evaluated in the scalp. Therefore, these dcEFs are thought to be harmless to the brain and all surrounding tissues. These findings are believed to be useful in designing

the electrode configuration for applications in GBM electrotherapy.

Conflicts of Interest

The author declares that there are no conflicts of interest regarding the publication of this paper.

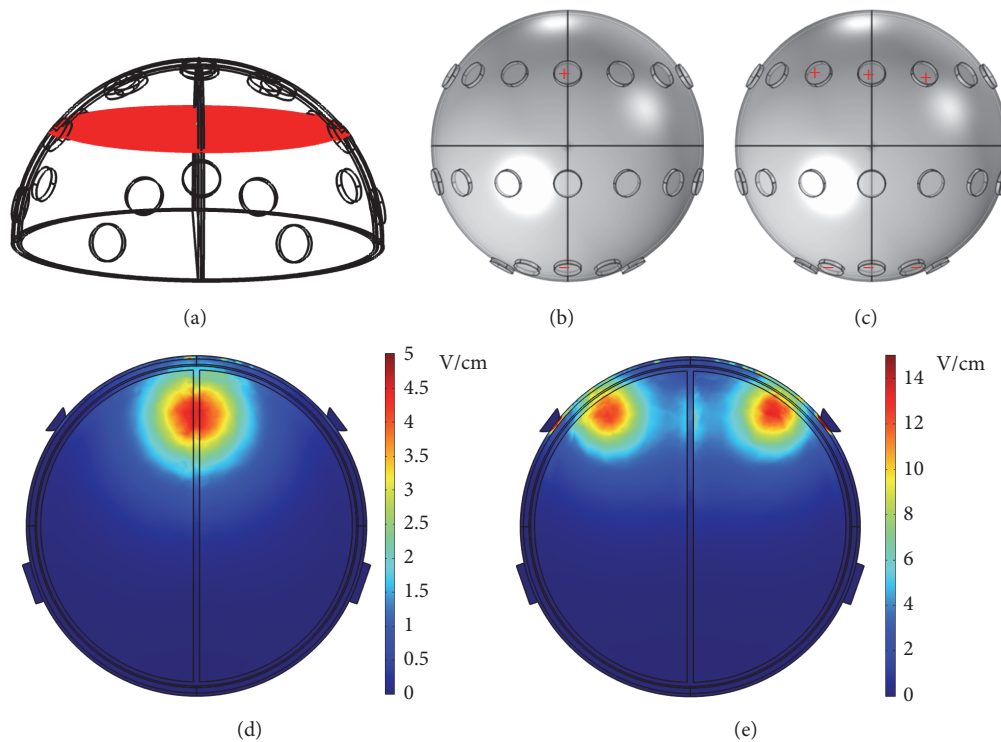


FIGURE 13: (a) The x - y plane cross-section located at $z = 33$ mm. (b) The electrode configuration where the center electrodes of the front and back arrays were assigned potentials and grounded, respectively. (c) The electrode configuration where the middle 3 electrodes of the front array were assigned potentials and the middle 3 electrodes of the back array were grounded. (d) The dcEF distribution corresponding to the electrode configuration in (b). (e) The dcEF distribution corresponding to the electrode configuration in (c).

Acknowledgments

This work was financially supported by the Ministry of Science and Technology of Taiwan under Contract nos. MOST 105-2112-M-030-002-MY2 and MOST 106-2112-M-030-001-MY2.

References

- [1] B. A. Kohler, E. Ward, B. J. McCarthy et al., "Annual report to the nation on the status of cancer, 1975–2007, featuring tumors of the brain and other nervous system," *Journal of the National Cancer Institute*, vol. 103, no. 9, pp. 714–736, 2011.
- [2] R. M. Young, A. Jamshidi, G. Davis, and J. H. Sherman, "Current trends in the surgical management and treatment of adult glioblastoma," *Annals of Translational Medicine*, vol. 3, no. 9, p. 121, 2015.
- [3] C. Gzell, M. Back, H. Wheeler, D. Bailey, and M. Foote, "Radiotherapy in Glioblastoma: the Past, the Present and the Future," *Clinical Oncology*, vol. 29, no. 1, pp. 15–25, 2017.
- [4] D. Khosla, "Concurrent therapy to enhance radiotherapeutic outcomes in glioblastoma," *Annals of Translational Medicine*, vol. 4, no. 3, p. 54, 2016.
- [5] S. Kuramitsu, A. Yamamichi, F. Ohka, K. Motomura, M. Hara, and A. Natsume, "Adoptive immunotherapy for the treatment of glioblastoma: Progress and possibilities," *Immunotherapy*, vol. 8, no. 12, pp. 1393–1404, 2016.
- [6] A. A. Thomas, M. S. Ernstoff, and C. E. Fadul, "Immunotherapy for the treatment of glioblastoma," *Cancer Journal*, vol. 18, no. 1, pp. 59–68, 2012.
- [7] A. Kwiatkowska, M. Nandhu, P. Behera, E. Chiocca, and M. Viapiano, "Strategies in Gene Therapy for Glioblastoma," *Cancers*, vol. 5, no. 4, pp. 1271–1305, 2013.
- [8] R. Stupp, W. P. Mason, M. J. van den Bent et al., "Radiotherapy plus concomitant and adjuvant temozolomide for glioblastoma," *The New England Journal of Medicine*, vol. 352, no. 10, pp. 987–996, 2005.
- [9] M. Zhao, J. V. Forrester, and C. D. McCaig, "A small, physiological electric field orients cell division," *Proceedings of the National Academy of Sciences of the United States of America*, vol. 96, no. 9, pp. 4942–4946, 1999.
- [10] R. Nuccitelli, "A role for endogenous electric fields in wound healing," *Current Topics in Developmental Biology*, vol. 58, pp. 1–26, 2003.
- [11] Y.-S. Sun, S.-W. Peng, K.-H. Lin, and J.-Y. Cheng, "Electrotaxis of lung cancer cells in ordered three-dimensional scaffolds," *Biomicrofluidics*, vol. 6, no. 1, Article ID 014102, 2012.
- [12] Y.-S. Sun, S.-W. Peng, and J.-Y. Cheng, "In vitro electrical-stimulated wound-healing chip for studying electric field-assisted wound-healing process," *Biomicrofluidics*, vol. 6, no. 3, Article ID 034117, 2012.
- [13] S.-Y. Wu, H.-S. Hou, Y.-S. Sun, J.-Y. Cheng, and K.-Y. Lo, "Correlation between cell migration and reactive oxygen species under electric field stimulation," *Biomicrofluidics*, vol. 9, no. 5, Article ID 054120, 2015.

- [14] E. D. Kirson, V. Dbalý, F. Tovaryš et al., “Alternating electric fields arrest cell proliferation in animal tumor models and human brain tumors,” *Proceedings of the National Academy of Sciences of the United States of America*, vol. 104, no. 24, pp. 10152–10157, 2007.
- [15] P. C. Miranda, A. Mekonnen, R. Salvador, and P. J. Basser, “Predicting the electric field distribution in the brain for the treatment of glioblastoma,” *Physics in Medicine and Biology*, vol. 59, no. 15, pp. 4137–4147, 2014.
- [16] E. D. Kirson, Z. Gurvich, R. Schneiderman et al., “Disruption of Cancer Cell Replication by Alternating Electric Fields,” *Cancer Research*, vol. 64, no. 9, pp. 3288–3295, 2004.
- [17] N. Gharaee, M. Habibpour, H. Sepehri, and L. Delphi, “10P Efficacy of tumor treating field therapy alone and in combination with doxorubicin in cellular model of breast cancer,” *Annals of Oncology*, vol. 27, no. suppl_9, 2016.
- [18] M. Giladi, U. Weinberg, R. S. Schneiderman et al., “Alternating electric fields (tumor-treating fields therapy) can improve chemotherapy treatment efficacy in non-small cell lung cancer both in vitro and in vivo,” *Seminars in Oncology*, vol. 41, no. 6, pp. S35–S41, 2014.
- [19] M. Munster, R. Blat, P. C. Roberts et al., “Abstract B79: Translational study of tumor treating fields in combination with paclitaxel in ovarian cancer,” *Clinical Cancer Research*, vol. 22, no. 2 Supplement, pp. B79–B79, 2016.
- [20] J. Byrne, A. O’Neill, R. Jajja et al., “Electric-field assisted delivery of gemcitabine for the treatment of pancreatic cancer,” *Cancer Research*, vol. 73, no. 8 Supplement, pp. 5610–5610, 2014.
- [21] R. Stupp, E. T. Wong, A. A. Kanner et al., “NovoTTF-100A versus physician’s choice chemotherapy in recurrent glioblastoma: A randomised phase III trial of a novel treatment modality,” *European Journal of Cancer*, vol. 48, no. 14, pp. 2192–2202, 2012.
- [22] E. T. Wong, E. Lok, and K. D. Swanson, “Clinical benefit in recurrent glioblastoma from adjuvant NovoTTF-100A and TCCC after temozolomide and bevacizumab failure: A preliminary observation,” *Cancer Medicine*, vol. 4, no. 3, pp. 383–391, 2015.
- [23] R. Stupp, “Tumor treating fields added to standard chemotherapy in newly diagnosed glioblastoma (GBM): Final results of a randomized, multi-center, phase III trial,” in *Proceedings of the AACR Annual Meeting 2017*, 2017.
- [24] K. Nowak, E. Mix, J. Gimsa et al., “Optimizing a rodent model of parkinson’s disease for exploring the effects and mechanisms of deep brain stimulation,” *Parkinson’s Disease*, vol. 2011, Article ID 414682, 19 pages, 2011.

Research Article

Simulation of Atrial Fibrosis Using Coupled Myocyte-Fibroblast Cellular and Human Atrial Models

Yuan Gao, Yinglan Gong, and Ling Xia

Key Laboratory for Biomedical Engineering of Ministry of Education, Department of Biomedical Engineering, Zhejiang University, Hangzhou 310027, China

Correspondence should be addressed to Yinglan Gong; yinglangong@zju.edu.cn and Ling Xia; xialing@zju.edu.cn

Received 3 July 2017; Revised 10 November 2017; Accepted 3 December 2017; Published 26 December 2017

Academic Editor: Marta Parazzini

Copyright © 2017 Yuan Gao et al. This is an open access article distributed under the Creative Commons Attribution License, which permits unrestricted use, distribution, and reproduction in any medium, provided the original work is properly cited.

Atrial fibrosis is characterized by expansion of extracellular matrix and increase in the number of fibroblasts which has been associated with the development and maintenance of atrial arrhythmias. However, the mechanisms how the fibrosis contributes to atrial arrhythmia remain incompletely understood. In this study, we used a proposed fibroblast model coupled with the human atrial myocyte to investigate the effects of fibrosis on atrial excitability and repolarization at both cellular and macroscopic levels. The 12-lead electrocardiogram (ECG) was also simulated to explore the index of clinical diagnosis for fibrosis. The simulation results showed that the fibrosis can modify action potential morphology of human atrial myocyte, slow down wave propagation, and have rate adaptation, thus causing the atrial electrical heterogeneity. The fibrosis alone was sufficient to cause arrhythmia, induce reentry wave, and result in low amplitude and wide P waves at normal heart rate and significant prolonged and inverse P waves at high heart rate. All these symptoms aggravated when the level of fibrosis increased. Our simulations demonstrated that fibrosis is the substrate of atrial arrhythmia and thereby may be a potential target in the treatment of atrial arrhythmias.

1. Introduction

Fibrosis is a critical aspect of cardiac dysfunction following myocardial infarction, hypertension, heart failure, and severe arrhythmia [1, 2]. It is characterized by expansion of myocardial extracellular matrix and increase in the number of cardiac fibroblasts (Fbs). It increases with age and can lead to slow propagation and contribute to unidirectional block [3]. Apart from electrical remodeling and contractile dysfunction, atrial fibrosis has been shown to increase the susceptibility to atrial fibrillation (AF) and may serve as a critical substrate in the formation of the arrhythmia [4, 5]. A study about the small mouse atria has indicated that the alterations in atrial conduction produced by atrial interstitial fibrosis alone were sufficient to produce a substrate for AF [6].

But the mechanisms by how the fibrosis contributes to atrial arrhythmia remain incompletely understood. Cardiac fibroblast was the essential cell type in heart that is responsible for the homeostasis of the extracellular matrix. But it may transform to a myofibroblast phenotype and contribute to cardiac fibrosis when under impairment [7]. Many studies have revealed that myocytes and fibroblasts are functionally

coupled by gap junctions when fibrosis occurred and may interact and modify impulse conduction via two-way electronic signal [8–10]. These results suggest a potential role for myocyte-fibroblast coupling in atrial arrhythmia.

Although there has been significant progress in the study of fibrosis over the past few decades, there still remain many unanswered questions. Investigation on human atrial myocardium with fibrosis is still very limited due to the difficulties in accessing experimental data. Therefore, alternative methods such as computer simulations are of great importance [11]. The main purpose of this study was to investigate the effects of fibrosis on atrial excitability and repolarization. To achieve this goal, we used a proposed fibroblast model [12] coupled with the Courtemanche et al. model [13] for atrial myocyte to stimulate the changes of action potential (AP) at the cellular level. At the macroscopic level, the AP models were incorporated into a human atrial model to simulate cardiac excitation conduction. Since the 12-lead ECG has been widely accepted as the main noninvasive diagnostic method of cardiac disease, we simulated the fibrosis ECG patterns to serve as an assistant method to study

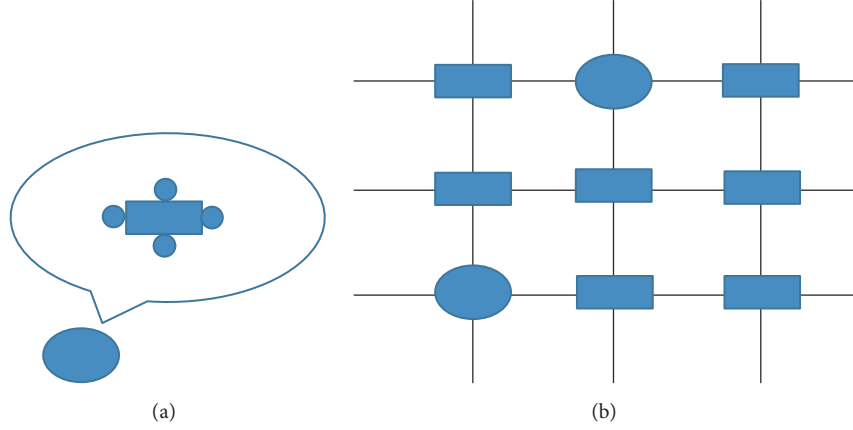


FIGURE 1: Illustration of myocyte/Fbs complex unit. The rectangle indicates a normal atrial myocyte, the ellipse indicates a myocyte/Fbs complex unit, and the circle around the myocyte indicates a fibroblast. (a) View of one myocyte/Fbs complex unit: a single human atrial myocyte is coupled a selected number of homogeneous fibroblasts via assigning an intercellular conductance (G_{gap}) [14]. In this study, the number of fibroblasts was 1 to 6. (b) Schematic representation of 2D atrial tissue: myocyte/Fbs complex unit that replaces the normal myocyte random existing in the tissue indicates the fibrosis proliferous area [15].

the underlying relationship between morphology of ECG and fibrosis atrial electrical activity.

2. Material and Methods

2.1. Myocyte-Fibroblast Electrophysiological Coupling. In our simulation, the atrial myocyte was surrounded by a selected number of fibroblasts in normal tissue, which was regarded as one myocyte/Fbs complex unit. The paradigm is illustrated in Figure 1.

The electrophysiological model of atrial myocyte is based on the Courtemanche et al. [13], which can accurately represent the atrial AP dynamics. Using specific formulations of Na^+ , K^+ , and Ca^{2+} currents based on the experimental data recorded from human atrial myocytes, along with representations of pump, exchange, and background currents, the model is computationally efficient and correctly replicates physiologically repolarization process.

The atrial fibroblast model was based on the active 1 model described by Maleckar et al. [12]. The model contains four active membrane ionic currents: time and voltage dependent K^+ current, inward-rectifying K^+ current, Na^+ - K^+ pump current, and background Na^+ current. This model originates from a previous mathematical formulation of MacCannell et al. [14] and is modified based on the experimental data to well represent human atrial fibroblast properties. The membrane potential of the coupling model is governed by the following equation:

$$\begin{aligned} \frac{dV_{\text{myo}}}{dt} &= -\frac{1}{C_{\text{myo}}} \left[I_{\text{myo}}(V_{\text{myo}}, t) + I_{\text{stim}} + \sum_{i=1:n} I_{\text{gap}} \right], \\ \frac{dV_{\text{Fb}}}{dt} &= -\frac{1}{C_{\text{Fb}}} \left[I_{\text{Fb}}(V_{\text{Fb}}, t) - I_{\text{gap}} \right], \\ I_{\text{gap}} &= G_{\text{gap}} (V_{\text{myo}} - V_{\text{Fb}}), \end{aligned} \quad (1)$$

where V_{myo} and V_{Fb} represent the membrane potential of the atrial myocyte and fibroblast, respectively, C_{myo} and C_{Fb} are the membrane capacitance of the myocyte and fibroblast, respectively, I_{myo} is the net membrane current of the myocyte, and I_{Fb} is the net membrane current of fibroblast. I_{stim} is the stimulus current applied to myocyte membrane, I_{gap} is the current that flows through the gap junction between the myocyte and each fibroblast, n is the total number of fibroblasts, and G_{gap} represents the gap junction conductance. According to the experimental reports, C_{Fb} ranges from 6.3 to 75 pF [16]; G_{gap} between a myocyte and a fibroblast ranges from 0.3 to 8 nS in cultured cells [17]. In this study, we used $C_{\text{myo}} = 100$ pF, $C_{\text{Fb}} = 6.3$ pF, and $G_{\text{gap}} = 3$ nS.

2.2. Model of 3D Atria. The atrial specimen was obtained from a healthy male adult in Zhujiang Hospital, Southern Medical University, China. The use of the heart for research purpose was approved by the local Ethics Committee of the Southern Medical University. The National Rules and Regulations on Heart research were strictly followed. The specimen was scanned by spiral computer tomography (Philips/Brilliance 64) with a resolution of 512 pixels by 512 pixels and a spatial resolution of $0.3574 \times 0.3574 \times 0.33$ mm. Details of the model were described in our previous study [18–20].

In the model, the conduction system included sinoatrial node (SAN), Bachmann's bundle (BB), crista terminalis (CT), pectinate muscles (PM), slow pathway (SP), and fast pathway (FP). In order to simulate the anisotropy, the fiber orientation of atria was contained. During the propagation, each myocardial unit has specific electrophysiological parameters associated with the action potential of the cell unit and conduction velocity.

The propagation of action potential was based on the monodomain model [21]:

$$\frac{\partial V_m}{\partial t} = \frac{1}{C_m} \left(\frac{1}{A_m} \left(\frac{\lambda}{1 + \lambda} \nabla \cdot (\sigma_i \nabla V_m) - I_{\text{ion}} + I_{\text{app}} \right) \right), \quad (2)$$

where V_m is transmembrane voltage, C_m is the membrane capacitance, A_m is surface-to-volume ratio, and we used $A_m = 1000 \text{ cm}^{-1}$ and $C_m = 1 \mu\text{F}/\text{cm}^2$ [22]. λ is the ratio of conductivity extracellular to intracellular, σ_i is cellular conductivity, and conductivity values were based on experimental data studied by Roth [23]. The transversal conductivity was set to 0.15 S/m for myocyte and CT, 0.11 S/m for PM and BB, and 0.05 S/m for SAN. The ratio for cross-axis to long-axis conductivity was set to 1:9. λ was set to 1.0. I_{ion} is the sum of ionic currents, and I_{app} is the sum of applied stimulus currents.

The equation was solved numerically using explicit Euler method based on parallel computational techniques. The simulations were performed on a cluster of networked Dawning TC4000L system. The hardware architecture is symmetric multiprocessor shared memory that contains one management node and ten computation nodes. Each computation node consisted of two Intel Xeon 5335 processors and 4 GB of shared memory. The total theoretical computing capacity can be up to 184 Gflops. We used MPI to implement the communication between nodes.

The torso model in our study was taken from the virtual male subject of the United States. The body surface potentials generated by the cardiac sources satisfy the Poisson equation with Newman boundary conditions:

$$\begin{aligned} \nabla \cdot (\sigma \nabla \Phi) &= -\nabla \cdot \mathbf{J}_s, \quad \text{in } \Omega, \\ \sigma (\nabla \Phi) \cdot \mathbf{n} &= 0, \quad \text{on } S_B, \end{aligned} \quad (3)$$

where σ is the tissue dependent conductivity tensor, Φ is the quasi static potential, \mathbf{J}_s is the density of the equivalent dipole sources, \mathbf{n} is the normal vector, S_B is the body surface, which encloses the volume conductor Ω .

Using the Green second identity,

$$\int_S (A \nabla B - B \nabla A) \cdot \mathbf{n} \, dS = \int_V (A \nabla^2 B - B \nabla^2 A) \, d\Omega \quad (4)$$

with

$$\begin{aligned} A &= \frac{1}{\mathbf{R}}, \\ B &= \sigma \Phi. \end{aligned} \quad (5)$$

The differential equation for Φ as (3) can be solved as the following integral equation:

$$\begin{aligned} \Phi(\mathbf{r}) &= \frac{1}{4\pi\sigma} \left(\int_{\Omega_h} \mathbf{J}_s \cdot \nabla \frac{1}{\mathbf{R}} \, dV \right. \\ &\quad \left. + \sum_{i=1}^m (\sigma_i^+ - \sigma_i^-) \int_{S_i} \Phi(\mathbf{r}) \nabla \frac{1}{\mathbf{R}} \, dS \right), \end{aligned} \quad (6)$$

where $\mathbf{R} = \mathbf{r} - \mathbf{r}_s$ is the vector between the field point \mathbf{r} and source point \mathbf{r}_s ; Ω_h is the heart area, S_i is the conductivity junction surface, and its inside and outside conductivities are σ_i^+ and σ_i^- , respectively. Further details of the model can be found in our previous studies [24, 25].

The 12-leads ECGs are calculated as [26]

$$\begin{aligned} \text{I} &= V_{\text{LA}} - V_{\text{RA}}, \\ \text{II} &= V_{\text{LL}} - V_{\text{RA}}, \\ \text{III} &= V_{\text{LL}} - V_{\text{LA}}, \\ \text{aVR} &= -\frac{1}{2}(\text{I} + \text{II}), \\ \text{aVL} &= \text{I} - \frac{1}{2}\text{II}, \\ \text{aVF} &= \text{II} - \frac{1}{2}\text{I}, \\ V_i &= V_{P_i} - \frac{(V_{\text{LA}} + V_{\text{RA}} + V_{\text{LL}})}{3}, \end{aligned} \quad (7)$$

where V_{LA} is left arm surface potential, V_{RA} is right arm surface potential, V_{LL} is left leg surface potential, V_i is each precordial lead ($i = 1, 2, \dots, 6$), and V_{P_i} is each precordial surface potential.

3. Results

3.1. Action Potential of Atrial Myocyte Coupling Fibroblasts. In our study, we first simulated the APs of one human atrial myocyte coupled different number of fibroblasts with a G_{gap} of 3 nS at stimulation frequencies between 1 and 3 Hz. More than 5 to 10 stimuli were applied to achieve steady state conditions.

Figure 2 shows the APs of atrial myocyte when coupled with 1, 4, and 6 fibroblasts, respectively, in comparison with the noncoupled control for pacing at 1 Hz. In Table 1, we compare typical characteristics of action potentials for the coupled myocyte. By comparison, we can see that, with more coupled fibroblasts, the maximum overshoot potential is decreased and resting potential is increased. When the number of fibroblasts increased, the membrane potential during the plateau was less depolarized, and the AP duration to 60% repolarization (APD_{60}) decreased quickly. But the 90% repolarization (APD_{90}) was prolonged with the increasing of fibroblasts.

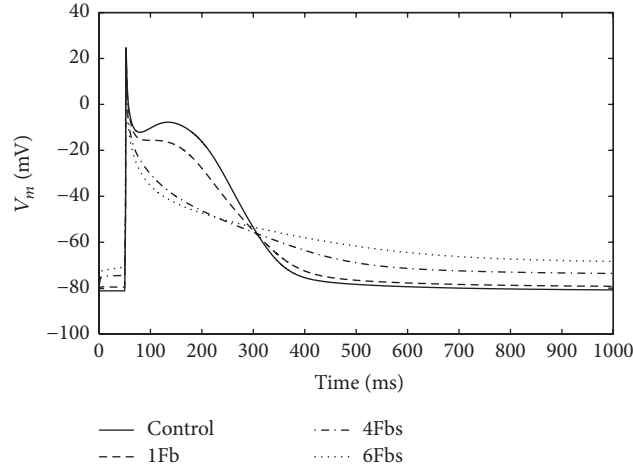
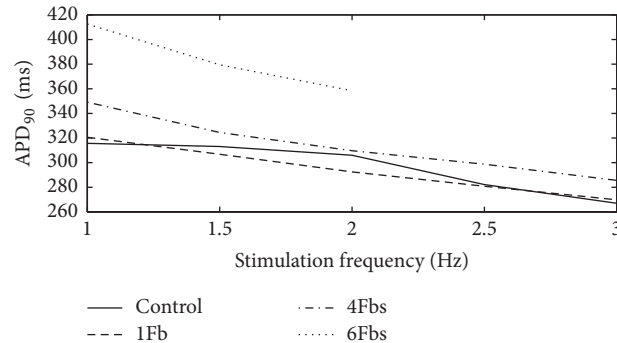
Figure 3 shows the APD_{90} of atrial myocyte coupled fibroblasts at stimulation frequencies between 1 and 3 Hz. Each of the cells displayed marked frequency dependent adaptation of the APD with a shortening at higher stimulation rates. The APD of noncoupled myocyte changed smoothly at low rates and sharply at high rates. However, the APD of coupled myocyte changed linearly with the rate increased. Remarkably, when coupled with 6 fibroblasts, the myocyte failed to achieve steady state condition at high frequency.

3.2. Simulation of 3D Atrial Exciting Sequence Map and 12-Lead ECG. Although the ratio has not been conclusive, fibrosis is characterized by the increase in the number of fibroblasts [27]. In this study, we simulated one atrial myocyte coupled 4 fibroblasts as a myocyte/Fbs complex unit. Then

TABLE 1: Characteristics for an atrial myocyte coupled Fbs with a G_{gap} of 3 nS for 1 Hz pacing.

#FB	V_{rest} (mV)	V_{max} (mV)	APD60 (ms)	APD90 (ms)
0	-81.2	24.4	230.8	315.7
1	-79.6	23.2	210.6	320.6
4	-74.1	18.1	114.0	349.1
6	-69.2	6.5	71.6	412.6

#FB indicates the number of fibroblasts coupled myocyte, V_{rest} indicates the resting potential, and V_{max} is the maximum overshoot value.

FIGURE 2: Illustration of changes in the waveform of atrial myocyte action potential when coupling to Fbs with a G_{gap} of 3 nS for 1 Hz pacing.FIGURE 3: APD₉₀ of one atrial myocyte coupled Fbs at different stimulation frequencies.

such a unit was used to randomly replace one normal myocyte in atria to simulate fibrosis. 10% and 70% of total atrial myocytes were replaced by the units to simulate gentle and severe fibrosis.

Figure 4 shows the exciting sequence map of atria with 10% and 70% fibrosis at 1 Hz pacing (i.e., the sinus rhythm was 60 beats per minute). For comparison, the exciting sequence map of normal atria was also presented. The first column of Figure 4 shows the typical normal atrial exciting sequence maps. The depolarization duration of the right atrium was 86 ms. The last part to be activated was at the site below the inferior vena cava. The total depolarization duration of the atria was 102 ms at the place of posterior left atrial wall. The second column shows the exciting sequence maps of the atria with 10% fibrosis. The right atrial depolarization duration was

90 ms and the total depolarization duration was 106 ms. The last activated areas were nearly the same as the normal case. The third column was the exciting sequence maps of the atria with 70% fibrosis. The last place to be activated in the right atrium was the right lateral wall at the time of 104 ms. The total depolarization duration of the atria was 133 ms nearly at the same place as the normal case.

Figure 5 shows the 12-lead ECG of atrium with 10% and 70% fibrosis in comparison with normal atria at 1 Hz pacing in two cardiac cycles. Because the fibrosis decreased the cellular maximum overshoot potential and reduced the atrial electrical excitation, this led to the smaller amplitude of P wave on each lead. As the fibrosis prolonged the atrial excitation time, the P wave duration was extended. The phenomenon has an increasing trend with the fibrosis degree

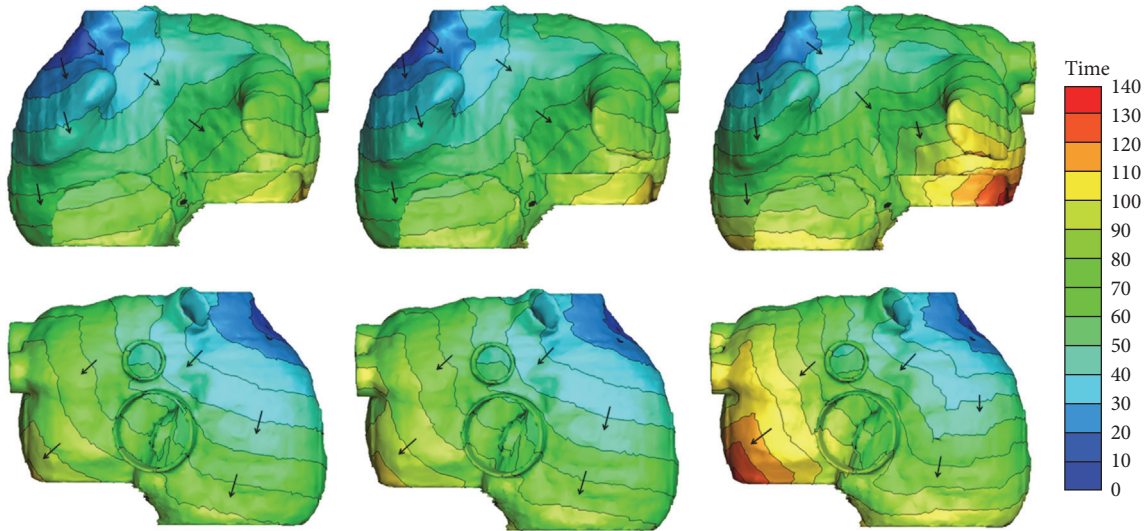


FIGURE 4: Simulated activation sequences at 1 Hz pacing. First column: normal atria; second column: atria with 10% fibrosis; third column: atria with 70% fibrosis. The first row is the anterior view of the atria; the second row is the posterior view of atria. The arrows indicate the direction of the wave propagation. The color bar on the right-hand side indicates the propagation time with the units in milliseconds.

growing. Since the time of atrial repolarization was sufficient, ECG patterns in the second cycle did not significantly change.

Figure 6 shows the exciting sequence map of atria with 10% and 70% fibrosis at 3 Hz pacing in three cardiac cycles. The first cycle of the excitation patterns was the same as Figure 4. The conduction pattern of atria with 10% fibrosis within the second cycle was slightly different. Since the repolarization of atrial myocytes near the proximal ends of conductive bundles was not sufficient, the excitation potential was far below the normal level. This led to the slow excitation propagation in the atria and slightly changed the exciting sequence. So the early part of P wave was gentle and an obvious wide P wave was visible on each lead (see Figure 7). The conduction pattern of atria with 10% fibrosis in the third cycle was more unusual. A quick exciting wave was initiated at the right posterior wall propagating around inferior vena cava from right atrium to the left atrium and merged with the planner wave propagated from the left atrial roof. It also propagated retrograde to the right lateral wall and merged with the wave propagated from the right anterior wall. This led to the notches of P waves appearing on most leads and inverse P wave on lead I.

As the fibrosis level increased to 70%, the myocytes near the sinoatrial node failed to be activated in the second cycle. The first exciting area was the right posterior wall below the inferior vena cava, initiating the reentry wave meandered in both the left atrium and the right atrium. The total activating time persisted nearly the whole cardiac cycle and merged with the next cycle. So the prolonged and inverse P waves were more significant in the ECG patterns.

4. Discussions

In this study, based on a coupled myocyte-fibroblast model, we investigated the effects of fibrosis on human atria at both

cellular and macroscopic level. At the cellular level, the AP morphology of the atrial myocyte is modified remarkably during depolarization and repolarization. With the number of coupled fibroblasts increasing, the resting membrane potential elevated and leads to weakened excitability along with the maximum overshoot potential decreased. Curtailment of 60% repolarization was seen and plateau of the AP disappeared depending on the increased number of coupled fibroblasts. However, the APD_{90} was prolonged with the increasing of fibroblasts. The atrial myocyte also displayed marked frequency dependent on the APD with a shortening at higher stimulation rate.

At the macroscopic level, the fibrosis changed the exciting wave pattern in the atria. When the sinus rhythm was normal, the velocity of wave propagation slowed down with the increased level of fibrosis, leading to the total duration of atrial depolarization and repolarization being prolonged. This resulted in the smaller amplitude and wider P wave on each lead. Since the time of atrial repolarization was sufficient, the excitation and ECG patterns at each cardiac cycle did not have obvious change. With the heart rate increasing, the electrical anomalous conduction in the atria was more obvious. Local electrical conduction block and reentry waves were initiated and meandered in both the right atrium and the left atrium. Notches of P waves appeared on most leads; significant prolonged and inverse P waves were observed. The reduced amplitude and prolonged duration of P waves have been observed in previous ECG recordings of animal and human with atrial fibrosis [28–31]. But there was no report about inverse P wave in patient with atrial fibrosis. However, this morphology has been shown to be common in patients with AF [32–35]. Notably, other morphologies of P waves in our simulation (e.g., wide duration and notches) also can be seen in these patients. This suggested the possibility that patients with atrial fibrosis can show similar ECG patterns characterized by AF.

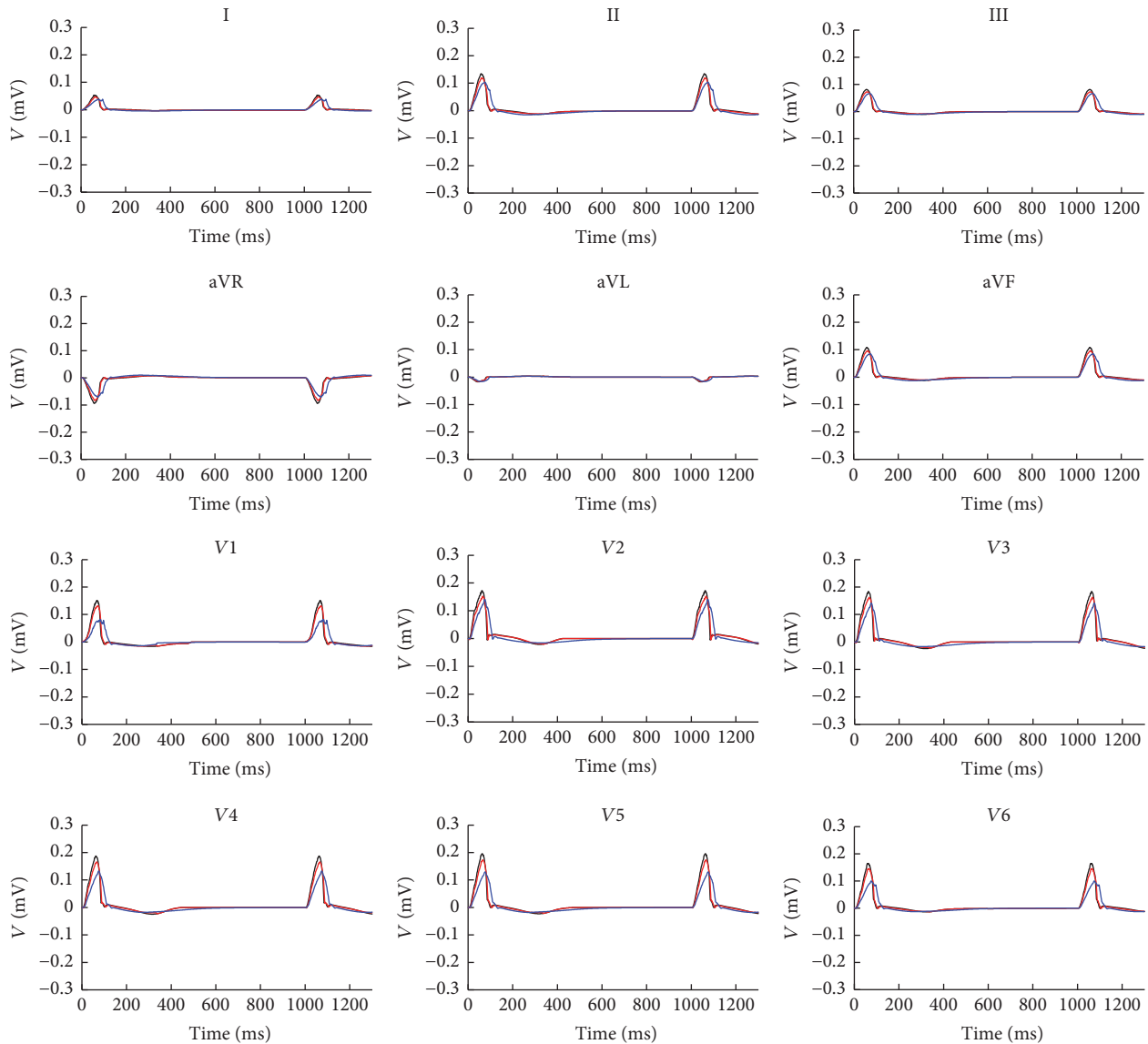


FIGURE 5: 12-lead ECG at 1 Hz in two cycles. The black lines are the normal case, red lines are atria with 10% fibrosis, and blue lines are the atria with 70% fibrosis.

Since atrial fibrosis is associated with a variety of cardiomyopathies and one of the main factors determining the relapse after therapies, the evaluating of existence and level of atrial fibrosis in atria has increasing importance for therapy strategies [5]. Nowadays late gadolinium-enhanced MRI (LGE-MRI) is the mainstream technique for detecting fibrosis [36]. But the image quality of LGE-MRI scans is frequently poor due to various reasons (e.g., residual respiratory motion, heart rate variability, low resolution limited by the thinness of atrial wall, and confounded enhancement from surrounding heart substructures). These caused a large number of false positives in the atrial fibrosis delineation. ECG may serve as a clinical method to guide the LGE-MRI evaluation. This could have implications for treatment as well as future clinical trials. Our simulations provide a promising

starting point for assessing patients with atrial fibrosis by ECG, and this could provide some references for clinical diagnosis.

It should be point out that there are still some limitations in this study. In our simulation, the atrial fibrosis model was constructed by uniformly random distributed fibrosis but not patient-derived. At the macroscopic level, we only considered the percentage increasing to represent the enhancement of fibrotic level, and the different number of coupled fibroblasts was not taken into account. Finally, the model used in this study was a static heart model with electrophysiological properties, but the mechanical functions have not been considered. Cardiac motion should be considered in future studies to further improve the simulation accuracy.

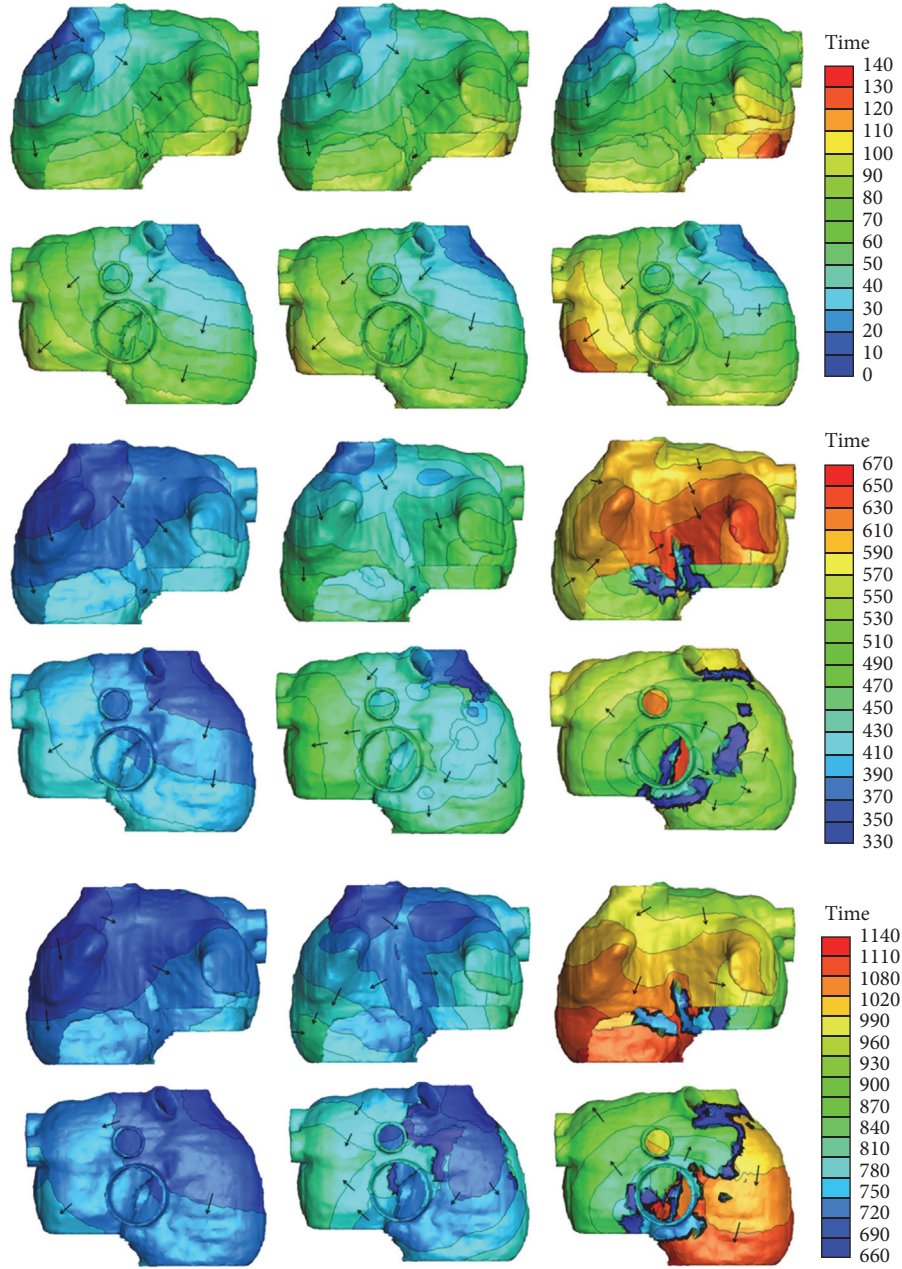


FIGURE 6: Simulated activation sequences at 3 Hz pacing. First column: normal atria; second column: atria with 10% fibrosis; third column: atria with 70% fibrosis. First two rows: anterior and posterior view of first cardiac cycle. Since the total activation duration is less than 133 ms, time window of the beginning 140 ms was given. Middle two rows: anterior and posterior view of second cardiac cycle. Last two rows: anterior and posterior view of third cardiac cycle. The arrows indicate the direction of the wave propagation. The color bars on the right-hand side indicate the propagation time with the units in milliseconds.

5. Conclusions

In this study, a coupled myocyte-fibroblast model has been used to investigate the effects of atrial fibrosis at cellular and human atrial levels. The 12-lead ECG was also simulated to explore the index of clinical diagnosis of fibrosis. The results show that the fibrosis can modify AP morphology of human atrial myocyte, slow down wave propagation, and have rate adaptation. These caused the atrial electrical heterogeneity.

The fibrosis alone was sufficient to cause arrhythmia, induce reentry wave, and result in low amplitude and wide P waves at normal heart rate and significant prolonged and inverse P waves at high heart rate. These symptoms will aggravate with the level of fibrosis increased. Our simulations demonstrated that fibrosis is the substrate of atrial arrhythmia and thereby may be a potential target in treatment of atrial arrhythmia. The understanding of the ECG changes could provide some references for clinical diagnosis.

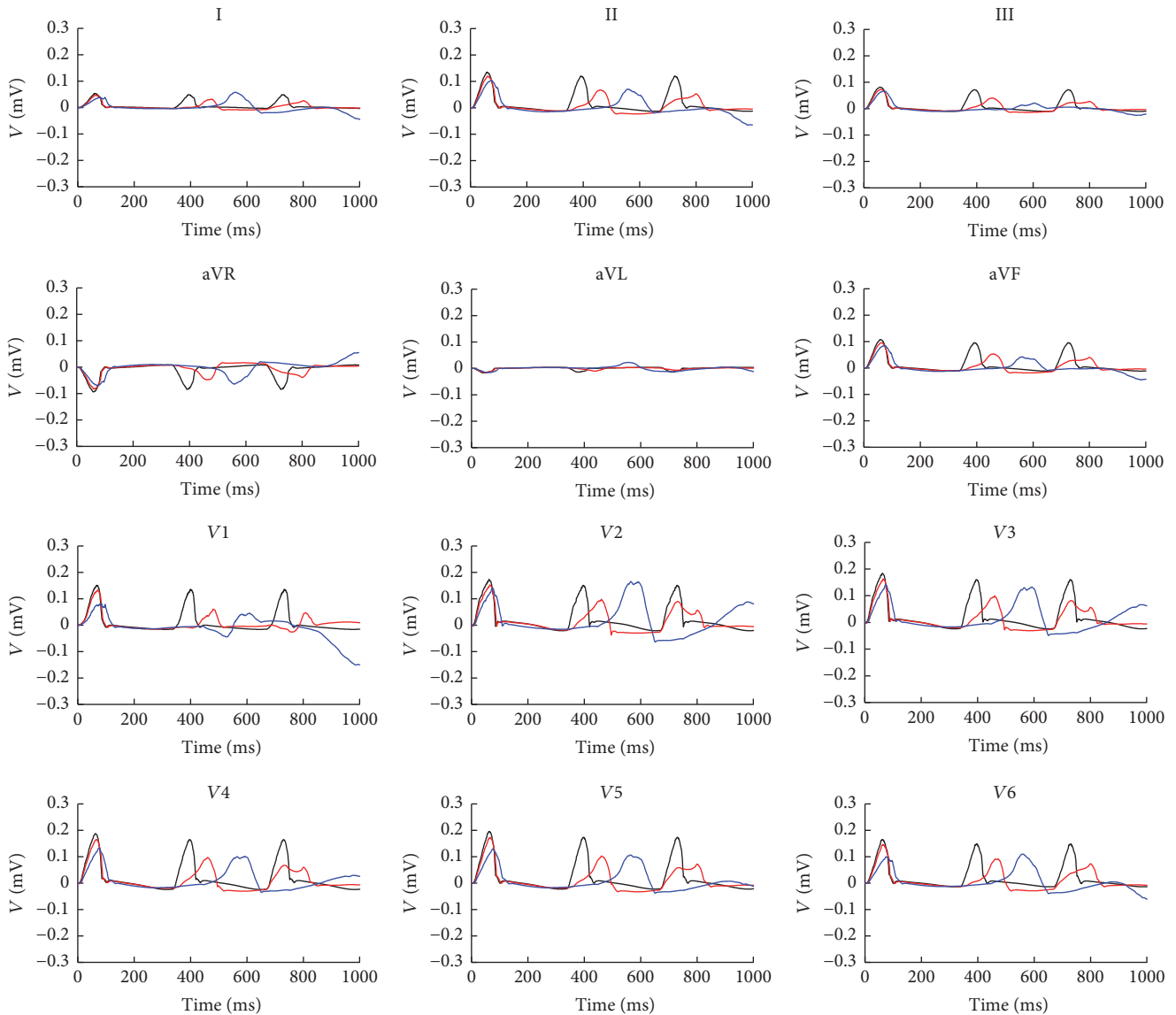


FIGURE 7: 12-lead ECG at 3 Hz in three cycles. The black lines are the normal case, red lines are atria with 10% fibrosis, and blue lines are the atria with 70% fibrosis.

Conflicts of Interest

The authors declare that there are no conflicts of interest regarding the publication of this paper.

Acknowledgments

This work was supported by the National R&D Program for Major Research Instruments (Grant no. 61527811), the National Natural Science Foundation of China (Grant no. 61701435), and the Zhejiang Provincial Natural Science Foundation of China (LY17H180003).

References

- [1] A. Piek, R. A. de Boer, and H. H. W. Silljé, "The fibrosis-cell death axis in heart failure," *Heart Failure Reviews*, vol. 21, no. 2, pp. 199–211, 2016.
- [2] S. D. Prabhu and N. G. Frangogiannis, "The biological basis for cardiac repair after myocardial infarction: from inflammation to fibrosis," *Circulation Research*, vol. 119, no. 1, pp. 91–112, 2016.
- [3] B. J. Hansen, J. Zhao, T. A. Csepe et al., "Atrial fibrillation driven by micro-anatomic intramural re-entry revealed by simultaneous sub-epicardial and sub-endocardial optical mapping in explanted human hearts," *European Heart Journal*, vol. 36, no. 35, pp. 2390–2401, 2015.
- [4] H. Cochet, A. Mouries, H. Nivet et al., "Age, atrial fibrillation, and structural heart disease are the main determinants of left atrial fibrosis detected by delayed-enhanced magnetic resonance imaging in a general cardiology population," *Journal of Cardiovascular Electrophysiology*, vol. 26, no. 5, pp. 484–492, 2015.
- [5] N. F. Marrouche, D. Wilber, G. Hindricks et al., "Association of atrial tissue fibrosis identified by delayed enhancement MRI and atrial fibrillation catheter ablation: the DECAAF Study," *Journal*

- of the American Medical Association, vol. 311, no. 5, pp. 498–506, 2014.
- [6] S. Verheule, T. Sato, T. Everett et al., “Increased vulnerability to atrial fibrillation in transgenic mice with selective atrial fibrosis caused by overexpression of TGF- β 1,” *Circulation Research*, vol. 94, no. 11, pp. 1458–1465, 2004.
 - [7] V. Nagpal, R. Rai, A. T. Place et al., “Response to letter regarding article, “MiR-125b is critical for fibroblast-to-myofibroblast transition and cardiac fibrosis,”,” *Circulation*, vol. 133, no. 24, pp. e714–e714, 2016.
 - [8] J. Pellman, J. Zhang, and F. Sheikh, “Myocyte-fibroblast communication in cardiac fibrosis and arrhythmias: mechanisms and model systems,” *Journal of Molecular and Cellular Cardiology*, vol. 94, pp. 22–31, 2016.
 - [9] S. L. K. Bowers and T. A. Baudino, “Cardiac myocyte-fibroblast interactions and the coronary vasculature,” *Journal of Cardiovascular Translational Research*, vol. 5, no. 6, pp. 783–793, 2012.
 - [10] M. Miragoli, G. Gaudesius, and S. Rohr, “Electrotonic modulation of cardiac impulse conduction by myofibroblasts,” *Circulation Research*, vol. 98, no. 6, pp. 801–810, 2006.
 - [11] S. Zahid, H. Cochet, P. M. Boyle et al., “Patient-derived models link re-entrant driver localization in atrial fibrillation to fibrosis spatial pattern,” *Cardiovascular Research*, vol. 110, no. 3, pp. 443–454, 2016.
 - [12] M. M. Maleckar, J. L. Greenstein, W. R. Giles, and N. A. Trayanova, “Electrotonic coupling between human atrial myocytes and fibroblasts alters myocyte excitability and repolarization,” *Biophysical Journal*, vol. 97, no. 8, pp. 2179–2190, 2009.
 - [13] M. Courtemanche, R. J. Ramirez, and S. Nattel, “Ionic mechanisms underlying human atrial action potential properties: insights from a mathematical model,” *American Journal of Physiology-Heart and Circulatory Physiology*, vol. 275, no. 1, pp. 301–321, 1998.
 - [14] K. A. MacCannell, H. Bazzazi, L. Chilton, Y. Shibukawa, R. B. Clark, and W. R. Giles, “A mathematical model of electrotonic interactions between ventricular myocytes and fibroblasts,” *Biophysical Journal*, vol. 92, no. 11, pp. 4121–4132, 2007.
 - [15] H. Zhan and L. Xia, “Excitation-contraction coupling between human atrial myocytes with fibroblasts and stretch activated channel current: a simulation study,” *Computational and Mathematical Methods in Medicine*, vol. 2013, no. 3, Article ID 238676, 9 pages, 2013.
 - [16] C. Vasquez, A. P. Moreno, and E. J. Berbari, “Modeling fibroblast-mediated conduction in the ventricle,” *Computers in Cardiology*, pp. 349–352, 2004.
 - [17] M. B. Rook, A. C. G. Van Ginneken, B. de Jonge, A. El Aoumari, D. Gros, and H. J. Jongsma, “Differences in gap junction channels between cardiac myocytes, fibroblasts, and heterologous pairs,” *American Journal of Physiology-Cell Physiology*, vol. 263, no. 5, pp. C959–C977, 1992.
 - [18] L. Xia, Y. Gao, Q. Lu, D. Zheng, D. D. Deng, and L. Xia, “Preliminary simulation study of atrial fibrillation treatment procedure based on a detailed human atrial model,” *Journal of Clinical Trials in Cardiology*, vol. 2, no. 4, pp. 1–9, 2015.
 - [19] D.-D. Deng, Y.-L. Gong, G.-F. Shou et al., “Simulation of biatrial conduction via different pathways during sinus rhythm with a detailed human atrial model,” *Journal of Zhejiang University Science B*, vol. 13, no. 9, pp. 676–694, 2012.
 - [20] D. Deng, P. Jiao, X. Ye, and L. Xia, “An image-based model of the whole human heart with detailed anatomical structure and fiber orientation,” *Computational and Mathematical Methods in Medicine*, vol. 2012, no. 3, Article ID 891070, pp. 449–461, 2012.
 - [21] Y. Zhang, L. Xia, Y. Gong, L. Chen, G. Hou, and M. Tang, “Parallel solution in simulation of cardiac excitation anisotropic propagation,” in *International Conference on Functional Imaging and Modeling of the Heart*, Lecture Notes in Computer Science, pp. 170–179, 2007.
 - [22] M. Potse, B. Dubé, A. Vinet, and R. Cardinal, “A comparison of monodomain and bidomain propagation models for the human heart,” in *Proceedings of the 28th Annual International Conference of the IEEE Engineering in Medicine and Biology Society, (EMBS '06)*, pp. 3895–3898, New York, NY, USA, September 2006.
 - [23] B. J. Roth, “Electrical conductivity values used with the bidomain model of cardiac tissue,” *IEEE Transactions on Biomedical Engineering*, vol. 44, no. 4, pp. 326–328, 1997.
 - [24] L. Xia, M. Huo, Q. Wei, F. Liu, and S. Crozier, “Electrodynamic heart model construction and ECG simulation,” *Methods of Information in Medicine*, vol. 45, no. 5, pp. 564–573, 2006.
 - [25] G. Shou, L. Xia, M. Jiang, F. Liu, and S. Crozier, “Forward and inverse solutions of electrocardiography problem using an adaptive BEM method,” *International Conference on Functional Imaging and Modeling of the Heart*, pp. 290–299, 2007.
 - [26] P. Kligfield, L. S. Gettes, J. J. Bailey et al., “Recommendations for the standardization and interpretation of the electrocardiogram,” *Heart Rhythm the Official Journal of the Heart Rhythm Society*, vol. 115, no. 10, pp. 1306–1324, 2007.
 - [27] P. Camelliti, T. K. Borg, and P. Kohl, “Structural and functional characterisation of cardiac fibroblasts,” *Cardiovascular Research*, vol. 65, no. 1, pp. 40–51, 2005.
 - [28] S. Verheule, T. Sat, T. IV. Everett et al., “Increased vulnerability to atrial fibrillation in transgenic mice with selective atrial fibrosis caused by overexpression of TGF- β 1,” *Circulation Research*, vol. 94, no. 11, pp. 1458–1465, 2004.
 - [29] F. Zhang, M. Tang, W. Wang, L. Chen, and D. O. Cardiology, “The effect of spironolactone on spontaneous hypertensive rat’s left atrial fibrosis and its atrial vulnerability,” *Journal of Clinical Cardiology*, 2015.
 - [30] T. T. Win, B. A. Venkatesh, G. J. Volpe et al., “Associations of electrocardiographic P-wave characteristics with left atrial function, and diffuse left ventricular fibrosis defined by cardiac magnetic resonance: the PRIMERI study,” *Heart Rhythm*, vol. 12, no. 1, pp. 155–162, 2015.
 - [31] A. Maheshwari, F. L. Norby, E. Z. Soliman et al., “Relation of prolonged p-wave duration to risk of sudden cardiac death in the general population (from the Atherosclerosis risk in communities study),” *American Journal of Cardiology*, vol. 119, no. 9, pp. 1302–1306, 2017.
 - [32] S. Rosenheck, “Signal-averaged P wave in patients with paroxysmal atrial fibrillation,” *Pacing and Clinical Electrophysiology Pace*, vol. 20, no. 10, pp. 2577–2586, 1997.
 - [33] P. G. Platonov, J. Carlson, M. P. Ingemansson et al., “Detection of inter-atrial conduction defects with unfiltered signal-averaged P-wave ECG in patients with lone atrial fibrillation,” *Europace: European Pacing, Arrhythmias, and Cardiac Electrophysiology*, vol. 2, no. 1, pp. 32–41, 2000.
 - [34] J. Carlson, R. Johansson, and S. Olsson, “Classification of electrocardiographic P-wave morphology,” in *Proceedings of the 39th IEEE Conference on Decision and Control*, pp. 1804–1809, Sydney, NSW, Australia.

- [35] F. Sadiq Ali, A. Enriquez, D. Redfearn, and A. Baranchuk, "P-wave pseudonormalization after iatrogenic coronary sinus isolation," *Journal of Electrocardiology*, vol. 49, no. 1, pp. 13-14, 2016.
- [36] P. Kellman and A. E. Arai, "Cardiac imaging techniques for physicians: late enhancement," *Journal of Magnetic Resonance Imaging*, vol. 36, no. 3, pp. 529-542, 2012.

Research Article

Computational FEM Model, *Phantom* and *Ex Vivo* Swine Breast Validation of an Optimized Double-Slot Microcoaxial Antenna Designed for Minimally Invasive Breast Tumor Ablation: Theoretical and Experimental Comparison of Temperature, Size of Lesion, and SWR, Preliminary Data

Geshel David Guerrero López,¹ Mario Francisco Jesús Cepeda Rubio,¹
José Irving Hernández Jácquez,¹ Arturo Vera Hernandez,² Lorenzo Leija Salas,²
Francisco Valdés Perezgasga,¹ and Francisco Flores García¹

¹*División de Estudios de Posgrado e Investigación, Tecnológico Nacional de México, Instituto Tecnológico de la Laguna, Blvd. Revolución, Esq. Calzad. Instituto Tecnológico de la Laguna, Zona Centro, 27000 Torreón, COAH, Mexico*

²*Sección de Bioelectrónica, Centro de Investigación y de Estudios Avanzados del Instituto Politécnico Nacional, Ciudad de México, Mexico*

Correspondence should be addressed to José Irving Hernández Jácquez; jihernandezj@correo.itlalaguna.edu.mx

Received 13 June 2017; Revised 17 August 2017; Accepted 29 October 2017; Published 10 December 2017

Academic Editor: Marta Parazzini

Copyright © 2017 Geshel David Guerrero López et al. This is an open access article distributed under the Creative Commons Attribution License, which permits unrestricted use, distribution, and reproduction in any medium, provided the original work is properly cited.

Malignant neoplasms are one of the principal world health concerns and breast cancer is the most common type of cancer in women. Advances in cancer detection technologies allow treating it in early stages; however, it is necessary to develop treatments which carry fewer complications and aesthetic repercussions. This work presents a feasibility study for the use of microwave ablation as a novel technique for breast cancer treatment. A microwave applicator design is also being proposed for this purpose. The coupling of the designed antenna was predicted with computer simulation. The standing wave ratio obtained through simulation was 1.87 and the result of experimental validation was 1.04. The optimized antenna has an optimal coupling (SWR = 1.04) so ablation temperatures can be achieved in a relatively short time using low power. Varying the time and power, the heating pattern can be changed to treat different tumors. However, as some discrepancies are still present, a deeper study of the dielectric properties and their variation with temperature is required.

1. Introduction

The most frequent reported types of cancer worldwide (ordered by number of deaths) are lung, stomach, liver, colon-rectum, esophagus, and prostate, in the case of males, and breast, lung, stomach, colon-rectum, and cervix, in the case of females. Breast cancer is one of the most common types of cancer in women [1, 2], so we have focused our research on its minimally invasive treatment. Surgery is the conventional treatment for this type of cancer [3].

The present work proposes a new technique for its minimally invasive treatment by using microwave ablation (MWA). Ablation using microwave energy is an encouraging method because it can heat breast carcinoma (high water content tissue) more than adipose or breast glandular healthy tissue (low water content tissue); additionally, it can be used to treat patients that are not candidates for surgery like anesthetic risk. MWA presents advantages over other therapies [4–6] which make it more attractive to treat breast tumors; however, it is important to mention that to the best

of our knowledge there is only one reported clinical trial of breast cancer treatment that uses MWA in literature [7]. Some of the benefits of MWA are an improved convection profile, higher constant intratumoral temperatures, faster ablation times, and the possibility of using multiple probes to treat multiple lesions simultaneously. In addition, the placement of grounding pads is not necessary; this reduces the risk of skin burns. Another advantage is that MWA creates larger ablation zones than other treatments with similar sized applicators [8]. Finally, the size and shape of the MWA zone may be more consistent and less dependent on the heat-sink effect from vascular structures in proximity of the lesion [9, 10].

Due to the increase in the use of mammography, the detection of breast cancer in initial stages has increased and this facilitates its treatment with noninvasive and minimally invasive techniques. These techniques are related to ablation technologies that can be classified as radio frequency ablation (RFA), MWA, laser photocoagulation, ultrasound ablation, and cryotherapy [11]. These treatments are a good alternative for patients who cannot be treated surgically.

MWA responds to the lower heating of adipose and glandular tissue compared to the heating of the breast carcinoma because of its higher water content [12]. The MWA occurs because of the movement of polar molecules in the tissue. Molecules try to align with the electric field generated and since the polarity of this field changes millions of times per second, they are constantly vibrating. This movement produces friction and the friction results in tissue heating. The aim of MWA is the complete destruction of the cancer tissue and a safety margin of surrounding healthy tissue. The thermal destruction of tissue depends on the maximum temperature reached and the time of exposition; there are experimental studies supporting that 60 minutes at 43°C is tumoricidal, and the period of time required to kill tumor cells is halved for every degree increased above 43°C [13, 14]. In this work, 55°C isothermal contour was considered as ablation zone, since time needed to damage cells at this temperature is less than one minute [15]. A great variety of applicators have been proposed for their use in MWA; most of them are based on a coaxial structure. The coaxial applicator designs include the monopole, the dipole, and the slot applicators; they are usually covered with a polytetrafluoroethylene (PTFE) catheter in order to minimize the adhesion of the applicator to the ablation exposed (carbonized) tissue. A wide review of these applicators can be found in [16], although none of them have been applied to breast cancer treatment.

The dipole antenna is usually constructed with semirigid coaxial cable; for its design, three important regions should be considered. The first region is the distal tip of the antenna (usually referred to as extension) which is a metal segment of a specific length. The second region is a slot (commonly referred to as gap or junction) that acts as the effective source of electromagnetic wave propagation. Finally, the last region is the insertion depth of the antenna with a variable length. The dipole is an applicator of easy construction; however, the lesion produced by this antenna is highly dependent on the insertion depth.

The monopole is an applicator constructed with a semirigid coaxial cable in which the outer conductor is removed in

order to leave an elongated inner conductor which is radially surrounded by dielectric materials. There are some variations of the monopole applicator, which depend on the finishing of the tip.

Finally, the slot antenna is one of the most popular designs for MWA. This is constructed by cutting a small ring slot in the outer conductor of a thin semirigid coaxial cable, and then the outer and inner conductor are short-circuited in the distal tip of the antenna. Some of the factors that modify the radiation pattern of this type of applicator are the width of the slot, the dielectric media surrounding the distal tip, and the length from the slot to the tip.

Since doing experimental validation for all these types of applicators is an extensive task, it turns useful to make use of computational models to face this problem. A numerical approach is an excellent way to solve complicated physical problems, considering that present hardware is not that expensive and it is powerful enough; thanks to this more researchers are using computational models to solve electromagnetic problems and component designs. There are several numerical approaches like Finite Difference Method that use finite differences to approximate the derivatives or the Finite Element Method (FEM) that subdivides a larger problem into smaller, simple parts, with a simple equation that models it. These equations are then assembled into a large system to model the entire problem.

There are several commercial software programs that use FEM like COMSOL, Abaqus, ANSYS, and SolidWorks. Among these software programs, the COMSOL uses electromagnetics and thermal libraries that permit the user to solve multiphysics problems making it possible to simulate the electromagnetic effect of the applicator and the thermal lesion produced in a single computation, which is the reason why it is used for this investigation.

In this work, an optimized double-slot antenna was constructed and computing modelled to be used in MWA therapy for breast cancer. The antenna was modelled by using the Finite Element Method and the Maxwell and bioheat equations. Then, the antenna was constructed by using a micro coaxial cable which was modified in order to have two slots. In both cases, the temperature distribution and the Standing Wave Ratio (SWR) were obtained. Experiments were carried out in breast mimicking phantom and *ex vivo* swine breast. The SWR and temperature distribution were compared in order to determine the feasibility of using this novel technique in breast cancer treatment.

2. Materials and Methods

2.1. Applicator Design. The applicator proposed here consisted of a micro coaxial cable with two 1mm wide slots situated in the distal part of the antenna. The diameter of the applicator was approximately 2.2mm; the outer conductor was made of copper; the dielectric was low loss PTFE and the inner conductor was silver plated copper wire (SPWC). Table 1 shows dimension details and thermal properties of the antenna and of the breast tissue.

The geometrical parameters of the antenna were selected considering the effective wavelength in tumor tissue at

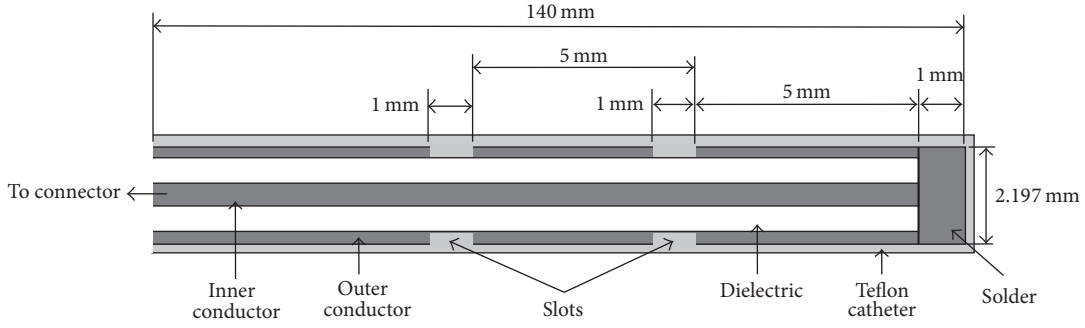


FIGURE 1: Axial view of the dimensions of the double-slot antenna used for MWA. The two 1 mm slots were separated by 5 mm; the total length of the applicator was 140 mm.

TABLE 1: Dimensions and properties of the materials used for the FEM modelling of the double-slot microcoaxial antenna.

Parameter	Value	Reference
Central conductor diameter	0.51 ± 0.0127 mm	[17]
Dielectric diameter	1.68 ± 0.0254 mm	[17]
External conductor diameter	2.197 ± 0.0254 mm	[17]
Catheter diameter	2.64 ± 0.03 mm	—
Material	Relative permittivity	Reference
Coaxial cable internal dielectric	2.03	[18]
Catheter	2.60	[16]

2.45 GHz (this frequency was selected considering that it belongs to ISM band and it is available worldwide). The wavelength was calculated by using the following equation:

$$\lambda_{\text{eff}} = \frac{c}{f \sqrt{\epsilon_r \mu_r}}, \quad (1)$$

where c represents the speed of light in free space (in m/s), f represents operating frequency of the generator (2.45 GHz), ϵ_r represents the relative permittivity of the tumor at operating frequency (59.385), and μ_r represents the magnetic relative permeability (1). The calculated wavelength for these values was 15.88 mm; however, since the tissue was heterogeneous, this value was used only as a reference.

The applicator geometry is shown in Figure 1. Notice that the distance between the first slot and the tip and the distance between both slots are approximately $0.25\lambda_{\text{eff}}$.

2.2. The Finite Element Method. Many researchers have used mathematical models based on computer electromagnetics models for the applicator design. These methods are focused on the solution of electromagnetic fundamental equations like the Maxwell equations. There are three primary computer electromagnetics models: Finite Difference Method, Method of Moments, and FEM. The FEM can rapidly provide the users with solutions to multiple differential equations systems and therefore it satisfies the heat-transfer problems [19]. Moreover, it is a numerical technique that can be formulated as functional minimization. FEM involves dividing a complex geometry into small elements for a system of partial differential equations, evaluated at nodes or edges. The method is the formulation of solutions to the fundamental electromagnetic equations, known as Maxwell equations. However,

in order to develop accurate models of the ablation process, the knowledge of tissue electromagnetic properties, like permittivity and conductivity and appropriate initial and boundary conditions, must be known.

2.3. Computer Model Definition. The simulations were carried out by using COMSOL Multiphysics™ 4.4 software (Comsol Inc., Burlington, MA). Since the model had an axial symmetry, a 2D axisymmetric model was used to minimize computing time. It was assumed for the model that the antenna was introduced into the neoplasm surrounded by breast tissue. The vertical axis was oriented along the longitudinal axis of the antenna and the horizontal axis was oriented along the radial direction as shown in Figure 2.

The boundary conditions for the electromagnetic simulation are scattering boundary condition for the exterior boundaries, with the z -axis as axial symmetry; for the thermal simulation the boundary conditions are all exterior constant temperature (25°C) with the z -axis as axial symmetry. Finite Element Method (FEM) has been used to simulate the performance of microwave coaxial antennas. Linear solver performed FEM model constructing two-slot antenna geometry. Mesh settings presented on FEM model had 0.004 mm and 2 mm minimum and maximum element size, respectively; the maximum element size was chosen considering the minimum wave length present in the experiment (approximately 2.1 mm for tumor tissue at a frequency of 2.45 GHz); the model had 27 vertex elements, 2412 boundary elements, 12135 elements, and 42756 degrees of freedom solved. Figure 3 shows the mesh for the simulation; it is finer near the slots where the maximum temperature is expected.

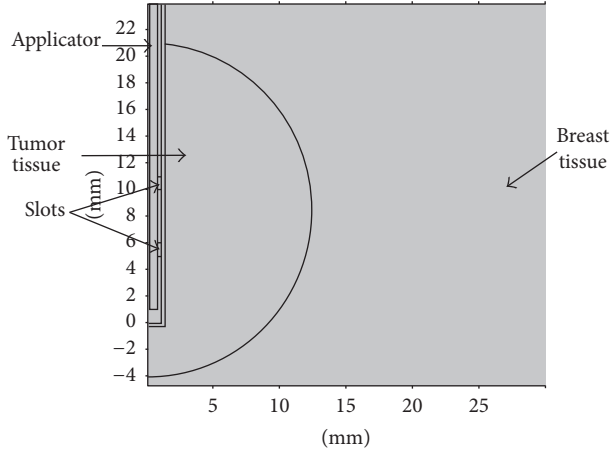


FIGURE 2: Axisymmetric view of the geometry used for the computer model. Tumor was represented as a semicircle surrounded by breast tissue; the slots were positioned inside the tumor. Units are in millimeters.

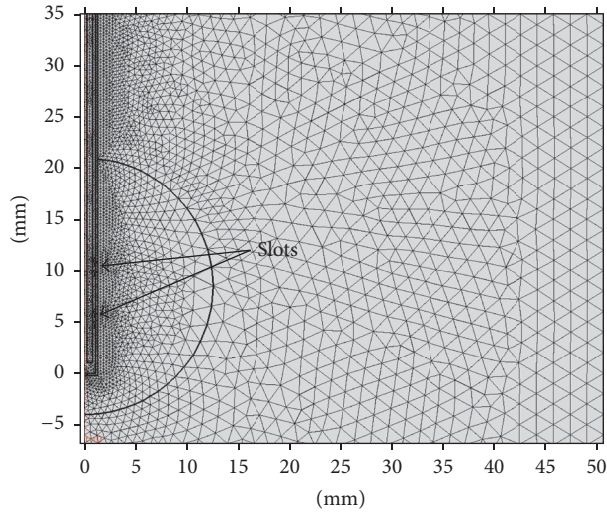


FIGURE 3: Mesh used for computational simulation; the mesh is finer near the slots of the applicator where maximum effect is expected.

Model solution took 25 seconds using 1.18 GB of physical memory and 1.42 GB of virtual memory. 4.0 GHz Intel Core i7 32 GB 1333 MHz DDR4 RAM PC was used to process the model.

For the evaluation of MWA performance, it was important to measure the frequency-dependent reflection coefficient and the specific absorption rate (SAR) pattern in the tissue. A reflection coefficient describes either the amplitude or the intensity of a reflected wave relative to an incident wave. This coefficient can be expressed logarithmically as

$$\Gamma(f) = 10 \times \log_{10} \left(\frac{P_r(f)}{P_{in}} \right) \text{ (dB)}, \quad (2)$$

where P_{in} is the input power and P_r represents the reflected power (both in Watts). SAR represents the amount of average

power deposited per unit mass of tissue ($\text{W} \cdot \text{kg}^{-1}$) at any position; it can be expressed as

$$\text{SAR} = \frac{\sigma}{2\rho} |\vec{E}|^2 \text{ (W} \cdot \text{kg}^{-1}\text{)}, \quad (3)$$

where σ represent tissue conductivity ($\text{S} \cdot \text{m}^{-1}$), ρ is the tissue density ($\text{kg} \cdot \text{m}^{-3}$), and E represents the electric field ($\text{V} \cdot \text{m}^{-1}$). The absorption of microwave energy causes tissue temperature to rise; however, it does not determine the final tissue temperature distribution. Thermal effects should be considered and Pennes bioheat equation can be used for this purpose [20]:

$$\nabla \cdot (-k\nabla T) = \rho_{bl} C_{bl} \omega_{bl} (T_{bl} - T) + Q_{met} + Q_{ext}, \quad (4)$$

where k represents tissue thermal conductivity ($\text{W} \cdot \text{m}^{-1} \cdot \text{K}^{-1}$), ρ_{bl} is the blood density ($\text{kg} \cdot \text{m}^{-3}$), C_{bl} represents the specific heat capacity of the blood ($\text{J} \cdot \text{kg}^{-1} \cdot \text{K}^{-1}$), ω_{bl} is the blood perfusion ($\text{kg} \cdot \text{m}^{-3} \cdot \text{s}^{-1}$), T_{bl} represents blood temperature (K), and T is the final temperature (K). The physical phenomena with the highest repercussion in the equation are microwave heating and tissue heat conduction. The temperature of the blood is approximately the same as body core temperature. Heat radiation (heat conduction) and metabolism heat generation are assumed to be minimal during MWA and are neglected. Also, in *ex vivo* samples $\omega_{bl} = 0$ since there is no perfusion. For Q_{ext} , microwave heating is considered; the microwave generates heat by resistive heating, and the rate of heat is proportional to the square of the applied electric field (E):

$$Q_{ext} = \sigma E^2. \quad (5)$$

For the computational model, an antenna, constructed with a 50Ω semirigid coaxial cable (Model UT-085, Micro-Coax, PA, US) [21], was used. The antenna was encased in a PTFE catheter in order to prevent adhesion of the antenna to desiccated ablated tissue. It was important to add the PTFE catheter to the simulation because, according to [18], it impacts on the SAR distribution and also on the heating pattern.

The conditions used in the simulation are shown in Table 2.

2.4. Model Validation. In order to validate the performance of the simulated applicator, it was built by using a microcoaxial semirigid cable (UT-85) and a SMA connector. Figure 4 shows the diagram for the experimental validation.

2.5. Electromagnetic Radiation System. In order to excite the applicator, a signal generator (Model SML03, Rohde & Schwarz, Munich, Germany) connected to an amplifier (Model I164-BBM3Q6AHM, EMPOWER, NY, US) was used to deliver a 10 W signal for the applicator tests.

2.6. Standing Wave Ratio and Dielectric Properties Measurement. The Standing Wave Ratio (SWR) measurement was performed in two ways: with and without a coupling impedance network. The antenna was immersed in a phantom and was connected to a network analyzer (Model E5071B

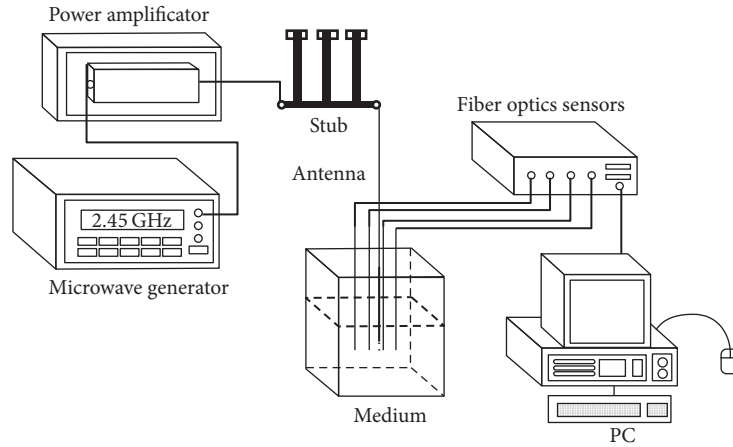


FIGURE 4: Setup for the experimental validation. A 2.45 GHz microwave was generated and amplified to the desired power level; then it was connected to the antenna through a stub. Sensors were used to measure temperature fiber optic.

TABLE 2: Conditions used for simulation of MTA treatment on breast and tumor phantom.

Parameter	Value
Space dimension	Axial symmetry 2D
Heat-transfer module	Time-dependent analysis
RF module	Frequency domain analysis
Boundary RF module	Setting
z axis	Axial symmetry
Port mode	Coaxial
All others	Impedance (Air)
Boundary heat-transfer module	Setting
All exterior	Constant temperature (25°C)
Mesh	Value
Number of vertex elements	27
Number of boundary elements	2412
Number of elements	12135
Breast thermal conductivity	0.42 W/m °K [22]
Breast cancer thermal conductivity	0.50 W/m °K [22]
Blood density	920 Kg/m ³ [22]
Blood heat capacity	3639 J/Kg/°K [23]
Blood perfusion rate	0.0036 s ⁻¹ [23]

ENA, Agilent, CO, USA) to measure the reflection coefficient of the antenna. This equipment was also used to measure the dielectric properties of the breast tissue and the phantoms by the use of the 85071E materials measurement software (Model 5988-9472EN, Agilent, CO, USA) and 85070E dielectric open ended coaxial probe kit (Model 5989-0222EN, Agilent, CO, USA).

The impedance matching network consisted of a stub type tuner (Model 2612C2, Maury Microwave Corporation, CA, USA).

2.7. Phantom Design. A phantom is a mixture of different materials with similar dielectric properties to those of human tissue. The permittivity of tumor tissue is approximately tenfold higher than that of normal tissue [12].

TABLE 3: Dielectric properties of breast and tumor tissue at 2.45 GHz.

Tissue	Conductivity (s/m)	Relative permittivity
Tumor	3.156	59.385
Breast	0.137	5.1467

Previous works were considered in the design and construction of the phantom [12, 24]. Relative permittivity and conductivity are very important properties for the MWA work; therefore, they were measured after the phantom elaboration with the network analyzer. Figure 5 shows these properties as a function of frequency. Table 3 shows the values measured for a 2.45 GHz frequency.

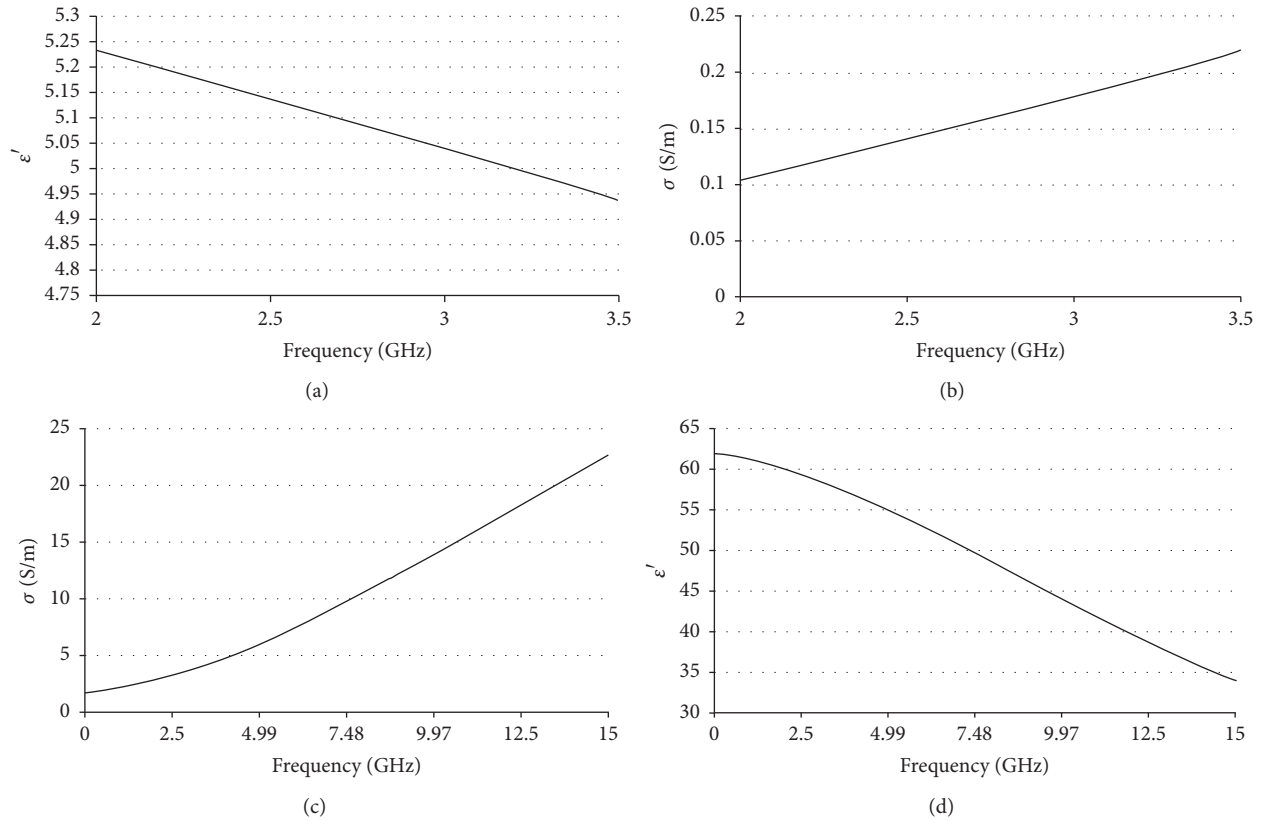


FIGURE 5: Breast relative permittivity (a) and conductivity (b) and tumor relative conductivity (c) and permittivity (d) obtained from [12]. It is important to notice that tumor properties were approximately tenfold higher than those of breast.

For breast phantom elaboration, vegetable oil (150 ml), bidistilled water (50 ml), neutral detergent (30 ml), and agarose (4.5 g) were mixed and heated; breast tumor phantom was composed of bidistilled water (100 ml), ethanol (60 ml), sodium chloride (1 g), and agarose (1.5 g).

As for the geometry used to prepare the phantom, a breast-shaped mold for breast tissue phantom and a sphere of 2.5 cm in diameter for the cancerous tissue phantom were used. The size of the breast mold was the mean value of the measurements of a group of ten volunteer women whose brassiere size was 34B. The sphere geometry was selected because it has axial symmetry, and the sphere size was chosen taking into account a tumor that had gone from T1 to T2, according to TNM Classification of Malignant Tumors [25]. These geometries are shown in Figure 6. Both phantoms are solids; after the elaboration of the tumor phantom the sphere was removed from the mold and then it was inserted in the breast phantom mixture before it solidified.

2.8. Validation Experiment. The applicator was inserted inside the tumor phantom which was surrounded by the breast phantom. An ultrasonic scanner (model ProSound 6, Aloka, Switzerland) was used along the process in order to verify that the position proposed in the computational model was achieved, Figure 7. Once the applicator was positioned, SWR measurements were made. For the validation of the temperature reached, the applicator was inserted into *ex vivo*

swine breast tissue obtained from a local slaughterhouse. In order to place the applicator and temperature sensors, the tissue was half open. Figure 8 shows the setup of this validation experiment.

In order to measure the temperature inside the tissue, three temperature fiber optic sensors (STB Medical probe, Luxtron MAR'05, Lumasense, Santa Clara, CA, USA) were used. The temperature range of the probes was 0 to 120°C, their length was 1 m with a diameter of 0.5 mm, and the response time was 0.25 s. The sensors were non-electromagnetically interfering. They were connected to a thermometer (Model 3300, Luxtron, CA, US), with a resolution of 0.01°C, in order to monitor temperature and to store the data, via a RS-232 cable, in a personal computer. The sensors were placed one in the hottest point according to simulation (1.6 mm, 2.6 mm), one next to the applicator close to the tissue surface (1.32 mm, 100 mm), and the last one at a distance from the applicator equal to the maximum ablation radius (4.2 mm, 3 mm) as shown in Figure 9.

3. Results and Discussion

Successful ablation is considered when total destruction of the tumor is achieved. This destruction depends on the temperature reached on the tumor, which in turn is determined by the energy transfer and coupling between the antenna and the radiated media (phantom or tissue); right

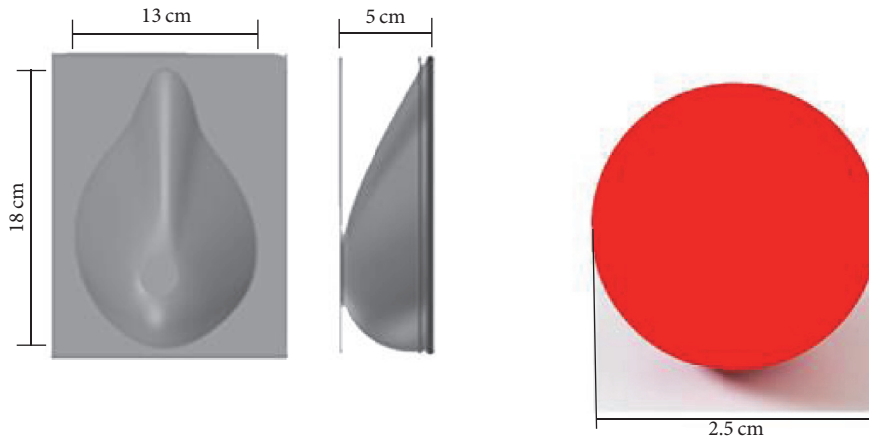


FIGURE 6: Molds used to fabricate breast and tumor phantoms. The size of the breast mold was the mean value of the measurements of ten 34B brassiere size volunteer women. The size for the cancer tissue mold corresponded to a tumor that had gone from T1 to T2.

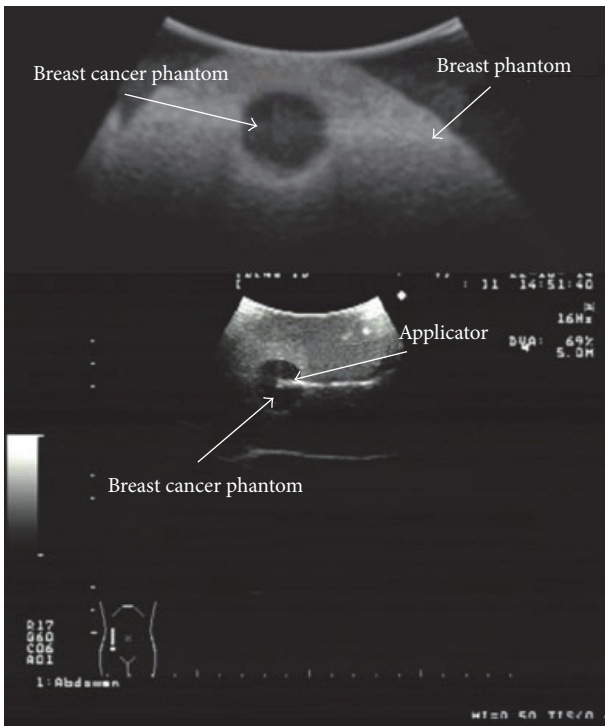


FIGURE 7: Positioning of the applicator. Image obtained through the ultrasonic scanner (model ProSound 6, Aloka, Switzerland). The antenna is shown at the center of breast cancer phantom.

coupling is necessary to prevent backward heating. For these reasons, the most important parameters to consider in the design of the microcoaxial antenna are the maximum temperature reached, the SWR, and the ablation zone. These results are presented below, first for the computer simulation and afterwards for the experimental validation. Finally, a comparison of both is presented.

3.1. Computer Model Results. Figure 10 shows the distribution of the temperature obtained through the computer model

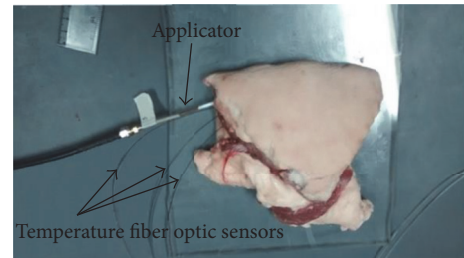


FIGURE 8: Model validation. Applicator and temperature sensors inserted into *ex vivo* swine breast tissue.

when the applicator was inserted into the breast tissue. The maximum temperature reached after 500 seconds (time required for steady state) was 70.6°C for an applied power of 10 W. The maximum radius of the lesion was 4.2 mm (measured from the center of the applicator to the farthest radial point of the 55°C isothermal curve), and the SWR for the frequency of 2.45 GHz was 1.84. Figure 11 shows the temperature distribution in a clinical situation where the applicator was inserted in a spherical tumor of 12.5 mm radius surrounded by breast tissue. The maximum temperature reached for a power of 10 W, after 500 seconds, was 110°C . The maximum radius of injury was 11.2 mm and the SWR for the frequency of 2.45 GHz was 1.87. It is important to note that, with a power of 10 W, the injury was not large enough to cover the entire tumor, but when therapy was performed with a power of 15 W, total tumor ablation was achieved. The maximum temperature reached was 155°C , after 500 seconds, as shown in Figure 12.

3.2. Experimental Validation. For the experimental validation, the temperature measurement was carried out in *ex vivo* swine breast tissue. Additionally, the SWR measurement was performed in a tumor phantom surrounded by a breast phantom; in order to emulate the conditions of the simulation, experiments were performed in triplicate. Figure 13 shows the lesion produced by the applicator inserted *ex vivo* into

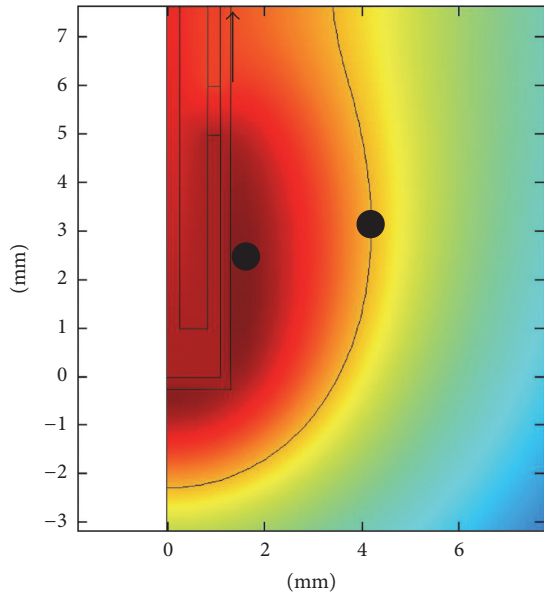


FIGURE 9: Points where temperature sensors were positioned in validation experiment. One in the hottest point, coordinates “1.6 mm, 2.6 mm,” one in the maximum radius of ablation (4.2 mm, 3 mm), and the last one close to tissue surface next to the applicator.

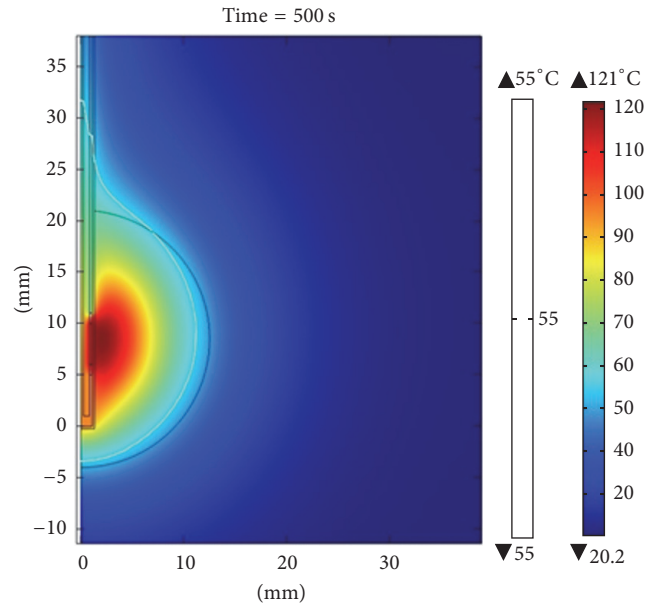


FIGURE 11: Temperature distribution for the simulation when the applicator was inserted in a spherical tumor of 12.5 mm in radius surrounded by breast tissue. The power applied was 10 W; the maximum temperature reached, after 500 seconds, was 110°C.

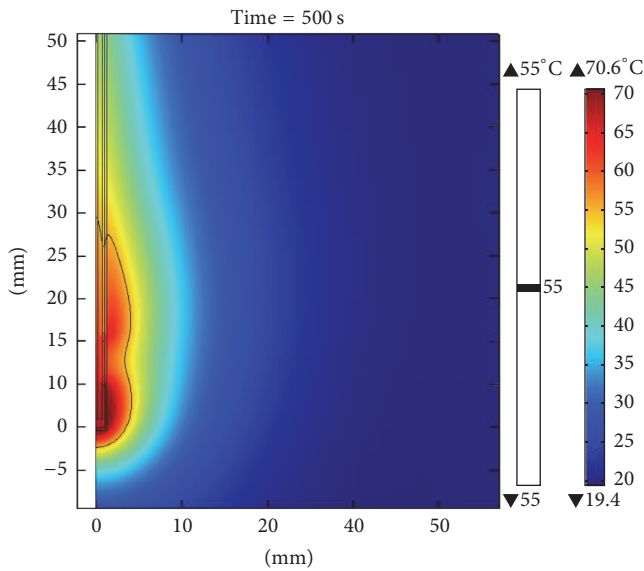


FIGURE 10: Temperature distribution for the simulation when the applicator was inserted in breast tissue. The power applied was 10 W; the maximum temperature reached, after 500 seconds, was 70.6°C.

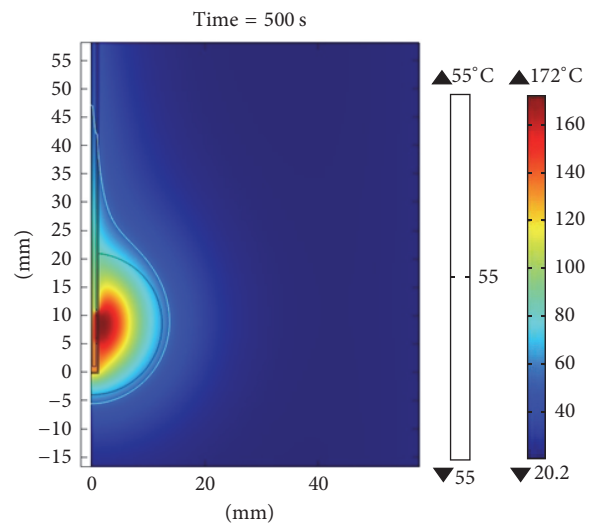


FIGURE 12: Temperature distribution for the simulation when the applicator was inserted in a spherical tumor of 12.5 mm in radius surrounded by breast tissue. The power applied was 15 W; the maximum temperature reached, after 500 seconds, was 155°C.

swine breast tissue. The maximum temperature reached for a power of 10 W was 90°C and the maximum radius of the lesion was 4.3 mm. Moreover, the SWR measured in tumor phantom surrounded by breast phantom for a frequency of 2.45 GHz was 1.04.

3.3. Comparison. As mentioned above, the three most important results were the maximum temperature reached, the

diameter of the lesion, and the SWR. The maximum temperature obtained through simulation with a power level of 10 W and a time of 500 s in healthy breast tissue was 70.6°C, while the maximum temperature reached during the experimental validation in *ex vivo* swine breast tissue was 90°C (Figure 14 shows the temperature rise versus time, both for the simulation and the experimental validation). The maximum radius of the lesion was 4.2 mm and 4.3 mm for simulation and validation experiments, respectively. Finally, the SWR obtained

TABLE 4: Comparison of temperatures (after 500 seconds), SWR, and lesion radius between simulation and experiment.

Medium	Temperature (°C)		SWR		Radius (mm)	
	Simulation	Experiment	Simulation	Experiment	Simulation	Experiment
Breast	70.6	85.43	1.84	—	5	4.1
Breast tumor (10 W)	110	—	1.87	1.04	11.17	—
Breast tumor (15 W)	155	—	1.87	1.04	13.86	—

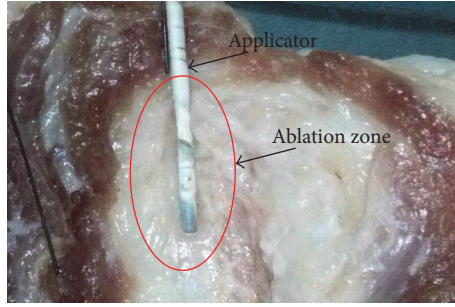


FIGURE 13: Injury produced by the applicator in *ex vivo* swine breast tissue.

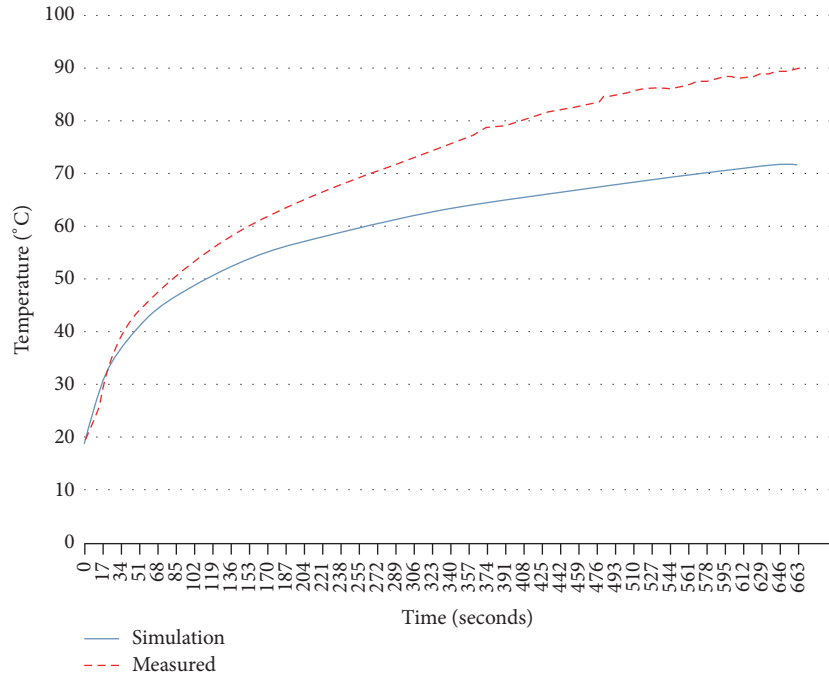


FIGURE 14: Temperature against time for two-slot applicator in *ex vivo* swine breast tissue.

in the simulation of the clinical situation (a tumor of 12.5 mm radius surrounded by breast tissue) for a frequency of 2.45 GHz was 1.87, while the SWR obtained in the experimental validation (sphere tumor phantom of 12.5 mm radius surrounded breast phantom) was 1.04. Figure 15 shows the comparison of the SWR for the frequency band from 2 GHz to 3.5 GHz. A resume of these comparisons is shown in Table 4.

4. Conclusions

Microwave ablation by using double-slot microcoaxial antennas as applicators is a promising technique for cancer

treatment. A feasibility study of the use of this technique for breast cancer treatment was carried out. The results specifically analyzed were temperature, size of lesion, and SWR, of a computational FEM model and physical models (breast phantom and *ex vivo* swine tissue).

The simulations demonstrated the possibility of obtaining ablation temperatures, that is, temperatures higher than 55°C. It was also observed that when the tumor was inside the breast tissue, the heat was focalized inside the tumor and higher temperatures were obtained. This can be explained due to the differences of dielectric properties between tumor and healthy breast tissues, which may be an advantage because

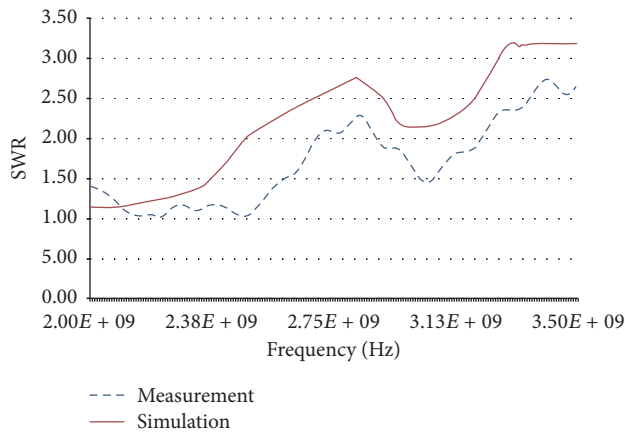


FIGURE 15: Comparison of SWR obtained through simulation (red) and experimental validation (blue).

cancerous tissue can be eliminated without affecting healthy tissue. It is important to mention that, by changing time and power, it was possible to change the size of the lesion caused by ablation; therefore, adjusting these two variables, it would be possible to treat tumors of different sizes.

Concerning the results obtained in physical models, phantom, and swine breast tissue, the possibility of reaching ablation temperatures was confirmed. The temperature obtained was 90°C for swine breast tissue, and the lesion was pear-shaped as in the computational model.

For the SWR, in the physical models a low value, 1.04, was obtained. This value approximated much more to the ideal value, 1.0, than that obtained from the simulation, which was 1.87. This result could be explained on the fact that the dielectric properties of tissue were not as constant and homogenous as they were considered for the simulation. It will also be important to consider that there are variations of dielectric properties from subject to subject, and it will be necessary to include a system to reduce the reflection of the applicator under clinical conditions. For this reason, it would be recommendable to determine the subject's tissue properties in order to run a computational model that determines the best position of the applicator.

However, it is still necessary to validate these results in *ex vivo* breast cancer tissue and *in vivo* laboratory tests before concluding if it is feasible to use this microcoaxial antenna for breast cancer treatment.

Abbreviations

RFA: Radio frequency ablation
 MWA: Microwave ablation
 PTFE: Polytetrafluoroethylene
 FEM: Finite Element Method
 SWR: Standing wave ratio.

Conflicts of Interest

The authors declare that there are no conflicts of interest regarding the publication of this paper.

References

- [1] WHO, GLOBOCAN 2012: Estimated Cancer Incidence, Mortality and Prevalence Worldwide in 2012, <http://www.who.int/cancer/en/>.
- [2] J.-P. Abastado, C. Adams, I. F. Adewole, H. Akaza, N. E. Allen, M. Alsan et al., *World Cancer Report 2014*, International Agency for Research on Cancer, Lyon, France, 2014.
- [3] G. Shafirstein, P. Novák, E. G. Moros et al., "Conductive interstitial thermal therapy device for surgical margin ablation: In vivo verification of a theoretical model," *International Journal of Hyperthermia*, vol. 23, no. 6, pp. 477–492, 2007.
- [4] C. Correa-Gallego, Y. Fong, M. Gonen et al., "A retrospective comparison of microwave Ablation vs. radiofrequency ablation for colorectal cancer hepatic metastases," *Annals of Surgical Oncology*, vol. 21, no. 13, pp. 4278–4283, 2014.
- [5] C. L. Brace, "Radiofrequency and microwave ablation of the liver, lung, kidney, and bone: what are the differences?" *Current Problems in Diagnostic Radiology*, vol. 38, no. 3, pp. 135–143, 2009.
- [6] J. I. Hernández, M. F. J. Cepeda, F. Valdés, and G. D. Guerrero, "Microwave ablation: State-of-the-art review," *OncoTargets and Therapy*, vol. 8, pp. 1627–1632, 2015.
- [7] W. Zhou, X. Zha, X. Liu et al., "US-guided percutaneous microwave coagulation of small breast cancers: A clinical study," *Radiology*, vol. 263, no. 2, pp. 364–373, 2012.
- [8] P. F. Laeseke, F. T. Lee Jr., L. A. Sampson, D. W. van der Weide, and C. L. Brace, "Microwave Ablation versus Radiofrequency Ablation in the Kidney: High-power Triaxial Antennas Create Larger Ablation Zones than Similarly Sized Internally Cooled Electrodes," *Journal of Vascular and Interventional Radiology*, vol. 20, no. 9, pp. 1224–1229, 2009.
- [9] R. C. G. Martin, C. R. Scoggins, and K. M. McMasters, "Safety and efficacy of microwave ablation of hepatic tumors: a prospective review of a 5-year experience," *Annals of Surgical Oncology*, vol. 17, no. 1, pp. 171–178, 2010.
- [10] C. L. Brace, J. L. Hinshaw, P. F. Laeseke, L. A. Sampson, and F. T. Lee Jr., "Pulmonary thermal ablation: Comparison of radiofrequency and microwave devices by using gross pathologic and CT findings in a swine model," *Radiology*, vol. 251, no. 3, pp. 705–711, 2009.
- [11] S. van Esser, M. A. J. Van Den Bosch, P. J. Van Diest, W. T. M. Mali, I. H. M. Borel Rinkes, and R. Van Hillegersberg, "Minimally invasive ablative therapies for invasive breast carcinomas: An overview of current literature," *World Journal of Surgery*, vol. 31, no. 12, pp. 2284–2292, 2007.
- [12] L. Mariya, P. Dijana, M. Leah, B. W. Cynthia, J. L. Mary, H. Josephine et al., "A large-scale study of the ultrawideband microwave dielectric properties of normal, benign and malignant breast tissues obtained from cancer surgeries," *Physics in Medicine and Biology*, vol. 52, p. 6093, 2007.
- [13] J. A. Dickson and S. K. Calderwood, "Temperature range and selective sensitivity of tumors to hyperthermia: a critical review," *Ann N Y Acad Sci*, vol. 335, p. 26, 1980.
- [14] H. I. Vargas, W. C. Dooley, R. A. Gardner et al., "Focused Microwave phased array thermotherapy for ablation of early-stage breast cancer: Results of thermal dose escalation," *Annals of Surgical Oncology*, vol. 11, no. 2, pp. 139–146, 2004.
- [15] C. J. Diederich, "Thermal ablation and high-temperature thermal therapy: overview of technology and clinical implementation," *International Journal of Hyperthermia*, vol. 21, no. 8, pp. 745–753, 2005.

- [16] J. M. Bertram, D. Yang, M. C. Converse, J. G. Webster, and D. M. Mahvi, "A review of coaxial-based interstitial antennas for hepatic microwave ablation," *Critical Reviews in Biomedical Engineering*, vol. 34, no. 3, pp. 187–213, 2006.
- [17] Micro-coax, Ed., *UT-085 datasheet*, Pottstown, Pa, USA.
- [18] J. M. Bertram, D. Yang, M. C. Converse, J. G. Webster, and D. M. Mahvi, "Antenna design for microwave hepatic ablation using an axisymmetric electromagnetic model," *Biomedical Engineering Online*, vol. 5, article no. 15, 2006.
- [19] M. F. J. Cepeda, "Estudio y Desarrollo de Aplicadores Coaxiales Tipo Slot de Ablación por Microondas para el Tratamiento Mínimamente Invasivo del Cáncer de Mama," *Doctor, Bioelectrónica, Centro de Investigación y de Estudios Avanzados del Instituto Politécnico Nacional*, 2011.
- [20] E. H. Wissler, "Pennes' 1948 paper revisited," *Journal of Applied Physiology*, vol. 85, no. 1, pp. 35–41, 1998.
- [21] J. B. P. Micro-coax, Ed., *UT-085 datasheet*, Pottstown, Pa, USA.
- [22] M. Gautherie, "Thermopathology of breast cancer: measurement and analysis of in vivo temperature and blood flow," *Annals of the New York Academy of Sciences*, vol. 335, pp. 383–415, 1980.
- [23] COMSOL, "Electromagnetics Module Model Library," in *COMSOL Multiphysics 3.5*, 2008.
- [24] R. Ortega-Palacios, L. Leija, A. Vera, and M. F. J. Cepeda, "Measurement of breast - Tumor phantom dielectric properties for microwave breast cancer treatment evaluation," in *Proceedings of the 2010 7th International Conference on Electrical Engineering, Computing Science and Automatic Control, CCE 2010*, pp. 216–219, September 2010.
- [25] M. K. Gospodarowicz, J. D. Brierley, and C. Wittekind, *TNM Classification of Malignant Tumours*, Wiley, 2017.